

Entangling the Spatial Properties of Laser Beams

Katherine Ingrid Wagner


A thesis submitted for the degree of
Doctor of Philosophy of
The Australian National University

August, 2010

Declaration

This thesis is an account of research undertaken between February 2007 and August 2010 at The Department of Physics, Faculty of Science, The Australian National University, Canberra, Australia.

The material presented in this thesis was jointly carried out by the Quantum Imaging group at ANU. My contributions to the work were across all components of the experiments - the conception and design, the laboratory work, and the data analysis. The theoretical calculations presented are the result of solitary work.



Katherine I. Wagner

August, 2010

Acknowledgements

There are many people without whom I would not have been able to finish the very rewarding, but also rather difficult process that is a PhD programme. My supervisor Hans Bachor, in particular, I would like to thank for his ability to encourage both the group as a whole and the individuals within the group through the inevitable highs and lows in experiments and enthusiasm. I'd like to extend my thanks to the others who I could go to when I was in need of some help with various physics problems - Ping Koy Lam, Ben Buchler and Charles Harb.

Working with this research group also gave me the opportunity for overseas travel; seeing international perspectives in science and in life¹, was an invaluable experience, for which I am very grateful.

Thanks to the other people, past and present, on the research team who I've been privileged to work with - Vincent Delaubert, Jiri Janousek, Roger Senior, Anaïs Dréau, Jean-François Morizur, and (briefly) Seiji Armstrong.

A big thank you to Ben Buchler and Boris Hage for reading and editing my thesis - it's very much appreciated. Thanks, Rachel (H) for meeting me at Tilley's to do work in the last month or so - this helped my motivation more than you probably realise!

The interesting and friendly group of people that I get to see every day in this department is always a source of enjoyment, and I'm very lucky to have had the company of such a wonderful group of people over the last few years. The lunchtime and beer o'clock conversations are interesting, and sometimes quite... enlightening, to say the least. Thanks to my friends and housemates, some of whom have helped me have fun, some of whom have put up with my messiness, and a few that managed both: Paul, Brigid, Michael, Rachel, Ben, Graham, Stuart, Simon, Emily, Leigh, Esther, Kelsey, Alison, Kev, and Dave. An extra special thank you to Mattias, for always helping me when I need help, and who has the common sense to see that mango plants and kittens deserve more attention than most of humanity.

Last but not least, thanks to my family: Mum, Dad, Mel and Cam, for your love and support.

¹and in skiing

Abstract

The use of non-classical states of light, such as squeezed states, have allowed the exploration of quantum mechanical effects that had previously been the subject of speculation only. One of the more interesting aspects of quantum mechanics is when two objects become linked in a process known as quantum entanglement. This property has been the focus of much research due to the potential applications that are expected to emerge from entangled systems.

This thesis focuses on the various spatial properties of continuous variable entangled systems, and on simplifying entanglement experiments for a given set of resources.

We begin by reviewing the required background quantum optics, and introducing the quantum optics tools that we will be using in the series of experiments.

The rest of the thesis details the experiments performed and the implications of the results that were obtained. Firstly, the spatial entanglement experiment is presented. This experiment involved the observation of Einstein-Podolsky-Rosen entanglement for the position and momentum of two laser beams. The position and momentum observables for laser beams manifest themselves as the displacement and tilt of the beams, and entanglement relies on the used of squeezed TEM_{10} laser modes, mixed with a TEM_{00} reference mode. The result of the EPR measure for the system was found to be 0.62 ± 0.03 .

The next section deals with a multimode entanglement experiment, where two spatial modes are entangled in a single beam of light. The experiment offers several simplifications upon more standard entanglement layouts, including the use of a single quadrant detector for the measurements, and a single squeezer that was used to produce two independent squeezed spatial modes. The observed Inseparability of the system was found to be 0.79 ± 0.02 .

Lastly, the effect of asymmetries in entangled systems was investigated. The possibility of changing the beamsplitter ratio in biased entanglement experiments in order to improve the measurements made was shown to be a useful approach in some circumstances. An experiment was performed, and showed that by changing the beamsplitter ratio, the value from the EPR criterion can be optimised, and in some cases can show entanglement when it would otherwise not be possible.

Contents

Declaration	iii
1 Introduction	1
2 Theoretical Quantum Optics and Optics Tools	5
2.1 Introduction	5
2.2 Quantum Uncertainty	5
2.3 Operators and Quadratures	6
2.4 Linearised Operators	7
2.5 Beamsplitters	8
2.6 Detection	9
2.6.1 Simple detection	10
2.6.2 Balanced homodyne detection	10
2.7 States of light	12
2.7.1 Vacuum state	12
2.7.2 Number state	13
2.7.3 Coherent state	14
2.7.4 Squeezed state	14
2.8 Spatial modes	15
2.8.1 Origins	15
2.8.2 Gouy phase shift	16
2.9 Optical cavities	17
2.9.1 Cavity Locking	22
2.9.2 Mode Cleaners	27
2.9.3 Mode Transfer and Combination	28
3 Squeezing and Entanglement	31
3.1 Introduction	31
3.2 Nonlinearities	31
3.3 Optical Parametric Amplification	32

3.3.1	OPA Cavity Equations	33
3.3.2	Nonlinear crystals	35
3.3.3	Loss on a Squeezed Beam	36
3.4	EPR and Inseparability	37
3.4.1	Inseparability criterion	45
3.4.2	EPR entanglement	47
4	Spatial Entanglement	53
4.1	Introduction	53
4.2	Displacement and tilt of a beam	53
4.2.1	Classical displacement and tilt of a beam	53
4.2.2	Heisenberg limit	55
4.3	Squeezing in higher order spatial modes	57
4.3.1	OPA layout	57
4.3.2	Ideal pump mode shape	59
4.3.3	Squeezing for different pump powers	59
4.4	Experimental setup	61
4.4.1	The laser	61
4.4.2	Optical Parametric Amplifiers	63
4.4.3	Mode combination	65
4.4.4	Locking Scheme	68
4.4.5	Measurement method	72
4.5	Experimental results	73
4.6	Conclusion	78
5	Multimode Entanglement	81
5.1	Introduction	81
5.2	Producing the squeezed beam	82
5.3	Simultaneous mode detection	84
5.3.1	Quadrant Detector	84
5.3.2	Digital data acquisition	86
5.3.3	Simultaneous squeezing measurements	89
5.4	Entangling the two modes	90
5.4.1	Cylindrical lenses	91

5.5	Spatial modes	94
5.6	Future work	96
5.7	Conclusion	97
6	Asymmetric entanglement	99
6.1	Direction of inference	99
6.2	Biased entanglement	104
6.2.1	Beamsplitter Ratio	105
6.2.2	Experimental Details	110
6.3	Conclusion	113
7	Conclusion	115
A	Entanglement equations	119
B	Biased entanglement theory	123
	Bibliography	125

List of Figures

2.1	Mixing beams on a beamsplitter	9
2.2	Different detector setups	10
2.3	Ball-on-stick diagrams for different states of light	13
2.4	Hermite Gauss modes	16
2.5	A cavity showing the different cavity parameters	18
2.6	Effect of a cavity transmission on beam variance	19
2.7	Cavity output power depends on cavity finesse	21
2.8	Different spatial mode resonances in a cavity	22
2.9	Pound-Drever-Hall locking	24
2.10	Amplitude and frequency modulations	25
2.11	The phase and power for a beam that is reflected from a cavity.	26
2.12	A mode cleaning cavity	28
2.13	A flip mode plate	29
2.14	Overlap between spatial modes	30
3.1	A generic OPA cavity	34
3.2	Loss on a squeezed beam	37
3.3	A standard entanglement setup	38
3.4	Different modes of light	39
3.5	Quantum noise is uncorrelated	41
3.6	Correlations between entangled beams	42
3.7	Correlation ellipses and standard deviation measurements	43
3.8	Correlation ellipses for changing local oscillator phase	44
3.9	Inseparability	48
3.10	EPR entanglement	49
3.11	Second EPR value - $\epsilon_{y x}$	50
3.12	Effect of loss on entanglement	51
3.13	EPR can be measured with 3dB of squeezing	52

4.1	Displacement and tilt of a beam	54
4.2	OPA configurations	58
4.3	Effect of OPA output coupler value	61
4.4	Spatial entanglement schematic	62
4.5	OPA design used	63
4.6	Measured TEM_{00} squeezing and antisqueezing	64
4.7	Measured TEM_{10} squeezing and antisqueezing	65
4.8	Effect of pump power on TEM_{10} squeezing and antisqueezing	66
4.9	Spatial mode combination	67
4.10	Dither locking	69
4.11	Homodyne detector signals used in experiment	72
4.12	Results for amplitude quadrature	74
4.13	Amplitude quadrature conditional variance	75
4.14	Results for phase quadrature	75
4.15	Phase quadrature conditional variance	76
4.16	Spatial entanglement results	76
4.17	Two values obtained for EPR entanglement	78
5.1	Schematic for experiment to produce squeezed TEM_{01} and TEM_{01} modes from a single OPA.	83
5.2	Results for squeezing in TEM_{01} and TEM_{01} modes from the single OPA.	84
5.3	Principle of split detection technique.	85
5.4	Methods of data collection	87
5.5	Correlation ellipse	88
5.6	Simultaneous detection of the squeezed TEM_{01} and TEM_{10} modes.	89
5.7	The intensity and phase response for the transmission of the OPA cavity	90
5.8	Multimode entanglement experiment setup.	91
5.9	Squeezing results for TEM_{10} and TEM_{01} modes with a $\pi/2$ phase shift.	92
5.10	Results of variances of entangled modes	92
5.11	Example of inseparability measurement.	93
5.12	Inseparability results for multimode entanglement experiment.	94
6.1	Standard entanglement setup	100

6.2	Correlation ellipses for a symmetric system, and for a system with a loss on one entangled arm	101
6.3	Effect of beamsplitter transmission on EPR entanglement	102
6.4	Asymmetric results were seen in the spatial entanglement experiment . . .	103
6.5	Correlation ellipses for a biased entanglement experiment	107
6.6	Effect of beamsplitter ratio on correlation ellipses	108
6.7	EPR measurement with changing loss	108
6.8	EPR value for biased entanglement, when the OPA transmission and the beamsplitter ratio are varied	109
6.9	Simplified asymmetric entanglement experimental setup	110
6.10	Asymmetric entanglement experimental setup	111
6.11	Data taken during experiment	112
6.12	Conditional variance found from data	113
6.13	Results for biased entanglement experiment	114
A.1	Mixing beams and the effect on the amplitude quadrature	120
B.1	Results for the Inseparability in a biased entanglement experiment.	124

Introduction

The concept of entanglement was originally conceived by Einstein, Podolsky, and Rosen, as a thought experiment to show the apparent contradictory nature of quantum mechanics. This thought (*Gedanken*) experiment was published in the 1935 paper “Can quantum-mechanical description of physical reality be considered complete?” [1], and has since been termed EPR entanglement after the three authors. The criticism of quantum mechanics is twofold in the paper - in one case, entanglement would imply non-locality of quantum mechanics - in dramatic contrast to all the established physics at the time. If this were not true, the authors wrote, then quantum mechanics could not be complete without some extra unknown variables causing the system to act in the way it does. These criticisms represent what are today considered to be the most interesting features of quantum mechanics, with the most promising potential applications.

For some applications the noise characteristics inherent in quantum systems represent a fundamental limitation on measurements, but it is these same characteristics that allow some of the most interesting possibilities of modern physics. Potential applications have been suggested that range from quantum cryptography and (more distantly) quantum computers, to quantum teleportation. Thus entanglement is considered important from both the perspective of fundamental physics with the implication of non-locality, and as a potential tool in future quantum devices.

For some years after its proposal, the existence or otherwise of entanglement was seen as a fairly academic distinction, since at that stage there were no measures that could be made that gave any insight into the problem. So it remained until 1964, when Bell published his famous inequalities, elevating entanglement from a philosophical novelty to a measurable effect. Violations of Bell’s inequalities were measured by Clauser [2] and Aspect et. al. [3], showing that some of the predictions of quantum physics were indeed true. The ability to measure EPR entanglement was extended into the continuous variable regime in 1989 by Reid [4], using conditional variances to verify the entanglement

of the beams. There is now a vast array of literature detailing entanglement experiments that have been conducted with single mode continuous (cw) beams, with demonstrations of strong entanglement between the amplitude and phase quadratures of pairs of beams [5, 6, 7] or the polarisation of the beams [8, 9, 10].

This thesis extends upon this series of experiments in the continuous variable regime with an experiment in spatial entanglement, a multimode entanglement experiment, and an experiment on asymmetric entanglement.

These three experiments each considers at least one of two central themes. These are:

- the extension of cw quantum entanglement experiments to higher order spatial modes, and
- the simplification or optimisation of entanglement experiments in order to deal with limited and imperfect resources.

These themes are practical rather than fundamental in nature; while they don't result in applications directly, they are important building blocks for the future uses on continuous variable quantum optics and entanglement.

Squeezed higher order spatial modes are used extensively in the experiments in this thesis, and both the efficient creation of these states and the subsequent entanglement of them have significance in wider research areas.

Squeezed higher order spatial modes are applicable to metrology when precision measurement of a transverse distance or displacement is required. Classical higher order spatial modes have long been used for the manipulation of micro-particles - a technique that is of interest for bio-sensing applications. The implementation of squeezed higher order mode light in such a system is currently being investigated by quantum optics groups in Australia.

Aside from the efficient creation of squeezed higher order spatial modes, this thesis also deals with the entanglement of these modes. The main motivation for using squeezed higher order spatial modes in entanglement experiments is the potential application of this type of entanglement to the emerging field of quantum communication.

In many experiments on the development of quantum communication tools, there has been a tendency towards the expansion of entangled systems to include extra channels [11, 12], resulting in multipartite entanglement. The reason for this expansion is the large payoff that accompanies the extra complexity - with more channels, the potential applications

of the entangled system increase greatly, with an improvement in the information capacity of the beams.

The tendency in continuous beam quantum optics has been to extend the entanglement to spatially separated channels, each in the fundamental spatial mode. The quantum resources required for such a setup increase dramatically as the number of channels increases, with extra squeezers, detectors, and mixing devices. Here an alternative is presented where the higher order spatial modes are instead used as the extra channels, with an in principle experiment entangling two spatial modes, with an accompanying decrease in the required resources. The argument in favour of simplifying quantum resources for communication purposes only becomes more compelling when one considers the broader research environment, which includes active areas such as optical memories with retrieval on demand [13] and systems for imposing delays on EPR entangled beams [14].

The asymmetric entanglement experiment, also, requires only one squeezer to operate, reducing the resources required. The operation of a biased entanglement system traditionally has a higher requirement on the squeezer - it must not have a loss greater than 33% in order for EPR entanglement to be achieved, whereas in a two-squeezer setup a loss of up to 50% can be tolerated. This limitation was explored, and by optimising the system for the level of loss present, it was found that EPR entanglement could in fact be measured for higher losses. This experiment again improves the ability to create entangled systems using limited resources.

The layout of the rest of this thesis is as follows.

Chapter 2 introduces the existence of quantum uncertainty, and the use of linearised quadrature operators for measuring the uncertainty for light fields. Basic tools that are needed for many quantum optics experiments are introduced, such as beamsplitters, optical cavities, and light detection techniques.

Chapter 3 discusses the use of nonlinearities in materials to induce squeezing as a method for manipulating the noise of a light field. Quantum entanglement is then introduced, with a description of different criteria of continuous variable entanglement.

Chapter 4 moves on to the experimental section of the thesis. It details the spatial entanglement experiment, where the position and momentum of laser beams are entangled. In the spirit of the original *Gedanken* experiment, the witness used for this experiment is EPR entanglement.

Chapter 5 moves on to the multimode entanglement experiment. This experiment

sees entanglement produced and measured within a single laser beam, using two different spatial modes of the beam.

Chapter 6 contains the asymmetric entanglement experiment, which explores the optimisation of biased entanglement for losses that occur in different parts of the entanglement system. Theoretical predictions are made for the ideal beamsplitter ratio that is required to compensate for the losses in the entanglement system, in some cases allowing the measurement of EPR entanglement when it otherwise wouldn't be measurable. The experimental results are also compared to the theoretical predictions. The method of optimisation can also be applied to conventional (non-biased) entanglement systems.

Chapter 7 contains the concluding comments for entanglement, and the future possible extension of the ideas discussed within this thesis.

Theoretical Quantum Optics and Optics Tools

2.1 Introduction

Here we introduce the basic background for general quantum optics experiments, with both experimental and theoretical sections. The existence of quantum noise and various quantum states of light are introduced. The linearised model is used to describe the behaviour of experimental components that are based on beamsplitters, such as homodyne detection setups. Optical cavities and the locking of these cavities is also discussed.

2.2 Quantum Uncertainty

The Heisenberg Uncertainty Principle [15] is one of the fundamental underlying concepts of quantum mechanics. Many quantum optics experiments operate in the manipulation of this limit, to investigate the boundaries of what can be detected.

For a pair of Hermitian operators with the commutation relation:

$$[A, B] = C \tag{2.1}$$

then if A and B correspond to observable quantities, the corresponding uncertainty relation is given by:

$$\Delta^2 A \Delta^2 B \geq \left(\frac{1}{2i} \langle C \rangle \right)^2 \tag{2.2}$$

where $\Delta^2 X$ refers to the variance of the measurement X . The variance is defined as:

$$V = \Delta^2 X = \langle \langle X^2 \rangle - \langle X \rangle^2 \rangle. \tag{2.3}$$

The noise can also be given in terms of the standard deviation, σ , which is the square root of the variance.

In order to explore the quantum limits of measurements, we must first have a set of variables for which the uncertainty principle applies; that is, we need a pair of operators that don't commute. The most common examples used for the inherent uncertainty in physical systems are the position and momentum operators, which have the uncertainty relation:

$$\Delta^2 x \Delta^2 p \geq \left(\frac{\hbar}{2}\right)^2. \quad (2.4)$$

Another useful pair of operators more relevant to optics are the creation and annihilation operators of the electromagnetic field, a^\dagger and a , which have the commutation relation $[a, a^\dagger] = 1$. Note that since the creation and annihilation operators are not Hermitian, the Heisenberg Uncertainty Principle does not apply in this case.

2.3 Operators and Quadratures

For optical systems, states of light can be understood and expressed using the photon creation and annihilation operators, \hat{a}^\dagger and \hat{a} . These are ladder operators for a harmonic oscillator, so starting with any quantum state of light, and in particular the ground state $|0\rangle$, we can arrive at all higher number states by the successive application of the creation operator.

The Hamiltonian, and thus the energy, of a single mode optical field in a linear medium is identical to that of the harmonic oscillator, and is given by [16]:

$$\hat{H} = \hbar\omega(\hat{a}^\dagger\hat{a} + \frac{1}{2}). \quad (2.5)$$

A single mode field, with annihilation and creation operators \hat{a} and \hat{a}^\dagger , can also be described in terms of a quadrature operator:

$$\hat{X}^\theta = \hat{a}e^{-i\theta} + \hat{a}^\dagger e^{i\theta}. \quad (2.6)$$

If we look at the operator obtained when $\theta = 0$, we arrive at what we define to be the amplitude quadrature:

$$\hat{X}^+ = \hat{a} + \hat{a}^\dagger \quad (2.7)$$

and when $\theta = \pi/2$ we obtain the phase quadrature:

$$\hat{X}^- = -i(\hat{a} - \hat{a}^\dagger). \quad (2.8)$$

The advantage of the quadrature operators over the ladder operators (\hat{a} and \hat{a}^\dagger) is that they are Hermitian, and thus have real eigenvalues, leading to theoretical results that are measurable in experiments.

The commutation relations for these operators are given by:

$$\begin{aligned} [\hat{a}, \hat{a}^\dagger] &= 1 \\ [\hat{X}^+, \hat{X}^-] &= 2i. \end{aligned} \quad (2.9)$$

There are many states of light that can be described, ranging from tools that are solely for conceptual purposes to working mathematical descriptions of laser beams. These states will be discussed later, but for the moment we will stay with a general field with annihilation and creation operators \hat{a} and \hat{a}^\dagger , which for simplicity will from here on be written without the hats that indicate they are operators.

The field is subject to uncertainty relations, so will always have some noise present in the system, and it is this noise on the field that we wish to be able to observe here. In order to understand physical processes, the existence of an analytic solution to a problem is a great advantage, and can give a useful insight into the system. When using the boson creation and annihilation operators, analytic results can be obtained for complicated systems by using suitable approximations on the operators.

2.4 Linearised Operators

For most experimental applications, the analytic results obtained from the linearised model [17] can be used. Here we break up the annihilation operator a , and the creation operator a^\dagger , into the expectation value for the operator, α , and a fluctuation term, δa .

$$\begin{aligned} a(t) &= \alpha + \delta a \\ a^\dagger(t) &= \alpha^* + \delta a^\dagger. \end{aligned} \quad (2.10)$$

where we have the expectation values for the two operators, $\alpha = \langle a \rangle$ and $\alpha^* = \langle a^\dagger \rangle$, and δa and δa^\dagger are the quantum fluctuations, so $\langle \delta a \rangle = \langle \delta a^\dagger \rangle = 0$. In quantum optics, it is the

fluctuations on the different states that are of particular interest, so it is these fluctuations that we must measure. Unless otherwise specified, the operator is a function of time for the rest of this thesis.

The power of the field is proportional to the number operator $n = a^\dagger a$. The number operator gives the total number of photons in the field, which is proportional to the power that can be measured using a normal photodetector.

$$\begin{aligned} a^\dagger a &= (\alpha^* + \delta a^\dagger)(\alpha + \delta a) \\ &= \alpha^* \alpha + \alpha^* \delta a + \alpha \delta a^\dagger + \delta a^\dagger \delta a. \end{aligned} \quad (2.11)$$

If we take α as real and assume $\langle \delta a^2 \rangle \ll \alpha$, then we can eliminate the negligible term that corresponds to the product of two small fluctuations, and we arrive at:

$$a^\dagger a \approx \alpha^2 + \alpha(\delta a + \delta a^\dagger) = \alpha^2 + \alpha(\delta X^+). \quad (2.12)$$

The quantum noise of the amplitude quadrature can then be seen via the power fluctuations that occur on a photodetector, with a variance

$$\begin{aligned} V_n &\approx \langle (\alpha^2 + \alpha \delta X^+)^2 \rangle - \langle \alpha^2 + \alpha \delta X^+ \rangle^2 \\ &= \alpha^2 V^+ \end{aligned} \quad (2.13)$$

where V^+ is the variance of the amplitude quadrature of the beam.

The variance of the phase quadrature (V^-) is not accessible by simply measuring the field directly with a photodetector. In order to perform many quantum optics experiments, we need to be able to measure both of the non-commuting operator pairs, and to be able to mix different fields together. Both of these tasks can be performed using the process of interference.

2.5 Beamsplitters

A standard beamsplitter consists of a thin layer of dielectric film or metal supported by a piece of glass, with the metal deposited to a thickness at which it reflects half of the incident photons and transmits the other half.

Figure 2.1 shows two input beams, a and b , interfering on a beamsplitter of power transmission t , and forming two outputs c and d . The beams are interfered with a relative

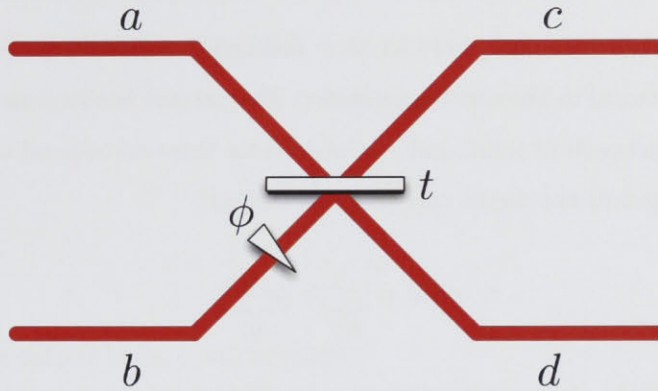


Figure 2.1: A beamsplitter with two inputs a and b mixed with a phase difference ϕ to produce two outputs c and d .

phase difference of ϕ . The outputs can then be described as:

$$\begin{aligned} c &= e^{i\theta_c}(\sqrt{1-t}a + e^{i\phi}\sqrt{t}b) \\ d &= e^{i\theta_d}(\sqrt{t}a - e^{i\phi}\sqrt{1-t}b) \end{aligned} \quad (2.14)$$

where θ_c and θ_d are the rotations required to make the expectation values $\langle c \rangle$ and $\langle d \rangle$ real for the two resulting beams; that is, we are setting the amplitude quadrature to correspond to the intensity of the field. Note that this is not strictly necessary, and we can also arbitrarily set θ_c and θ_d to zero, and the best approach often depends on the experiment being described.

Models of beamsplitters are useful for several reasons. Firstly, beamsplitters are used extensively in our experiments, both as a central component of the experiment, and in the detection systems. In addition to this, the equations that are used to describe the behaviour of light at a beamsplitter are also useful for describing other experimental devices used for mixing modes together, and for describing losses that are encountered by the field.

2.6 Detection

Here we are interested in detecting both quadratures of a beam of light. The basic tool for this is the photodetector, but the details of how it is used can vary.

2.6.1 Simple detection

Simple detection has just one photodetector measuring a beam's power. The current induced is proportional to the number operator. The current has two components: a fluctuating term and a constant term, and on the detector these correspond to the alternating current (AC) output or the direct current (DC) output.

$$n = a^\dagger a = \underbrace{\alpha^2}_{DC} + \underbrace{\alpha \delta X^+}_{AC} \quad (2.15)$$

While easy to perform, such a measurement is insufficient for many quantum optics experiments since it is limited to measuring just one quadrature. It is also difficult to normalise the measurements taken if different noise levels for different beams are to be compared.

2.6.2 Balanced homodyne detection

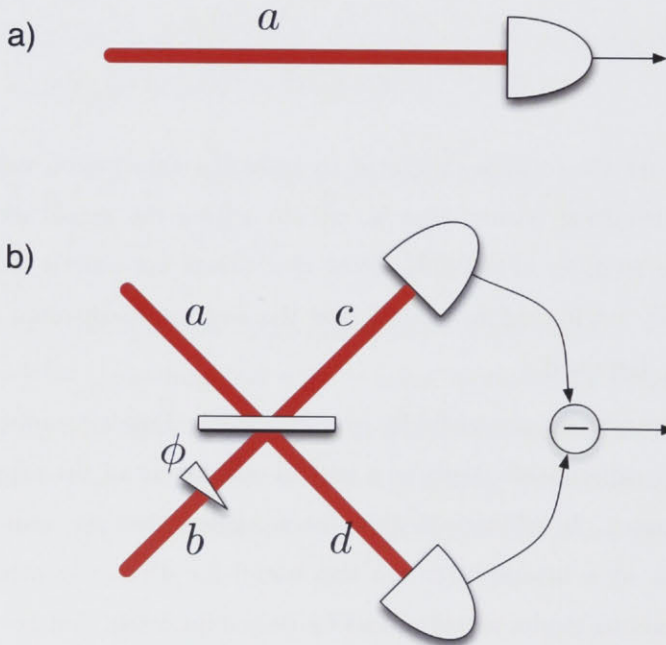


Figure 2.2: Common detector setups: **a)** simple detection, and **b)** balanced homodyne detection.

We have already looked at beamsplitters and simple photodetectors. One very useful scheme for achieving measurements on any quadrature combines these two tools, and is known as balanced homodyne detection. With this method, the beam of interest is mixed

with another beam on a beamsplitter, and each of the two outputs are measured with a photodetector. This is shown in Figure 2.2.

For a 50:50 beamsplitter, the outputs can be described as:

$$\begin{aligned} c &= \frac{1}{\sqrt{2}} e^{i\theta_c} (a + be^{i\phi}) \\ d &= \frac{1}{\sqrt{2}} e^{i\theta_d} (a - be^{i\phi}). \end{aligned} \quad (2.16)$$

A detector on the output beam c will measure:

$$c^\dagger c = \frac{1}{2} (a + be^{i\phi})^\dagger (a + be^{i\phi}). \quad (2.17)$$

If we apply the linearisation technique, and eliminate the negligible terms, this becomes:

$$\begin{aligned} c^\dagger c &= \frac{1}{2} [\alpha^2 + \beta^2 + 2\alpha\beta \cos \phi + \beta (\delta b + \delta b^\dagger) + \alpha (\delta a + \delta a^\dagger) + \alpha (\delta b e^{i\phi} + \delta b^\dagger e^{-i\phi}) \\ &\quad + \beta (\delta a e^{-i\phi} + \delta a^\dagger e^{i\phi})]. \end{aligned} \quad (2.18)$$

Normally, we make one beam (here b) much brighter than the beam that we actually want to observe. This bright beam is then called the local oscillator. The approximation $\beta \gg \alpha$ means that we can omit the terms that are not at least of order one in β , simplifying the expression somewhat.

$$\begin{aligned} c^\dagger c &\approx \frac{1}{2} \left[\beta^2 + 2\alpha\beta \cos \phi + \beta (\delta b + \delta b^\dagger) + \beta (\delta a e^{-i\phi} + \delta a^\dagger e^{i\phi}) \right] \\ &= \underbrace{\frac{1}{2} \beta^2 + \alpha\beta \cos \phi}_{DC} + \underbrace{\frac{1}{2} \beta \delta X_b^+ + \frac{1}{2} \beta \delta X_a^\phi}_{AC}. \end{aligned} \quad (2.19)$$

A similar expression can be found for the second output beam:

$$d^\dagger d \approx \frac{1}{2} \beta^2 - \alpha\beta \cos \phi + \frac{1}{2} \beta \delta X_b^+ - \frac{1}{2} \beta \delta X_a^\phi. \quad (2.20)$$

If we then look at the difference of these two currents:

$$c^\dagger c - d^\dagger d \approx \underbrace{2\alpha\beta \cos \phi}_{DC} + \underbrace{\beta \delta X_a^\phi}_{AC}. \quad (2.21)$$

The AC term then can measure the noise on any quadrature component of the field,

and which quadrature is measured depends on the relative phase difference ϕ between the two beams incident on the beamsplitter. In the meantime, if the field of interest has some small amplitude α , then this will result in a slight modulation of the DC component of the photodetector's response as the phase difference changes, so that there is verification of which quadrature is being measured.

2.7 States of light

Now that we have looked at how noise on beams of light can be measured, we will take a brief look at different states of light.

2.7.1 Vacuum state

A vacuum state describes a mode that contains no photons, yet still contains fluctuations, as expected with quantum mechanics. It is usually written as $|0\rangle$, and is a symmetric minimum uncertainty state, so that:

$$\Delta^2 X^+ = \Delta^2 X^- = 1. \quad (2.22)$$

Since this state contains no photons, applying the number operator gives $a^\dagger a|0\rangle = 0$, and the energy of the system, as found by the Hamiltonian in Equation 2.5, is non-zero, and given by $\frac{\hbar\omega}{2}$.

A knowledge of the vacuum state allows us, through the creation operator, to describe many other states of light useful in quantum optics. It also provides a method for describing the way light interacts with one of the fundamental optics tools, the beamsplitter. A ball-on-stick diagram of a vacuum state is shown in Figure 2.3a. Ball-on-stick diagrams have the amplitude and phase quadratures for the axes, and show the coherent amplitude with the length of the 'stick' and the amount of noise is represented with the 'ball'. The width of the ball for any given axis projection is related to the standard deviation for the state.

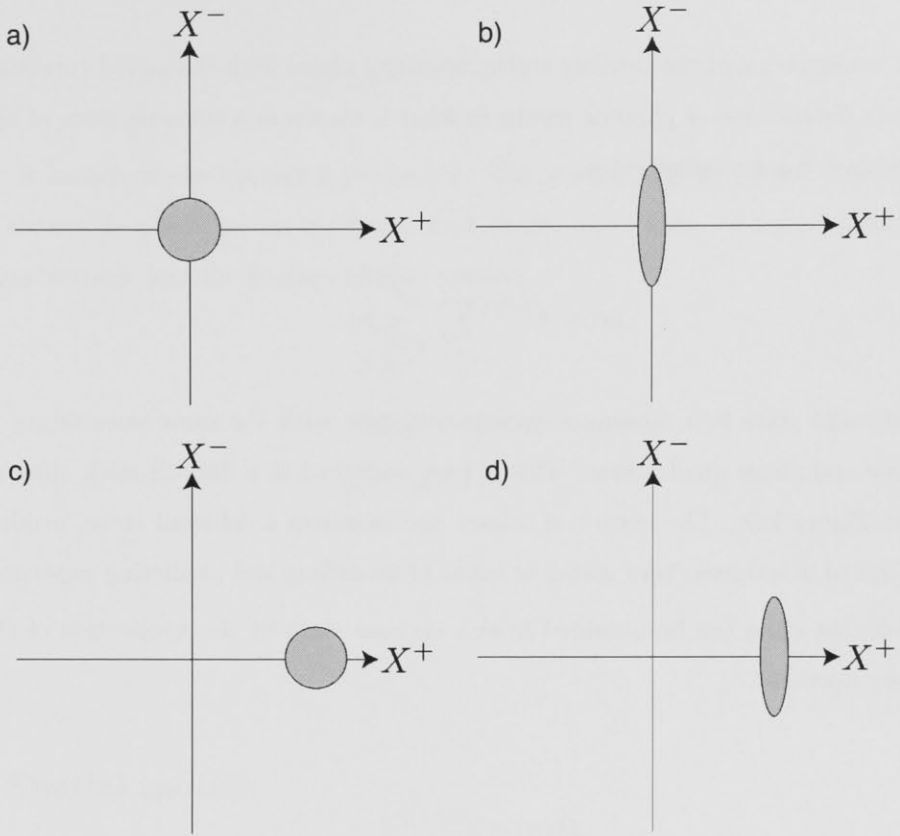


Figure 2.3: Ball-on-stick representations of various quantum states of light. The grey area represents the uncertainty distribution for the different states. **a)** the vacuum state, **b)** vacuum squeezing, **c)** a coherent state, and **d)** amplitude squeezing.

2.7.2 Number state

Given some state of light with a certain number of photons, $|n\rangle$, the state with one more photon can be found by the application of the creation operator, as follows.

$$a^\dagger|n\rangle = \sqrt{n+1}|n+1\rangle. \quad (2.23)$$

Successive application of this operator then allows any *number state* (also termed Fock state) to be described in terms of some state with a lower number of photons. Since we already have the vacuum state $|0\rangle$, we can then describe any number state using:

$$|n\rangle = \frac{(a^\dagger)^n}{\sqrt{n!}}|0\rangle. \quad (2.24)$$

2.7.3 Coherent state

A linear combination of the number states described above with the added condition of a Poissonian distribution of photons results in what is known as a coherent state of light. A coherent state can be described as:

$$|\alpha\rangle = e^{|\alpha|^2/2} \sum_n \frac{\alpha^n}{\sqrt{n!}} |n\rangle. \quad (2.25)$$

A coherent state is a minimum uncertainty state with the same uncertainty in the amplitude and phase quadratures. This is best described in a ‘ball-on-stick’ diagram, as shown in Figure 2.3c. The output of a laser approximates a coherent state, making this mathematical description very useful in terms of modelling and predicting experiments.

A coherent state can be obtained from a vacuum state by the application of the displacement operator.

$$D(\alpha) = e^{\alpha a^\dagger - \alpha^* a} \quad (2.26)$$

Applying this to the the vacuum state then gives us:

$$D(\alpha) |0\rangle = |\alpha\rangle. \quad (2.27)$$

2.7.4 Squeezed state

The coherent state has amplitude and phase quadrature uncertainties given by $\Delta X^+ = \Delta X^- = 1$. This level of noise is a fundamental limit on laser beams and is known as the Quantum Noise Limit, or QNL. If certain quantum processes act upon this coherent state, the uncertainty in one quadrature can be decreased below this limit. This decrease in uncertainty on one quadrature comes at the expense of the other quadrature, as required by the Heisenberg Uncertainty Principle. A state with uncertainty lower than the quantum limit in one quadrature is known as squeezed light, due to the new shape that replaces the circle in the Figure 2.3.

The squeezed state can be obtained by applying the squeezing operator to a vacuum or coherent state.

$$S = e^{\frac{1}{2}(r^* a^2 - r a^{\dagger 2})} \quad (2.28)$$

where r is known as the squeezing parameter. The squeezing parameter r is related to several observable quantities on the beam, such as the uncertainty on the amplitude and phase quadratures, and the average photon number:

$$\begin{aligned} \Delta X^+ &= e^{-r} \\ \Delta X^- &= e^r \\ \langle n \rangle &= \sinh^2 r. \end{aligned} \quad (2.29)$$

2.8 Spatial modes

2.8.1 Origins

In general, quantum optics experiments operate using the fundamental Gaussian spatial transverse mode for spherical resonators, TEM_{00} . Though it can introduce extra complications, there is no reason why the experiments cannot take advantage of the different spatial modes that can be produced. Higher order spatial modes provide extra degrees of freedom for information to be transmitted, as well as providing access to extra information about the fundamental mode.

Any general image can be described in terms of a combination of a complete set of modes, such as the Hermite-Gauss modes.

The Hermite Gauss modes can be described as:

$$TEM_{nm}(x, y, z) = \frac{C_{nm}}{w(z)} H_n \left(\frac{\sqrt{2}x}{w(z)} \right) H_m \left(\frac{\sqrt{2}y}{w(z)} \right) e^{-\frac{(x^2+y^2)}{w(z)^2}} e^{ik\frac{(x^2+y^2)}{2R(z)}} e^{i\phi_G(z)} \quad (2.30)$$

where we have introduced

$$C_{nm} = \frac{1}{\sqrt{\pi 2^{n+m+1} n! m!}} \quad (2.31)$$

$$z_R = \frac{\pi w_0^2}{\lambda} \quad (2.32)$$

$$R(z) = z + \frac{z^2}{z_R} \quad (2.33)$$

$$w(z) = w_0 \sqrt{1 + \left(\frac{z}{z_R}\right)^2} \quad (2.34)$$

$$\phi_G(z) = -(n + m + 1) \tan^{-1} \left(\frac{z}{z_R} \right) \quad (2.35)$$

where λ is the wavelength, w_0 is the beam waist, w is the beam width, z_R is the Rayleigh range for the beam, $R(z)$ is the radius of curvature, and $\phi_G(z)$ is the Gouy phase shift. A few examples of spatial modes can be seen in Figure 2.4.

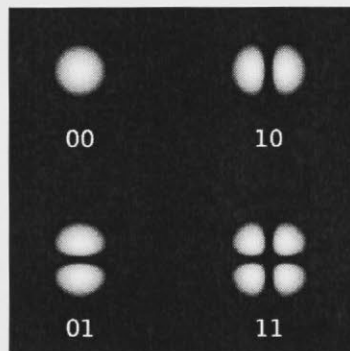


Figure 2.4: The intensity distribution for several of the lower order TEM modes.

It is possible to create a beam that contains squeezed light in several spatial modes by either creating the different squeezed modes and then combining them, or by using a squeezer that is able to operate at several modes at the same time. The operation of a squeezer that transmits several modes simultaneously can be technically very challenging, depending on the method of squeezing being used.

2.8.2 Gouy phase shift

A collimated TEM_{00} mode travels a slightly different path length to a TEM_{00} mode that travels through a focus, and this results in a relative phase shift between the focussed and collimated cases. A higher order spatial mode propagating through the same system as

the focussed TEM₀₀ mode will again travel a slightly different path length to the focussed TEM₀₀ mode, since the average mode size is slightly larger, resulting in an additional phase shift. This is known as the Gouy phase shift [18], as shown in Equation 2.30, and can be applied to a general Gaussian mode TEM_{*mn*}, as described by:

$$\phi_G(m, n, z) = -(m + n + 1) \tan^{-1} \left(\frac{z}{z_R} \right) \quad (2.36)$$

where z is the position of interest, relative to the beam waist, and z_R is the Rayleigh range for the beam.

2.9 Optical cavities

An optical cavity, in its simplest form, consists of two partially reflecting mirrors, or beamsplitters, positioned in such a way that light can build up in between the two mirrors. When there is constructive interference within the cavity, it is on resonance, and there is a maximum in the transmission of the cavity. If the cavity is not on resonance, most of the light will be reflected by the first mirror. Adding an extra mirror forms a ring cavity, shown in Figure 2.5, allowing the various input and output fields to be visualised more easily.

Here the field inside the cavity is labeled a , and the main input and output fields are A_{in} and A_{out} . There is some coupling rate between the interior and exterior fields at each of the beamsplitters, and here κ_{in} is the coupling rate through the input mirror, κ_l is the coupling rate for the loss inside the cavity, and κ_{out} is the coupling rate for the output mirror. The vacuum fields are prefaced with a δ , as seen with the vacuum field coupled in at the output coupler δA_ν , or the vacuum field coupled in by intra-cavity losses δA_l . The field reflected from the cavity, A_{ref} , can be either a vacuum output or a coherent field, depending on the transmission of the cavity mirrors. A calculation of $\langle a^\dagger a \rangle$ gives the number of photons contained in the cavity, whereas a calculation of $\langle A^\dagger A \rangle$, since it is a travelling wave, gives the number of photons per second. κ , the coupling rate, has units s^{-1} .

The equation of motion for an empty cavity is given by:

$$\dot{a} = -\kappa a + \sqrt{2\kappa_{in}} A_{in} + \sqrt{2\kappa_l} \delta A_l + \sqrt{2\kappa_{out}} \delta A_\nu \quad (2.37)$$

where κ is the sum of all three coupling rates. This equation is valid for a non-detuned

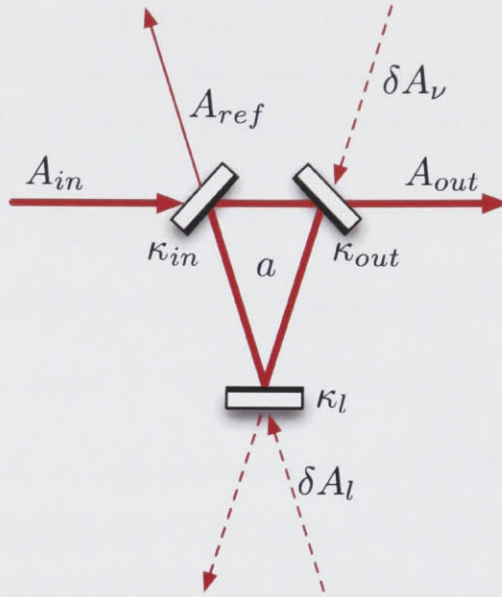


Figure 2.5: A ring cavity with interior field a , with various modes coupling in and out of the cavity. The loss of the cavity is modelled by the lower mirror with coupling rate κ_l .

cavity, that is, a cavity where the frequency of the input field is equal to the cavity frequency. If the Fourier transform of this is taken to move us into the frequency domain, the boundary conditions for the input and output fields are given by [19]:

$$\begin{aligned}\tilde{A}_{ref} &= \sqrt{2\kappa_{in}}a - \tilde{A}_{in} \\ \tilde{A}_{out} &= \sqrt{2\kappa_{out}}a - \delta\tilde{A}_\nu\end{aligned}\quad (2.38)$$

and the transmitted field of the cavity can then be calculated to be:

$$\tilde{A}_{out} = \frac{2\sqrt{\kappa_{out}\kappa_{in}}\tilde{A}_{in} + (2\kappa_{out} - \kappa - i\omega)\delta\tilde{A}_\nu + 2\sqrt{\kappa_{out}\kappa_l}\delta\tilde{A}_l}{i\omega + \kappa}\quad (2.39)$$

where ω is the frequency shift from the optical carrier, and \tilde{O} indicates that we are referring to a function of frequency $\tilde{O}(\omega)$ rather than a function of time $O(t)$. Similarly, the reflected field can be found to be:

$$\tilde{A}_{ref} = \frac{(2\kappa_{in} - \kappa - i\omega)\tilde{A}_{in} + \sqrt{\kappa_{in}\kappa_{out}}\delta\tilde{A}_\nu + 2\sqrt{\kappa_{in}\kappa_l}\delta\tilde{A}_l}{i\omega + \kappa}.\quad (2.40)$$

Given that we normally measure the quadrature fluctuations, it is convenient to write

the output in terms of these operators.

$$\tilde{X}_{out}^{\pm} = \frac{2\sqrt{\kappa_{out}\kappa_{in}}\tilde{X}_{in}^{\pm} + (2\kappa_{out} - \kappa - i\omega)\delta\tilde{X}_{\nu}^{\pm} + 2\sqrt{\kappa_{out}\kappa_l}\delta\tilde{X}_l^{\pm}}{i\omega + \kappa} \quad (2.41)$$

From this equation we can then obtain the variance of the field at different sideband frequencies, allowing us to see the noise properties so central to quantum optics experiments.

$$\tilde{V}_{out}^{\pm} = 1 + \frac{4\kappa_{out}\kappa_{in}(\tilde{V}_{in}^{\pm} - 1)}{\omega^2 + \kappa^2}. \quad (2.42)$$

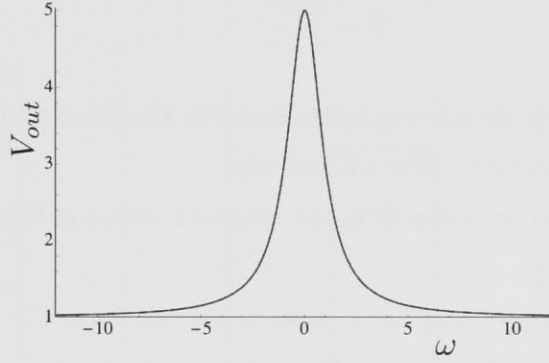


Figure 2.6: The output variance for a frequency ω of a cavity for a laser beam that originally has a variance of 5. The coupling parameters used are $\kappa_{out} = 0.5$, $\kappa_{in} = 0.5$ and $\kappa_l = 0$. The variance drops to QNL for high frequencies.

The output variance is plotted for different sideband frequencies in Figure 2.6. The variance is initially 5, but after transmission through the cavity the variance decreases as ω moves away from zero. In this case, the initial variance of 5 occurs for both quadratures, and the output variance is the identical for both quadratures. This filtering effect is characteristic of optical cavities and is a very useful effect, since our experiments usually aim to measure the amount of noise in the system, and excess classical noise can obscure the effects being investigated. For more details on cavities and their effects on beams of light, see [20].

If we look at the intensity of the reflected field shown in Equation 2.40 and ignore the noise terms by finding $\tilde{A}_{ref}^\dagger \tilde{A}_{ref}$ and disregarding the δ terms, we get the classical reflected power.

$$\tilde{P}_{ref} = \frac{(2\kappa_{in} - \kappa)^2 + \omega^2}{\kappa^2 + \omega^2} \tilde{P}_{in} \quad (2.43)$$

Often the cavity is required to transmit as much of the light as possible in order to be used in other parts of the experiment. When the reflected intensity is minimised, then more of the intensity is travelling through the cavity, as is required. If we look at the carrier frequency, this occurs when $\kappa_{in} = \kappa_{out} + \kappa_l$, a condition that results in an impedance matched cavity.

There are various parameters for resonators that are very useful experimentally for the design and operation of a cavity. The finesse is a parameter that gives a comparison of the energy density within the cavity to the energy density without the cavity. It can be found to be [21]:

$$\mathcal{F} = \frac{\pi r^{1/2}}{1 - r} \quad (2.44)$$

where r is the round trip attenuation factor, given by the fraction of the amplitude of a wave that remains in the cavity after a round trip.

The output power for two different finesse cavities is shown in Figure 2.7 as the cavity length is changed.

The free spectral range (ν_{FSR}) of a cavity is the inverse of the round trip time for that cavity. For a cavity with round trip length L and refractive index n , the free spectral range is then given by:

$$\nu_{FSR} = \frac{c}{nL}. \quad (2.45)$$

In Figure 2.7b, the cavity length, and hence the cavity frequency, was changed while the laser frequency was kept constant. Similarly, if the cavity length is kept constant and the laser frequency is changed, there will be resonance peaks, with periods of very low transmission in between. The parameter used to quantify the frequencies over which the cavity will transmit is the cavity linewidth, which can be found to be:

$$\frac{\nu_{FSR}}{\mathcal{F}}. \quad (2.46)$$

In order to have a stable, high finesse cavity there is usually some focussing of the field inside the cavity. While cavities are usually operated using a TEM₀₀ field, they can instead be set to transmit a higher order spatial mode. If we consider two different spatial modes travelling through a cavity, it is clear that the higher order mode will undergo a relative

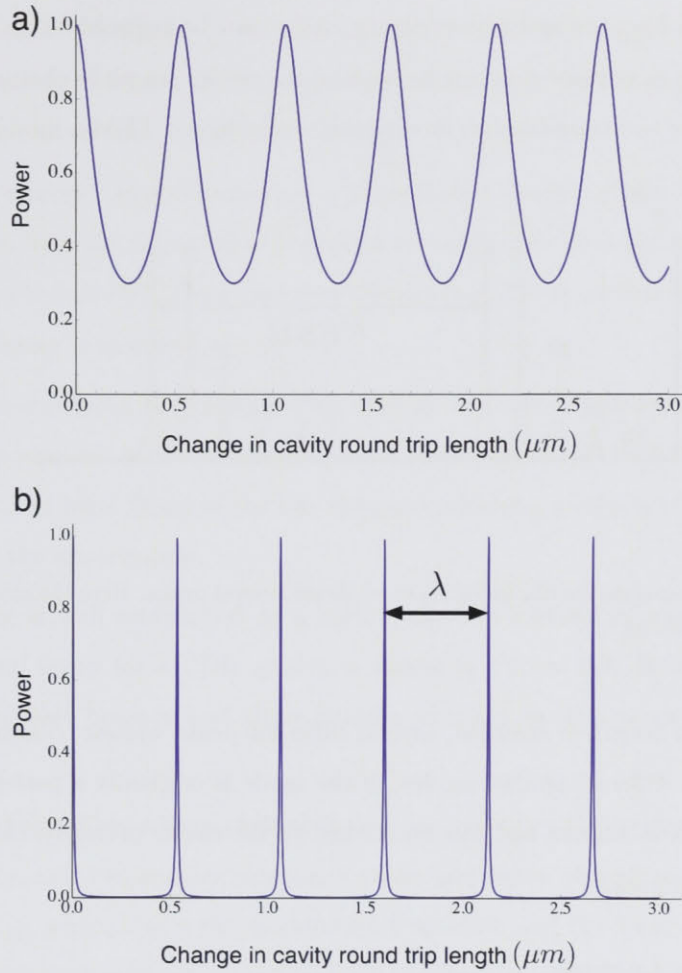


Figure 2.7: The output power of the cavity as the length is scanned for different finesse. **a)** $\rho = 0.1$, giving a finesse of 2.4, and **b)** $\rho = 0.95$, giving a finesse of 59.6.

phase shift as it is focused and defocused, as seen in the expression for the Gouy phase shift in Equation 2.36. In order to achieve resonance, the extra phase shift imparted onto the higher order mode must be compensated for, and this is done by slightly adjusting the length of the cavity. For this reason, a cavity will generally not be resonant for different spatial modes at the same time¹.

If a beam containing several spatial modes is aligned into the cavity, the cavity's length can be set to transmit one of these modes. A single spatial mode beam that is slightly

¹There are exceptions to this, such as the transmission of both TEM_{nm} and TEM_{mn} for a cavity that is rotationally symmetric about the beam axis. Another exception is the confocal cavity design, which is able to transmit several spatial modes.

tilted from its ideal alignment into the cavity is identical to having several spatial modes in a well-aligned beam, since any arbitrary shape can be reduced to its Hermite-Gauss components. These components can be seen as the cavity length is changed, as shown in Figure 2.8, where the transmission intensity of a misaligned TEM_{00} mode is used.

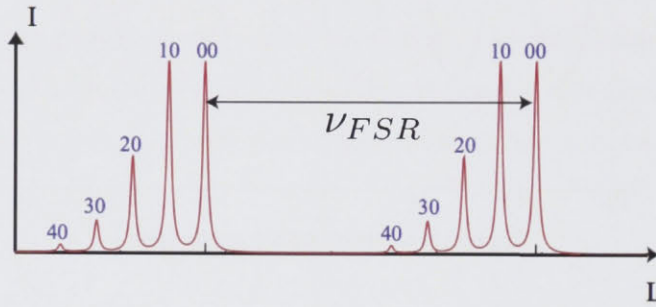


Figure 2.8: A misaligned cavity being scanned shows several peaks. Here the mode corresponding to each peak is labeled.

As the cavity length is scanned, several different peaks appear, corresponding to the resonance of the different spatial modes. If the mode is originally a perfect eigenmode of the cavity, and it is aligned and mode-matched to the cavity precisely, then there is only one transmission peak.

2.9.1 Cavity Locking

In order to have an operating optical cavity, there must be constructive interference for the field inside the cavity. Constructive interference occurs when the optical path length of the cavity is $n\lambda$, or an integer number of wavelengths. The length of the cavity must then be controlled to ensure that constructive interference is maintained, allowing constant transmission of the light through the cavity. For cavities with highly reflective mirrors, and therefore a high finesse, any small deviation from one of the cavity resonance peaks will result in no transmission, as seen in Figure 2.7. For this reason, cavity locking systems are in place in many optics experiments. The locking system makes some measurement on the system, and produces a feedback signal based on this measurement. The feedback signal then goes to an actuator that is built in to the cavity² that then modulates the cavity length as required.

²The feedback can also control an actuator inside the laser, to adjust the laser frequency to match the cavity frequency.

Since the degree of control required is typically of the order of nanometres, slight disturbances such as vibrations or even air currents can affect the path length and stop the cavity operating. Cavities are thus made as mechanically stable as possible - with a heavy base and covered with a protective casing.

The actuator most commonly used is a piezoelectric device, where the shape of the material changes with the voltage that is applied across it. The piezoelectric material used for the actuators here is PZT (lead zirconate titanate), and it is on this material that one of the cavity mirrors is mounted.

There are several types of locking system used in this thesis. One method that is used in all of the experiments in this thesis is termed Pound-Drever-Hall (PDH) locking, and this will be outlined here. Some of the less ubiquitous locking methods will be introduced as they arise in the experiments.

PDH locking is well established as a highly effective method of cavity stabilisation [22]. The general setup for a PDH system is shown in Figure 2.9. Before the cavity is encountered, the laser beam is first phase modulated using an electro-optic modulator, or EOM.

A modulated signal has a large peak at the carrier frequency Ω , which in this case is the optical frequency, and two smaller sidebands above and below this. The higher sideband occurs at $\Omega + \Omega_M$, where Ω_M is the modulation frequency, and the lower sideband occurs at $\Omega - \Omega_M$. These sidebands rotate in time with the frequency of the applied modulation, changing from being real (aligning with the carrier) to being imaginary, to being negative with respect to the carrier. When the sideband at $\Omega + \Omega_M$ aligns with the carrier signal, the angle of the corresponding lower sideband indicates the form of modulation present. If the second sideband is also positive, then the beam is amplitude modulated at Ω_M , as shown in Figure 2.10a. If the second sideband is negative, then the beam is phase modulated at Ω_M , as seen in Figure 2.10b. For a signal where the second sideband is partly imaginary, there is a combination of amplitude and phase modulation, shown in Figure 2.10c. The value of the parameter θ shown indicates the amount of phase and amplitude modulation.

For PDH locking, we first want a phase modulated beam, and the signal must be detected on either the transmitted or the reflected beam - typically the reflected beam since this will not be used for other parts of the experiment. The modulation frequency can be either inside or outside the cavity linewidth with the same end result. The measurement

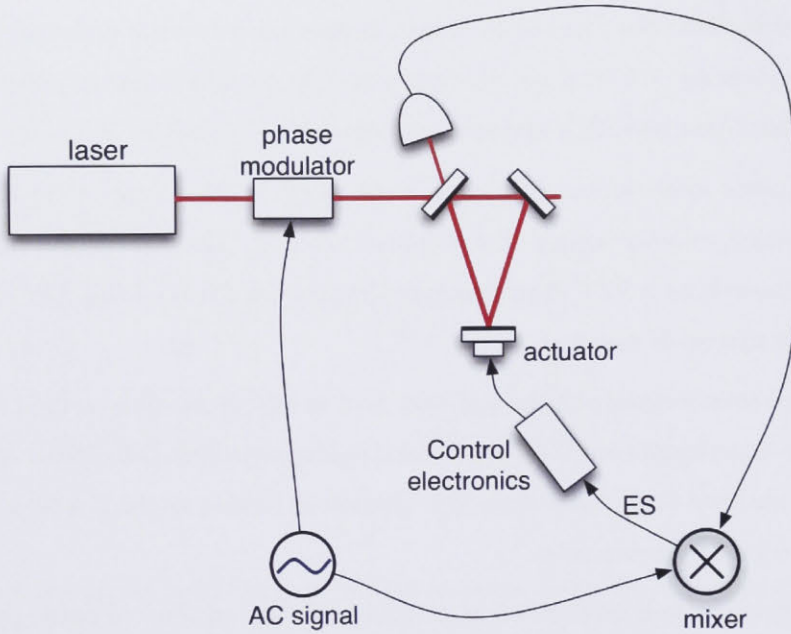


Figure 2.9: A locking system for keeping a triangular cavity on resonance. The beam is phase modulated before being sent into a cavity. The reflected beam is detected and mixed with the signal used for the phase modulation, producing an error signal (ES), that then changes the length of the cavity.

from the reflected beam is then mixed with the same modulation that is fed into the EOM, and the resultant signal is then the feedback, or error signal.

For a high finesse cavity that is on resonance, the carrier beam will largely be transmitted through the cavity, and the sidebands and some portion of the carrier will be reflected. If the cavity starts to move off resonance, the reflected component of the carrier field will undergo a relative phase shift θ , as shown in Figure 2.11, and what was before perfect phase modulation will be mixed with amplitude modulation. The sign of the phase shift depends on the direction of the drift off resonance for the cavity.

The reflected light then contains information about how far from resonance the cavity is, and in whether the cavity needs to be made longer or shorter.

The AC component of the reflection is given by:

$$AM \approx \sin \Omega_M t \sin \theta. \quad (2.47)$$

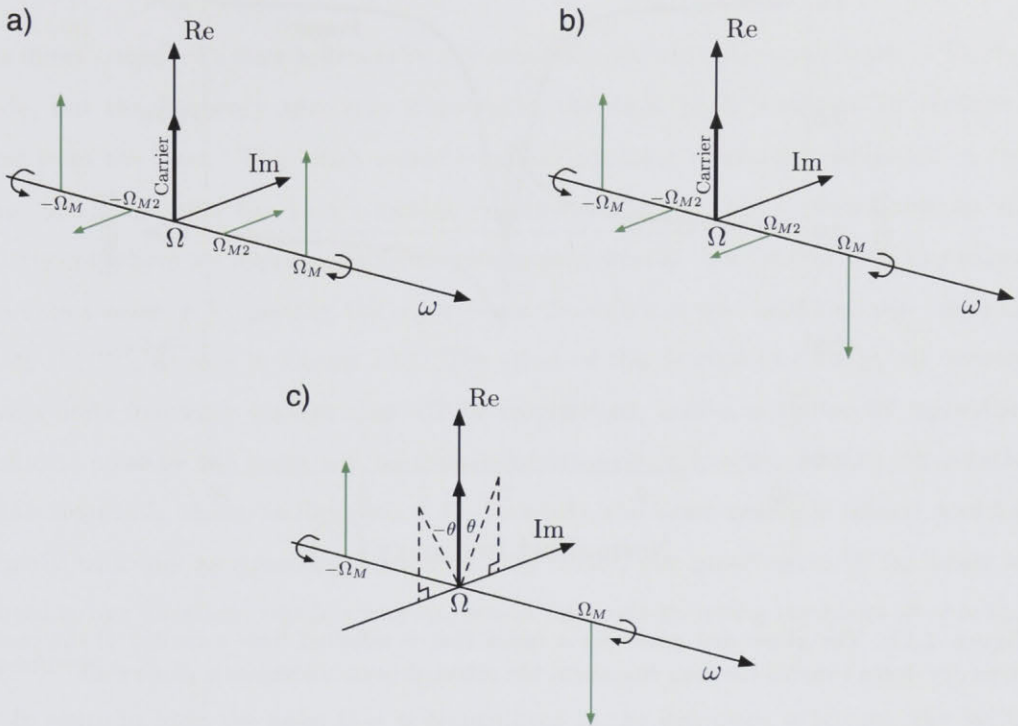


Figure 2.10: The sideband picture can be used to describe **a)** amplitude modulation, **b)** frequency modulation, and **c)** a combination of both amplitude and frequency modulation. Ω_M and Ω_{M2} are modulation frequencies that are used.

This is then mixed with the original modulating signal, creating an error signal:

$$ES \approx \sin^2 \Omega_M t \sin \theta = \frac{1}{2} \sin \theta (1 - \cos 2\Omega_M t). \quad (2.48)$$

The signal can then be altered using some electronics - if we include a low-pass filter, the error signal no longer has the $\cos 2\Omega_M t$ component. Looking only at small deviations from the resonance - small values of θ - we have an error signal that is directly proportional to the correction that is required to the cavity length.

The actuator then moves in the direction that brings θ to zero, eliminating the amplitude modulation and moving the cavity back to a resonance position. For larger values of θ , the linear relationship no longer holds. This reflects the limitation of correction possible for the locking system - if the length of the cavity changes too far from its ideal position, the error signal is no longer able to correct the path length. This highlights the importance of mechanical stability, to minimise the deviations that occur.

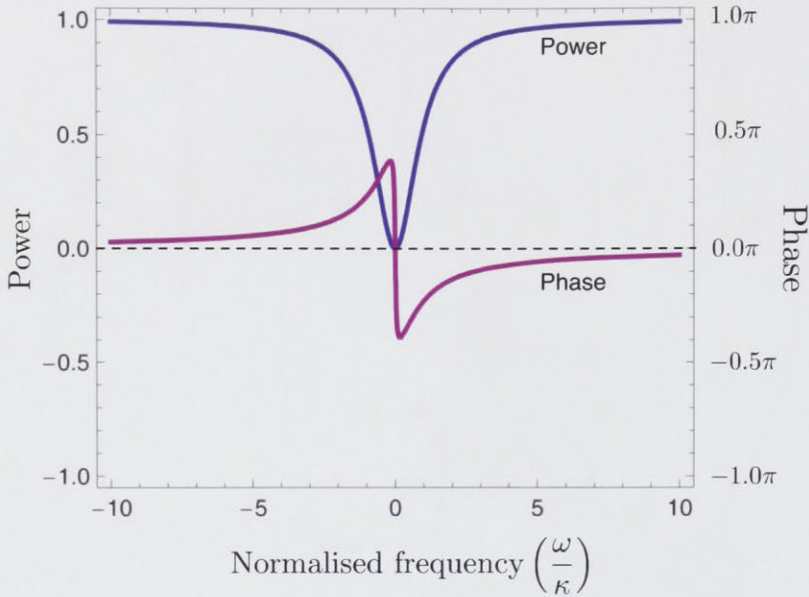


Figure 2.11: The phase and power for a beam that is reflected from a cavity. If the cavity frequency doesn't match the laser frequency, the reflected beam undergoes a phase shift.

Control electronics

The main device used in these experiments for the electronic control of the locking systems is a PID controller. The PID or proportional-integral-derivative controller is an important tool for noise suppression in the locking loop, and allows for locking systems of high stability to be achieved.

The PID controller consists of three stages:

- The *proportional* stage multiplies the error signal by a fixed function, to optimise the correction for fast changes in the cavity length;
- The *integral* stage integrates the error signal over some time window, allowing the cavity control system to compensate for slow drifts that occur in the system; and
- The *derivative* state returns a value based on the derivative of the error signal. This can allow for the system to predict near-future movements, and compensate for these as they occur.

The use of a PID controller can improve the stability of some locking systems to a point where they can remain locked for many hours.

2.9.2 Mode Cleaners

The direct output of a laser is generally a reasonable approximation to a Gaussian TEM₀₀ mode, but the frequency spectrum surrounding the main peak is marred by technical noise from the laser. This noise comes from the resonant relaxation oscillation of the laser, and noise from the laser's locking processes. Clearly, this is undesirable for an experiment where we require quantum noise limited beams. The easiest way to remove this excess noise, is by passing the noisy beam through a cavity, called a *mode cleaning cavity* (MCC), as seen in Figure 2.12. The effect of this is twofold - firstly, all cavities have a finite frequency window that will be transmitted, known as the cavity linewidth. Technical noise on the beam will be attenuated strongly at frequencies that fall outside of this linewidth, shown in Equation 2.46. Secondly, the beam profile is refined, and for a cavity with any astigmatism (such as a ring cavity) the polarization of the beam is limited to one direction, which is very important for mode-matching the beam later in the experiment.

In order to limit the noise that is transmitted in the frequency spectrum, the MCC should have a low cavity linewidth. Since the cavity linewidth is given by ν_{FSR}/\mathcal{F} , this can be achieved by lowering the free spectral range (achieved by increasing the length of the cavity), or increasing the finesse of the cavity by increasing the reflectivity of the input and output mirrors in the cavity.

In reality, adjusting these parameters will at some stage introduce a penalty to the MCC's operation. Increasing the length eventually makes the cavity less stable, and also makes alignment of the cavity more difficult. Increasing the reflectivity of the mirrors makes any losses within the cavity more significant, as seen by increasing the κ_{in} and κ_{out} in the cavity equations earlier, and limits the overall transmission of the cavity. Increasing the finesse also means that the energy density on each of the mirrors is higher, which means high quality, clean mirrors are needed to avoid burning the surface.

The MCCs used in this experiment have three mirrors - two flat mirrors, and one curved mirror. In order to achieve the best possible transmission through a cavity, the mode that is incident on the first cavity mirror must match the eigenmode of the cavity. The mode shape of the transmitted beam is also determined by this cavity eigenmode. For this reason, it is preferable for the cavity to not impart any astigmatism onto the transmitted beam. While a curved mirror in a ring cavity will always impart some astigmatism onto the beam, the curved mirror is placed such that the light strikes it with a small angle of

incidence to minimise the astigmatism, as seen in Figure 2.12. The reflectivity of the two top mirrors depends on the polarisation of light being used. The reflectivity is higher for s-polarised light - that is, light with a polarisation perpendicular to the plane of incidence, leading to a higher finesse cavity in this case.



Figure 2.12: The triangular mode cleaning cavity used in this experiment.

2.9.3 Mode Transfer and Combination

Using several modes into an experiment requires new methods in the manipulation of the beams. Firstly, there is the creation of higher modes from the TEM_{00} mode we originally obtain from the laser. For the Hermite-Gauss basis, where circular symmetry is not required, we can tilt the input to the MCC in order to excite a higher order mode of the cavity. The cavity can then be set in length to the mode that is required - different spatial modes encounter different Gouy phase shifts inside the cavity, and so require slightly different cavity lengths. The efficiency of such a mode conversion is limited to the overlap of the original beam used and the beam being produced, so a direct conversion results in a substantial loss of laser power. In order to minimize this loss, phase plates can be used before the MCC to produce an input mode that more closely approximates the required mode. A phase plate is a device that imparts a spatially dependent phase shift on the beam. For the conversion of TEM_{00} to TEM_{10} , which is performed in experiments in this thesis, this is done with a ‘flip-mode plate’ [23], shown in Figure 2.13, placed in front

of the MCC. This plate gives an extra π phase shift to one side of the TEM_{00} beam,

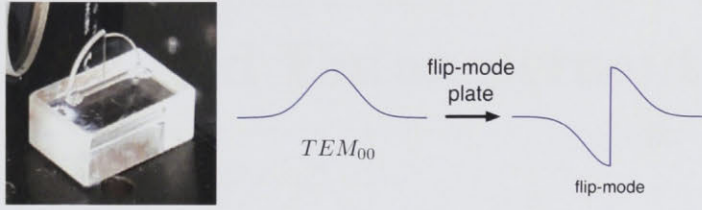


Figure 2.13: A flip mode plate, and the effect of this plate on a TEM_{00} mode shape.

improving the overlap between the modes substantially more than a beam misalignment, and improving the mode conversion efficiency from 30% to nearly 70%. The rest of the light can be represented as other modes in the Hermite-Gauss basis, and these are not resonant in the cavity at the same time. The overlap of TEM_{10} with TEM_{00} can be seen in Figure 2.14. Included are the cases of simple overlap, overlap with a tilt, and overlap with a flip mode plate on the TEM_{00} mode.

This concept of changing the mode shape to match a cavity can be extended to any mode required by using a spatial light modulator, or SLM. These interference devices can produce an arbitrary shape, to a rough approximation.

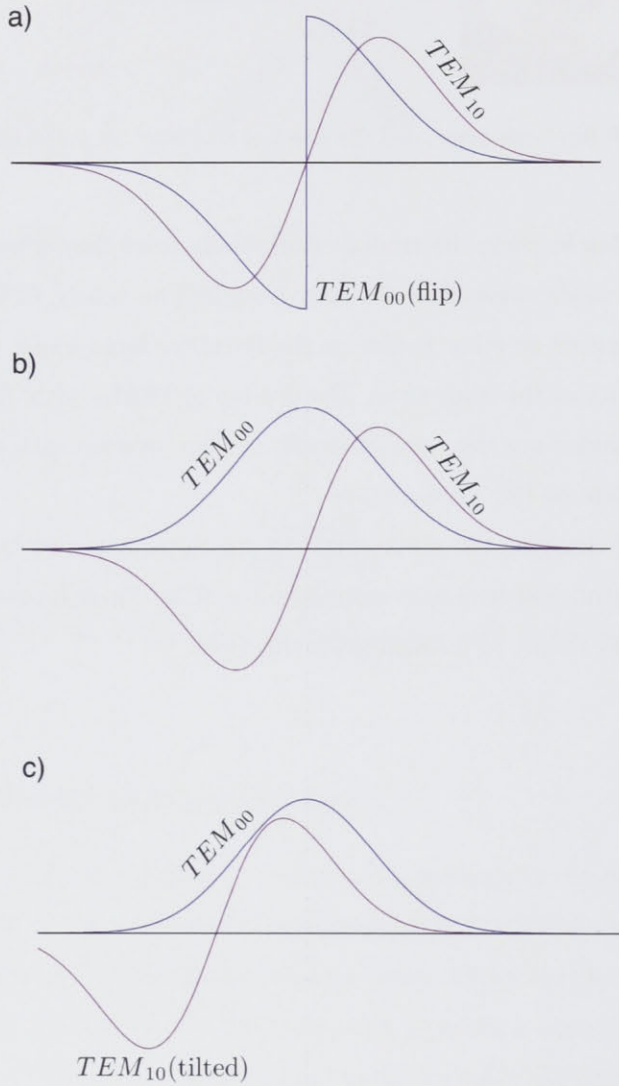


Figure 2.14: In order to efficiently use a cavity to transfer a mode, the input mode shape should be as close as possible to the required output mode shape. **a)** The overlap between TEM_{00} with a flip plate and TEM_{10} mode. **b)** The overlap between TEM_{00} mode and TEM_{10} mode, which across the profile ends up being zero. **c)** The overlap between TEM_{00} mode and TEM_{10} mode with a tilt between the two modes.

Squeezing and Entanglement

3.1 Introduction

The two quantum optics concepts central to this thesis are those of squeezing and entanglement. Squeezing has become ubiquitous in quantum optics experiments, and we will here discuss the requirements in order to produce such a state, and the effects of losses on squeezed modes once they are created.

All three experiments included in this thesis involve novel entanglement setups for continuous variable systems. The production of such states is discussed, and different methods of witnessing entanglement, namely EPR entanglement and Inseparability, are presented.

3.2 Nonlinearities

In order to create a squeezed state of light from a classical coherent state we first require some form of nonlinearity in the system. Such a nonlinearity can come from processes such as four wave mixing, second harmonic generation, or, as is used here, parametric downconversion. Ultimately, in this process the nonlinearity comes from the electric polarisation in the material that is used.

The electric polarisation is a measure of the density of the dipole moment within the material, and can be described mathematically in terms of the applied field E :

$$\mathcal{P} = \epsilon_0(\chi^{(1)}E + \chi^{(2)}E^2 + \chi^{(3)}E^3 + \dots) \quad (3.1)$$

where $\chi^{(n)}$ is the n^{th} order electric susceptibility. As a general rule, $\chi^{(n)}$ decreases rapidly as n increases. For most dielectric materials, known as linear materials, the first order susceptibility is sufficient in describing the interaction of the electric field with the material. When an electromagnetic field is sent through a linear dielectric, the electrons surrounding

the atoms experience this effect, with the dipole moment oscillating at the frequency of the incident radiation field. The oscillating polarisation then emits photons in the frequency of the polarisation field.

If the material is nonlinear, the polarisation of the material no longer changes in the same direct proportion to the applied field. If $\chi^{(2)}E^2$ is no longer negligible, then for a sinusoidal input field, $E = A_0\sin\Omega t$, there will be a component of the polarisation with a $\sin^2\Omega t$ dependence, that will oscillate at twice the frequency of the applied field. The oscillating polarisation then leads to the emission of the higher frequency photons as a result, in a process known as second harmonic generation, or frequency doubling. This process also works in reverse, where the stimulation of the material at the higher frequency results in the creation of photons at the lower frequency, and this is known as parametric down conversion.

3.3 Optical Parametric Amplification

In order to create a system where the nonlinear coupling occurs to a significant extent, there are two main requirements. These are:

1) a nonlinear material - a material with a high value for $\chi^{(2)}$ or $\chi^{(3)}$. Note that “high” is used in a relative sense; even in materials with a high nonlinearity the nonlinear polarisation response is small compared to the linear polarisation response for typical laboratory pump powers.

2) an input pump field of a sufficient intensity that $E^{(n)}$ is high enough to compensate for the weak higher order susceptibility.

The requirement for nonlinear materials can be found in the form of nonlinear crystals or atomic ensembles. Nonlinear crystals are the medium of interest for this thesis, and there are several types that can be used, such as lithium niobate, and potassium titanyl phosphate (KTP).

The input pump field must then travel through this crystal in order to induce the nonlinearity. Since the pump intensity inside the crystal is so important, there are several standard methods of increasing this intensity, such as focussing the beam at the centre of the crystal, or passing the pump field through the crystal multiple times. To produce squeezing using optical parametric amplification, these techniques are incorporated into the design of the *optical parametric amplifier*, or OPA.

Second order nonlinear materials allow a coupling between an optical field at a funda-

mental frequency and its second harmonic, at twice the frequency. The Hamiltonian for the this interaction, which governs both second harmonic generation and optical parametric amplification, is given by [16]:

$$\hat{H} = \hbar\Omega_1 a^\dagger a + \hbar\Omega_2 b^\dagger b + \frac{i\hbar\epsilon}{2} (a^{\dagger 2} b - a^2 b^\dagger) \quad (3.2)$$

for a fundamental field frequency of Ω_1 and a harmonic field frequency of Ω_2 , where ϵ is the coupling strength between the two different frequencies, and depends on the $\chi^{(2)}$ value for the material, as well as the phase-matching and the mode overlap inside the crystal. Looking at the sections of this equation, we can see that it is made up of the Hamiltonian for the fundamental field $\hbar\Omega_1 a^\dagger a$, the Hamiltonian for the second harmonic field $\hbar\Omega_2 b^\dagger b$, and the interaction term, describing the movement of photons between these two modes. It is the interaction term that describes parametric up-conversion and parametric down-conversion, and results in the change in the noise properties of the beam that is characteristic of squeezing.

3.3.1 OPA Cavity Equations

Using a model as shown in Figure 3.1, with the quantum Langevin equations, we can find the governing equations for the cavity, as in [24]. Here a is the fundamental mode and b is the harmonic mode, at twice the frequency of the fundamental mode.

$$\dot{a} = -\kappa_a a + \epsilon a^\dagger b + \sqrt{2\kappa_{in}^a} A_{in} + \sqrt{2\kappa_{out}^a} A_\nu + \sqrt{2\kappa_l^a} A_l \quad (3.3)$$

$$\dot{b} = -\kappa_b b - \frac{\epsilon}{2} a^2 + \sqrt{2\kappa_{in}^b} B_{in} + \sqrt{2\kappa_{out}^b} B_\nu + \sqrt{2\kappa_l^b} B_l \quad (3.4)$$

where $\kappa_{in,out,l}^{a,b}$ is the coupling term for the field a or b , for the three different mirrors in the cavity, and $\kappa_{a,b} = \kappa_{in}^{a,b} + \kappa_{out}^{a,b} + \kappa_l^{a,b}$. The mirrors used can have different transmission properties for the two different frequencies used, resulting in different values for the coupling terms.

For OPAs, the harmonic field, b , is always much stronger than the fundamental field, a . We can then assume that b is constant, since the light coupled from b to a is much smaller than the light in the field b . That is, we are assuming that the pump field remains undepleted throughout the process. We also introduce a nonlinear gain term, g , that is

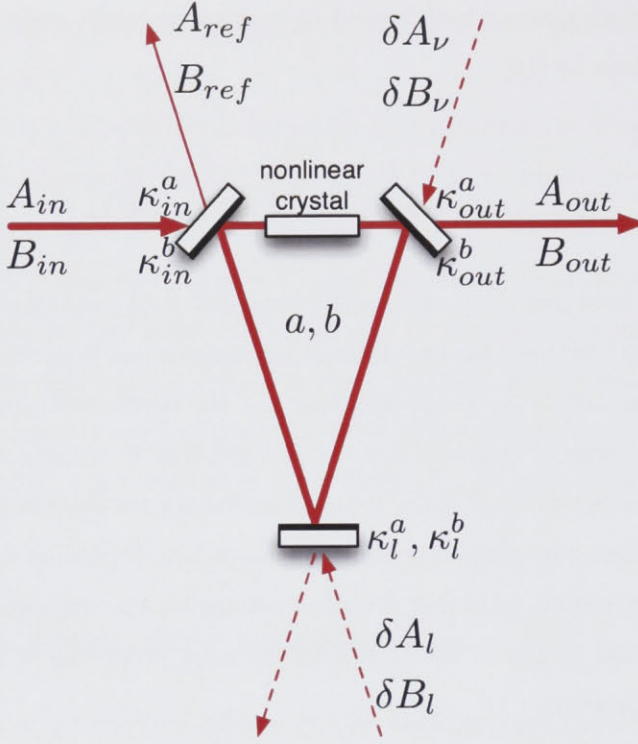


Figure 3.1: A model for an OPA, with input and output coupling, and a loss term. The fundamental and harmonic fields are labeled as a and b .

given by the product of the (constant) pump field b and the nonlinear interaction term ϵ . These simplifications leave us with a new description for the cavity:

$$\dot{a} = -\kappa_a a + g a^\dagger + \sqrt{2\kappa_{in}^a} A_{in} + \sqrt{2\kappa_{out}^a} A_\nu + \sqrt{2\kappa_l^a} A_l \quad (3.5)$$

If we look at the quadratures instead of the fields directly, we obtain:

$$\delta\dot{X}_a^+ = (g - \kappa_a) \delta X_a^+ + \sqrt{2\kappa_{in}^a} \delta X_{in}^+ + \sqrt{2\kappa_{out}^a} \delta X_\nu^+ + \sqrt{2\kappa_l^a} \delta X_l^+ \quad (3.6)$$

$$\delta\dot{X}_a^- = -(g + \kappa_a) \delta X_a^- + \sqrt{2\kappa_{in}^a} \delta X_{in}^- + \sqrt{2\kappa_{out}^a} \delta X_\nu^- + \sqrt{2\kappa_l^a} \delta X_l^- \quad (3.7)$$

which can be solved to find:

$$\begin{aligned} \delta\tilde{X}_{out}^+ &= \frac{(2\kappa_{out} - i\omega - \kappa + g)\delta\tilde{X}_\nu^+ + 2\sqrt{\kappa_{out}\kappa_{in}}\delta\tilde{X}_{in}^+ + 2\sqrt{\kappa_{out}\kappa_l}\delta\tilde{X}_l^+}{i\omega + \kappa - g} \\ \delta\tilde{X}_{out}^- &= \frac{(2\kappa_{out} - i\omega - \kappa - g)\delta\tilde{X}_\nu^- + 2\sqrt{\kappa_{out}\kappa_{in}}\delta\tilde{X}_{in}^- + 2\sqrt{\kappa_{out}\kappa_l}\delta\tilde{X}_l^-}{i\omega + \kappa + g} \end{aligned} \quad (3.8)$$

where all κ values now refer to the a field.

The variance of the output field for the two quadratures can then be obtained.

$$V_{out}^+ = 1 + \eta\eta_{esc} \frac{4g/\kappa + 4(\kappa_{in}/\kappa)(V_{in}^+ - 1)}{\omega^2/\kappa^2 + (1 - g/\kappa)^2} \quad (3.9)$$

$$V_{out}^- = 1 + \eta\eta_{esc} \frac{-4g/\kappa + 4(\kappa_{in}/\kappa)(V_{in}^- - 1)}{\omega^2/\kappa^2 + (1 + g/\kappa)^2} \quad (3.10)$$

where η_{esc} is the escape efficiency for the cavity, and is given by $\frac{\kappa_{out}}{\kappa}$, and η is the transmission on the beam after the cavity.

3.3.2 Nonlinear crystals

The squeezer must have an input pump beam - an intense beam at twice the frequency of the end squeezed beam. It can also have a *seed beam*, a low intensity beam at the same frequency as the end squeezed beam, resulting in a squeezed beam with a coherent amplitude. The squeezer with the seed beam is known as an OPA, or optical parametric amplifier, whereas the same squeezer without the seed beam is known as an OPO, or optical parametric oscillator. A coherent amplitude on the squeezed beam has some advantages, such as ease of alignment, and locking at a later point, but can also be a potential source of noise on the squeezed beam.

In order for efficient down conversion in the OPA, we require the phase matching condition to be met. This condition is essentially conservation of momentum for the three photons involved in the down conversion process. We require that:

$$k_1 + k_2 = k_3 \quad (3.11)$$

where k_3 is the wavevector of the photon in the harmonic field and k_2 and k_3 are the wavevectors of the two photons created in the fundamental field.

The phase matching condition can be achieved using the birefringence of nonlinear crystals, using what is termed with *critical* or *non-critical* methods. Noncritical phase matching occurs when the polarisation of one of the fields is aligned with the crystal axis. Critical phase matching, on the other hand, involves the adjustment of the angle of the linearly polarised light with respect to the crystal axis so that the effective refractive index for the harmonic and fundamental fields is suitable for phase matching.

The OPA used in these experiments has a MgO doped LiNbO₃ crystal, which is non-critically phase matched. The fields are of a Type I configuration - the photon in the

harmonic field is linearly polarised along one crystal axis, and the two photons created in the fundamental field have the orthogonal polarisation¹.

Since the refractive indices of the material depend on its temperature, the phase matching can then be achieved by slight adjustments to this temperature.

The Boyd-Kleinman factor [25] is a parameter that calculates the ideal size of the focus of the pump beam inside the crystal in order to obtain the highest possible level of squeezing. The ideal focus size is described by the focusing parameter, ξ , which is defined as:

$$\xi = \frac{\lambda l}{2\pi w_p^2} \quad (3.12)$$

where l is the length of the crystal, λ is the wavelength, and w_p is the ideal pump beam waist size in a vacuum. The optimal focusing parameter can be obtained by calculating the SHG field created in the nonlinear crystal for a given pump field. One first considers a series of thin slices of the crystal and the contribution from each of these slices to the second harmonic field. By integrating these contributions, the total SHG field is obtained, and the SHG efficiency can then be calculated as the focusing parameter is varied. For $\text{TEM}_{00} \rightarrow \text{TEM}_{00}$ conversion, the optimum SHG efficiency occurs when $\xi = 0.84$.

The seed beam, if one is used, should then ideally have a waist size $w_s = \sqrt{2}w_p$.

3.3.3 Loss on a Squeezed Beam

All of the squeezed states in the experiments of this thesis are amplitude squeezed states, indicating an increase in order with time and hence a sub-Poissonian distribution of photons in the beam. A loss then corresponds to random photons being removed from the squeezed beam, decreasing the order and hence the degree of squeezing.

Any loss on the beam can be modelled by a beamsplitter, previously discussed in Section 2.5. Starting with a beam X_1 , a loss of magnitude $1 - \eta$ can be modelled with a beamsplitter of transmission η , and the vacuum mode that is coupled in then results in the a beam with new squeezing characteristics, X_2 , as seen in Figure 3.2.

Note that the implication of this, for a system where the squeezing and antisqueezing

¹Type II phase matching has a photon of the harmonic field with one linear polarisation aligned with the crystal axis producing two photons - one of which has the same polarisation as the harmonic, and one orthogonal to this.

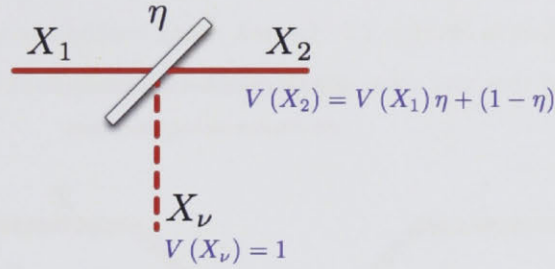


Figure 3.2: A squeezed beam with a loss applied to it can be modelled as having an original variance, V^+ and V^- , and having a vacuum mode introduced by way of a beamsplitter.

can be measured accurately, without being compromised by excess noise or locks that aren't functioning correctly, is that the squeezing and antisqueezing on a beam, V^+ and V^- , can also be written in terms of an original amount of squeezing V_0 , and the total loss that has been experienced by the beam, $1 - \eta$. The original amount of antisqueezing is then $\frac{1}{V_0}$, and from the measured squeezing and antisqueezing values, the original squeezing and the total loss can be found as:

$$V_0 = - \left(\frac{V^+ - 1}{V^- - 1} \right) \quad (3.13)$$

$$\eta = \frac{V^+ + V^- - V^+V^- - 1}{V^+ + V^- - 2}. \quad (3.14)$$

These equations assume that there is no additional classical noise on the squeezed beam.

3.4 EPR and Inseparability

Once a squeezed state has been produced, it can be used to perform sub quantum noise measurements directly, or it can be used as a component in a larger experiment. Here, we look at the use of squeezed sources to create entangled continuous variable states - states with two modes, where a measurement of one mode affects the state of the other mode. Such states result in correlations between two modes that surpass the correlations that can be measured in purely classical systems. In order to produce an entangled system, we require a superposition of two states, where at least one of these states has sub-quantum noise statistics.

One method for providing the superposition state involves mixing two beams on a beamsplitter, as detailed in Section 2.5. Indeed, many continuous variable entanglement setups can be pictured this way, even if it does not accurately reflect the physical setup.

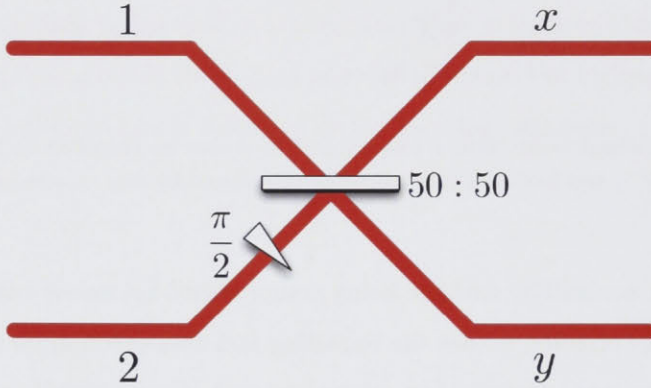


Figure 3.3: A standard entanglement setup, with two input beams 1 and 2 mixed using a 50:50 beamsplitter with a $\pi/2$ phase shift, producing two output beams x and y .

For the standard entanglement setup shown in Figure 3.3, with two input beams, 1 and 2 mixed using a 50:50 beamsplitter with a $\pi/2$ phase shift, the output beams x and y can be described as:

$$X_x^\pm = \frac{1}{2} (\pm X_1^+ + X_2^+ + X_1^- \mp X_2^-) \quad (3.15)$$

$$X_y^\pm = \frac{1}{2} (X_1^+ \pm X_2^+ \mp X_1^- + X_2^-) \quad (3.16)$$

as can be seen in Appendix A.

In essence, continuous variable entanglement involves correlations between two (or more) modes, when measured on two conjugate observables. Note that in this context when the word ‘mode’ is used, it refers to independently propagating channels, and can include spatially separated modes, different spatial modes, different frequency modes, or orthogonal polarisations, as shown in Figure 3.4. Each of these systems of modes has two distinct parts - a signal can be imparted onto one mode without affecting the other. The correlations between the modes that are ultimately used to characterise the entanglement can be represented by plotting the measurements on each mode parametrically. The shape of the contours from the resulting distribution can then be used to determine the strength

of the correlations.

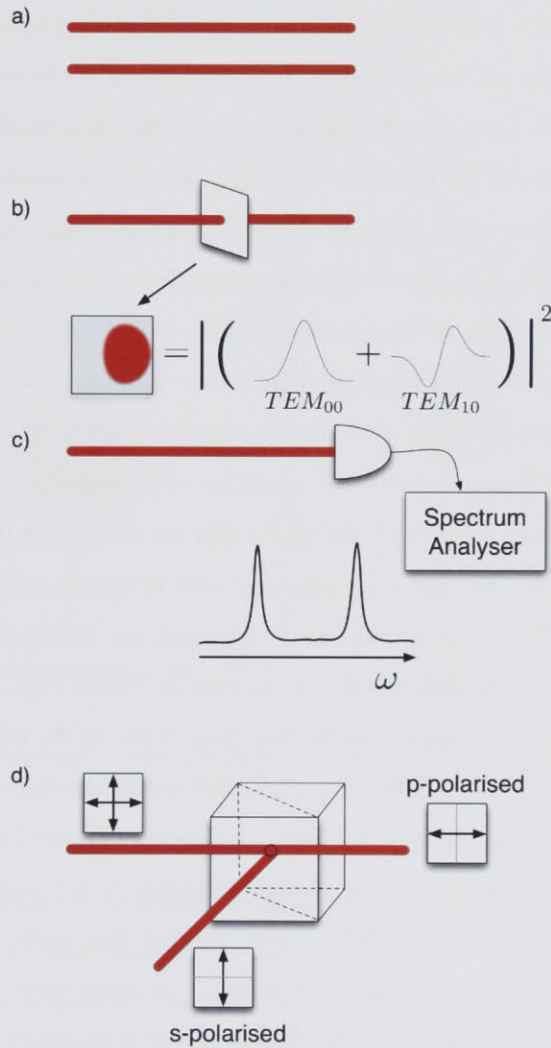


Figure 3.4: There are several types of modes, or independent channels, that can be entangled. These include **a)** spatially separated modes, **b)** different spatial modes copropagating on one beam, **c)** different frequency modes, or **d)** orthogonal polarisation modes.

For two quantum noise limited beams that are combined on a beamsplitter, the resulting output beams, while classically identical, are uncorrelated at a quantum level. The instantaneous fluctuations that occur in such a system are represented in the traces in Figure 3.5a. Since these are uncorrelated, the combination of the two traces by addition or subtraction gives the same variance, as does any normalised linear combination of the two beams. If the values of the two measurements are plotted parametrically, this results in a circular distribution as seen in Figure 3.5b. Each point in this diagram represents one pair of data points, δ_x and δ_y , where the data were taken in the same integration time. If we then draw a line showing the standard deviation σ of the distribution for all possible angles, the resulting circle defines our quantum noise limit for such a system², as shown in Figure 3.5c. Because the input state has the same noise statistics independent of the quadrature (provided the input states are quantum noise limited), the distribution of the mixed modes looks identical for both the phase and the amplitude quadrature.

If the two input coherent states are replaced with squeezed states, and mixed with a phase difference of $\pi/2$, the two modes, now entangled, are each still noisy, but the noise on each of the modes is now anti-correlated, as seen in Figure 3.6a. The normalised sum of the two sets of points then fluctuates by less than either of the individual traces, while the difference fluctuates more. This means that if each pair of points is again plotted parametrically, an elliptical shape will result, as shown in Figure 3.6b and c. Note that, as with squeezing, the Heisenberg Uncertainty Principle is not being violated with the measurement, that falls below the QNL, since making this same measurement on the other quadrature will be above the QNL by at least the same factor as this measurement is under. The system represented by the ellipses shown is assumed to be lossless, and is symmetric, so the two squeezers being mixed are identical.

From the shape of the ellipse that has been obtained, several values useful for categorising the state can be found, as shown in Figure 3.7. This includes (for a given quadrature) the standard deviation for either of the entangled modes on their own (σ_x and σ_y), and the normalised standard deviations of the sum ($\sigma_{x+y} = \sigma \left(\frac{X_x + X_y}{\sqrt{2}} \right)$ - here lower than the QNL) and difference (σ_{x-y}) of the modes. From the standard deviations, we can find the variances of the modes, as discussed in Section 2.2 from $V = \sigma^2$.

Given that we're now looking at states that aren't coherent, the shape of the distri-

²Note that instead of using the standard deviation to define the quantum noise, any arbitrary contour may be chosen - for example the 7σ contour, and this would simply result in a renormalisation to the new quantum noise limit, due to the properties of Gaussian noise distribution.

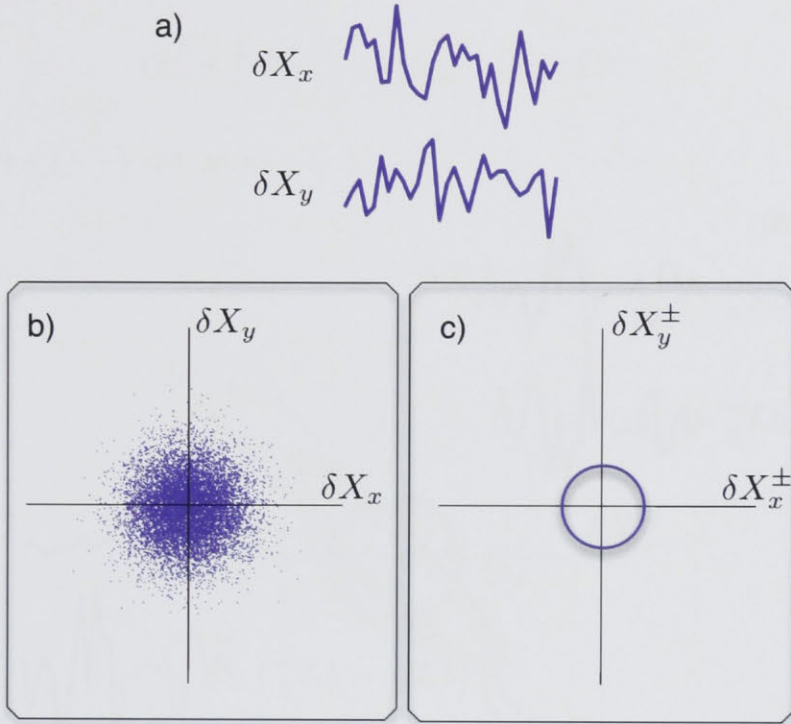


Figure 3.5: In the unentangled case, the noise on the beams δX_x and δX_y is uncorrelated, as seen in **a)**, resulting in a circular distribution, seen in **b** and **c**.

bution changes for different quadratures measured. The phase quadrature will have a correlation between the noise traces, resulting in an ellipse at 90° to that in the amplitude quadrature case. The ellipses for the different quadratures is shown in Figure 3.8. From each cross section, similar noise statistics can be inferred.

The noise statistics of the entangled state can be visualised using such methods, but it is not useful for characterising the state in a complete and concise way. For this, we will introduce the correlation matrix. Light with Gaussian statistics, as we generally encounter in the continuous variable regime, can be fully characterised by an appropriate correlation matrix. For a system with two modes, x and y , this correlation matrix is defined as

$$CM = \begin{bmatrix} C_{xx}^{++} & C_{xx}^{+-} & C_{xy}^{++} & C_{xy}^{+-} \\ C_{xx}^{-+} & C_{xx}^{--} & C_{xy}^{-+} & C_{xy}^{--} \\ C_{yx}^{++} & C_{yx}^{+-} & C_{yy}^{++} & C_{yy}^{+-} \\ C_{yx}^{-+} & C_{yx}^{--} & C_{yy}^{-+} & C_{yy}^{--} \end{bmatrix} \quad (3.17)$$

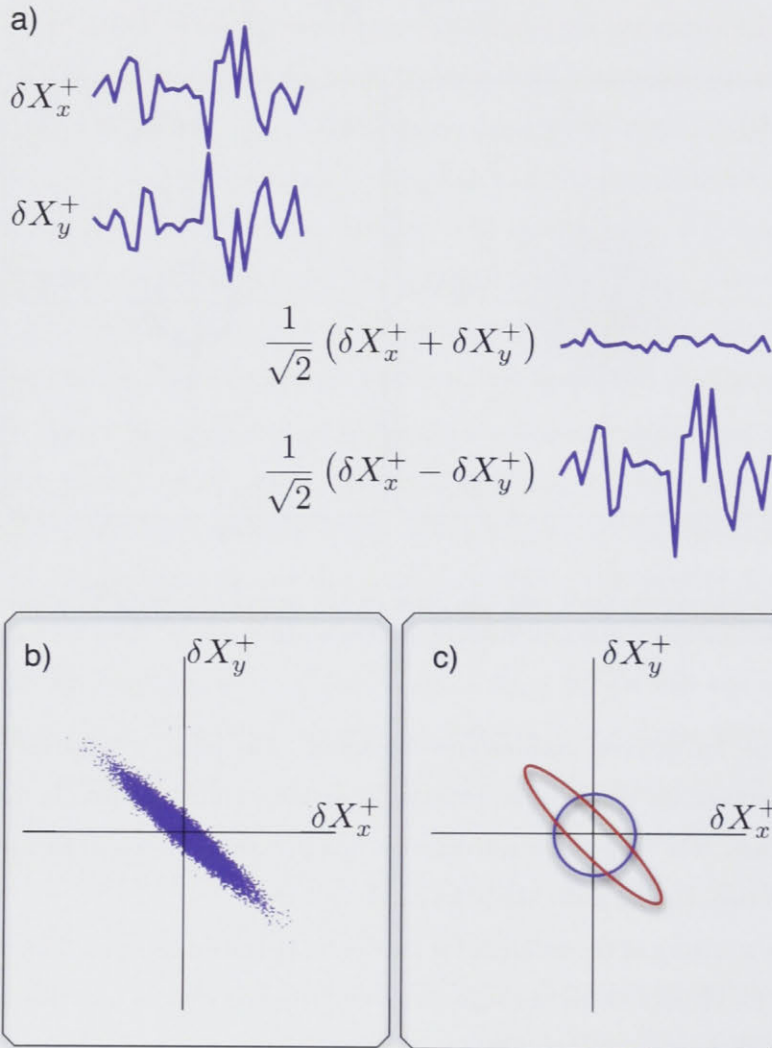


Figure 3.6: In this case, X_x and X_y are correlated to below the QNL, resulting in an elliptical distribution. In part c), the distribution for this case is shown in red, and the quantum noise limit is shown in blue for comparison.

Each element in the matrix is defined as:

$$C_{mn}^{kl} = \frac{1}{2} \langle \hat{X}_m^k \hat{X}_n^l + \hat{X}_n^l \hat{X}_m^k \rangle - \langle \hat{X}_m^k \rangle \langle \hat{X}_n^l \rangle \quad (3.18)$$

where $\{k, l\} \in \{+, -\}$ and $\{m, n\} \in \{x, y\}$.

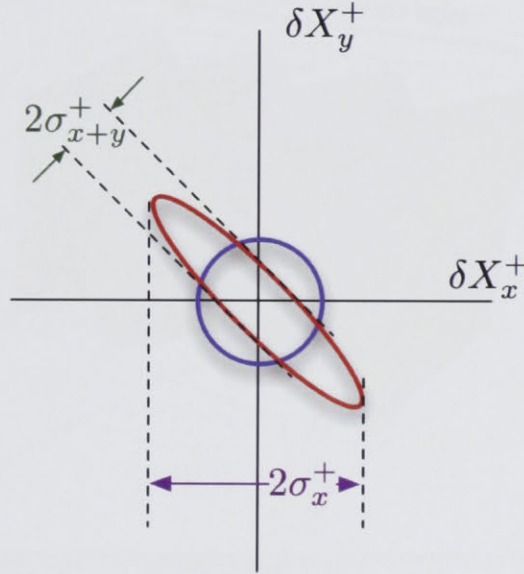


Figure 3.7: From the elliptical distribution, we can find σ_x^+ , σ_y^+ , and combinations of these, such as σ_{x+y}^+ .

Some of these elements correspond directly to the variances that can be found from the ellipses shown above - for instance C_{xx}^{++} is V_x^+ .

Note that although the matrix uses the amplitude and phase quadratures explicitly, the state can equivalently be characterised using the more general quadratures, θ and $\theta + \pi/2$.

While the required information about the state is contained in the correlation matrix, it is not immediately obvious by looking at the matrix whether the state is entangled. Entanglement is usually verified with one of several definitions. The two measurements that are of interest in this thesis are the Inseparability of a system, and the EPR paradox.

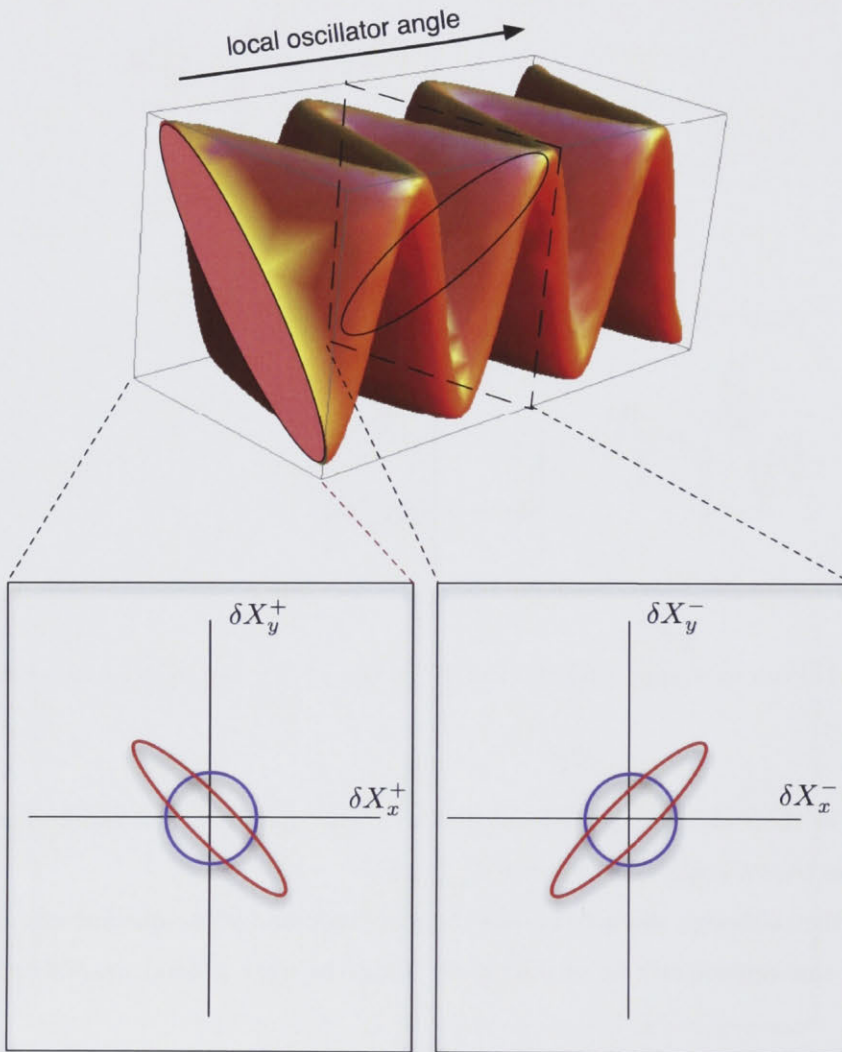


Figure 3.8: The correlation ellipses for a continuously varying quadrature (local oscillator angle). The phase and amplitude quadrature cross-sections are shown.

3.4.1 Inseparability criterion

One criterion that is both sufficient and necessary for the existence of entanglement is the Inseparability of a system. A system is separable if the wavefunction of a system can be written in such a way that it is the product of the wavefunctions of the component modes. That is, a system is separable if it can be written as:

$$|\psi\rangle = |\psi_1\rangle \otimes |\psi_2\rangle. \quad (3.19)$$

It was found by Duan et. al. [26] that there is a lower bound to the total variance for any separable system, and that if this lower bound is violated, the system is inseparable, and therefore entangled. Given two EPR type operators, as in [1],

$$\hat{u} = |k|\hat{X}_x^+ + \frac{1}{k}\hat{X}_y^+ \quad (3.20)$$

$$\hat{v} = |k|\hat{X}_x^- - \frac{1}{k}\hat{X}_y^- \quad (3.21)$$

where k is a real number, then for all separable states,

$$\mathcal{I} = \frac{V_u^+ + V_v^-}{2(k + 1/k)} \geq 1. \quad (3.22)$$

In order to make sure that any entanglement that exists in a system is measured, the measured correlation matrix can be put into this form via local linear Bogoliubov operations, by transforming into Standard form I and Standard form II. Duan et. al. first transform the correlation matrix into *standard form I*, a matrix independent of the quadratures initially measured. Standard form I then has the format:

$$CM' = \begin{bmatrix} n & 0 & c & 0 \\ 0 & n & 0 & c' \\ c & 0 & m & 0 \\ 0 & c' & 0 & m \end{bmatrix} \quad (3.23)$$

The elements n , m , c , and c' are found using the determinants of differ-

ent parts of the original correlation matrix, such that $\det \begin{pmatrix} C_{xx}^{++} & C_{xx}^{+-} \\ C_{xx}^{-+} & C_{xx}^{--} \end{pmatrix} = n^2$,
 $\det \begin{pmatrix} C_{yy}^{++} & C_{yy}^{+-} \\ C_{yy}^{-+} & C_{yy}^{--} \end{pmatrix} = m^2$, $\det \begin{pmatrix} C_{xy}^{++} & C_{xy}^{+-} \\ C_{xy}^{-+} & C_{xy}^{--} \end{pmatrix} = \det \begin{pmatrix} C_{yx}^{++} & C_{yx}^{+-} \\ C_{yx}^{-+} & C_{yx}^{--} \end{pmatrix} = cc'$, and
 $\det(CM) = (mn - c^2)(nm - c'^2)$

This transformation in effect rotates the quadrature of the measurements to the quadrature with the most pronounced ellipses, with the highest correlations. If the original quadratures measured are $\pi/4$ from the ideal quadratures for seeing the entanglement, then the original ellipses will look like circles, as can be seen in Figure 3.8. Following the transformation, the elements of the correlation matrix are the same as the measurement would have originally yielded if the amplitude and phase quadratures had been measured.

Changing the matrix into *Standard Form II* involves the application of squeezing operations r_1 and r_2 . Using the elements from Standard Form I, the following two equations must be solved to find the appropriate values for r_1 and r_2 .

$$\frac{n/r_1 - 1}{nr_1 - 1} = \frac{m/r_2 - 1}{mr_2 - 1} \quad (3.24)$$

$$|c|\sqrt{r_1 r_2} - |c'|\sqrt{r_1 r_2} = \sqrt{(nr_1 - 1)(mr_2 - 1)} - \sqrt{(n/r_1 - 1)(m/r_1 - 1)} \quad (3.25)$$

There are generally several solutions to these equations, and the required values for r_1 and r_2 are those that yield the best (lowest) value for \mathcal{I} . Using these values, Standard form II is then:

$$CM'' = \begin{bmatrix} nr_1 & 0 & c\sqrt{r_1 r_2} & 0 \\ 0 & n/r_1 & 0 & c'/\sqrt{r_1 r_2} \\ c\sqrt{r_1 r_2} & 0 & mr_2 & 0 \\ 0 & c'/\sqrt{r_1 r_2} & 0 & m/r_2 \end{bmatrix} \quad (3.26)$$

Values from this matrix can then have the Inseparability criterion applied to them. The system is inseparable, and therefore entangled, if:

$$\mathcal{I} = \frac{C_I^+ + C_I^-}{2(k + 1/k)} < 1 \quad (3.27)$$

where

$$C_I^+ = k(nr_1) + \frac{1}{k}(mr_2) - 2|c\sqrt{r_1r_2}| \quad (3.28)$$

$$C_I^- = k\left(\frac{n}{r_1}\right) + \frac{1}{k}\left(\frac{m}{r_2}\right) - 2\left|\frac{c'}{\sqrt{r_1r_2}}\right| \quad (3.29)$$

and

$$k = \sqrt{\frac{mr_2 - 1}{nr_1 - 1}} = \sqrt{\frac{\frac{m}{r_2} - 1}{\frac{n}{r_1} - 1}} \quad (3.30)$$

For a symmetric case, with identical squeezers and a 50:50 beamsplitter, the end value that is found is given by:

$$\mathcal{I} = \sqrt{V_{x\pm y}^+ V_{x\mp y}^-} \quad (3.31)$$

which can be found directly from two measurements, without the need to find all of the components of the correlation matrix. At worst, this is an unoptimised form of Inseparability, and it is a sufficient but not a necessary condition for entanglement.

These two measurements required to find the unoptimised Inseparability can be found from the correlation ellipses for the phase and amplitude quadrature of an entangled system, as seen in Figure 3.9.

For a symmetric system, with two squeezed modes with initial amount of squeezing V_0 , the measurement of Inseparability becomes less marked with loss. As a function of the initial amount of squeezing and the transmission η , the Inseparability is given by:

$$\mathcal{I} = \eta V_0^+ + (1 - \eta) \quad (3.32)$$

3.4.2 EPR entanglement

The originally conceived form of entanglement, the EPR paradox with a pair of particles, can also be applied to continuous variable systems [4]. It involves the measurement of one of the entangled modes to attempt to predict the behaviour of the second mode to

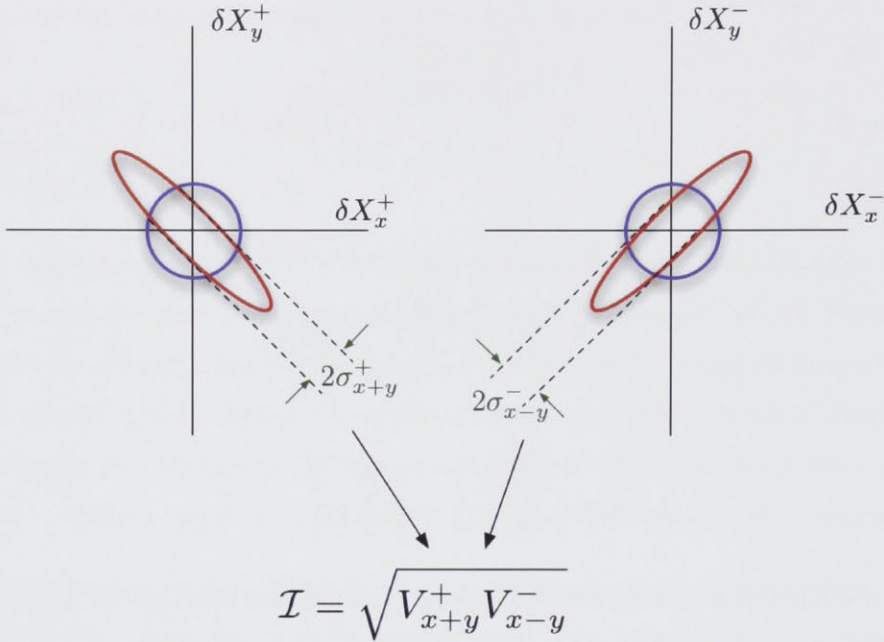


Figure 3.9: From the elliptical distribution, we can find σ_{x+y}^+ and σ_{x-y}^- , and from this, the unoptimised Inseparability can be deduced.

a higher degree of accuracy than can be measured by classical means. This results in an apparent violation of the Heisenberg Uncertainty Principle, since this measurement is more precise than allowed for an instantaneous measurement in two conjugate variables. Mathematically, EPR entanglement is achieved if the following inequality is satisfied.

$$\epsilon = V_{x|y}^+ V_{x|y}^- < 1 \quad (3.33)$$

where the conditional variance $V_{x|y}$ denotes the variance of a mode x given a measured value of y , and is found by:

$$V_{x|y} = \min_g \langle (\delta X_x - g \delta X_y)^2 \rangle \quad (3.34)$$

$$= V_x - \frac{\langle \delta X_x \delta X_y \rangle^2}{V_y} \quad (3.35)$$

The EPR value can therefore be measured using the values from the correlation matrix.

Alternatively, as with the simplified version of the Inseparability measure, the EPR measure can be obtained directly from correlation ellipses already discussed. The conditional deviation $\sigma_{x|y}$ can be found from the intercepting points of the ellipse with the δX_x axis, as shown in Figure 3.10. From these conditional deviation values for two orthogonal quadratures, the conditional variances and hence the value for ϵ can be found.

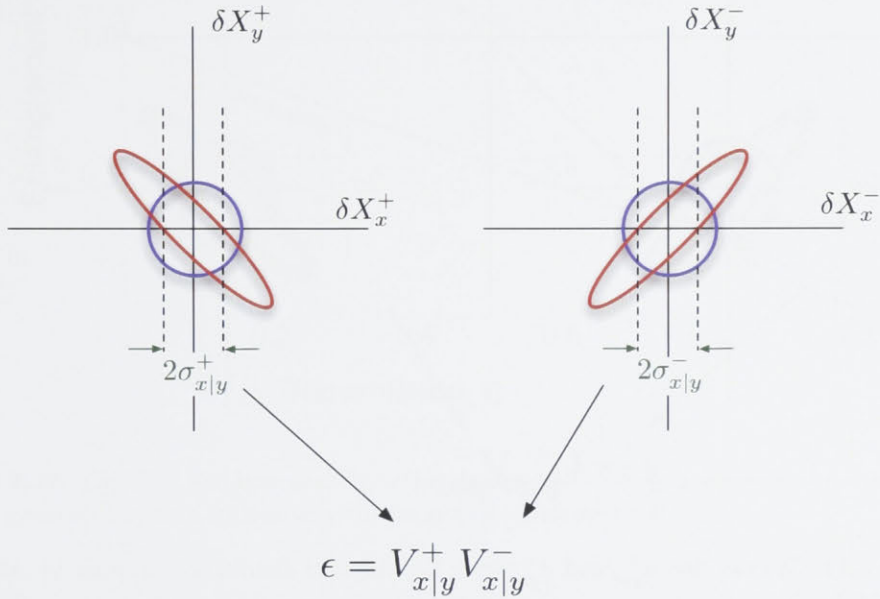


Figure 3.10: From the elliptical distribution, we can find $\sigma_{x|y}^+$ and $\sigma_{x|y}^-$, and from this, the EPR paradox can be measured.

Unlike Inseparability, measurement of the EPR paradox provides a sufficient but not necessary condition for entanglement. For a symmetric system, the degree of EPR paradox that can be measured can be written in terms of the initial amount of squeezing V_0^+ , and the total transmission of the system η , as follows.

$$\epsilon = 4 \left(1 + \eta + \frac{2\eta - 1}{\eta (V_0^+ + 1/V_0^+ - 2) + 2} \right)^2. \tag{3.36}$$

This result is derived in Appendix 1.

For asymmetric systems, this result no longer holds, and there emerge two possible values that can be obtained for the EPR value. These values arise because of the asymmetric nature of the EPR criterion itself: it is the prediction of one object's behaviour based on

a measurement made on a second object. In terms of two potentially entangled arms x and y , this means that y can be measured and x predicted based on this, as has been considered thus far, or x can be measured and y predicted. The measurement required to obtain the second EPR value, $\epsilon_{y|x}$, is shown graphically in Figure 3.11.

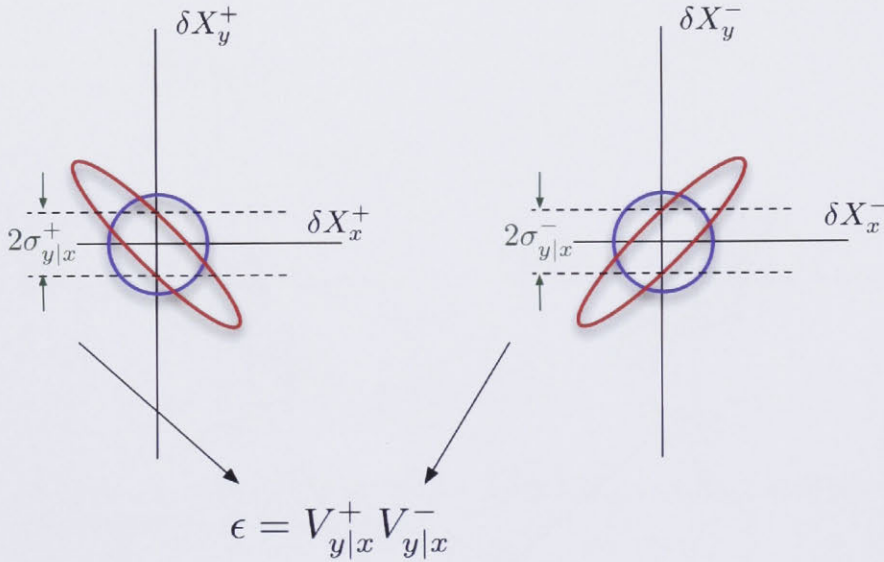


Figure 3.11: We can find $\sigma_{y|x}^+$ and $\sigma_{y|x}^-$ from the elliptical distribution in order to obtain the second EPR value, $\epsilon_{y|x}$.

Plotting the theoretical values of EPR and Inseparability for different transmission values η , as can be seen in Figure 3.12 shows that whereas Inseparability still indicates quantum behaviour as the loss approaches 100%, EPR entanglement requires that the total loss on the system be less than 50%³, as can be seen in Figure 3.12. This is one of the characteristics that makes EPR entanglement more difficult to measure than Inseparability, and leads to the rule-of-thumb that 3dB of squeezing is required in order measure EPR entanglement.

The reason for the greater squeezing requirement for measuring EPR entanglement can be seen in a geometric approximation from the correlation ellipses, shown in Figure 3.13. For Inseparability entanglement to be observable, we need for $V_{x+y}^+ V_{x-y}^- < 1$. For a symmetric system, this requirement ultimately means that $\sigma_{x+y}^+ < 1$, which requires that the initial amount of noise on the input modes σ_0^+ be less than one; that is, the input

³This is not true for the case of asymmetric systems, which are discussed and investigated in Chapter 6.

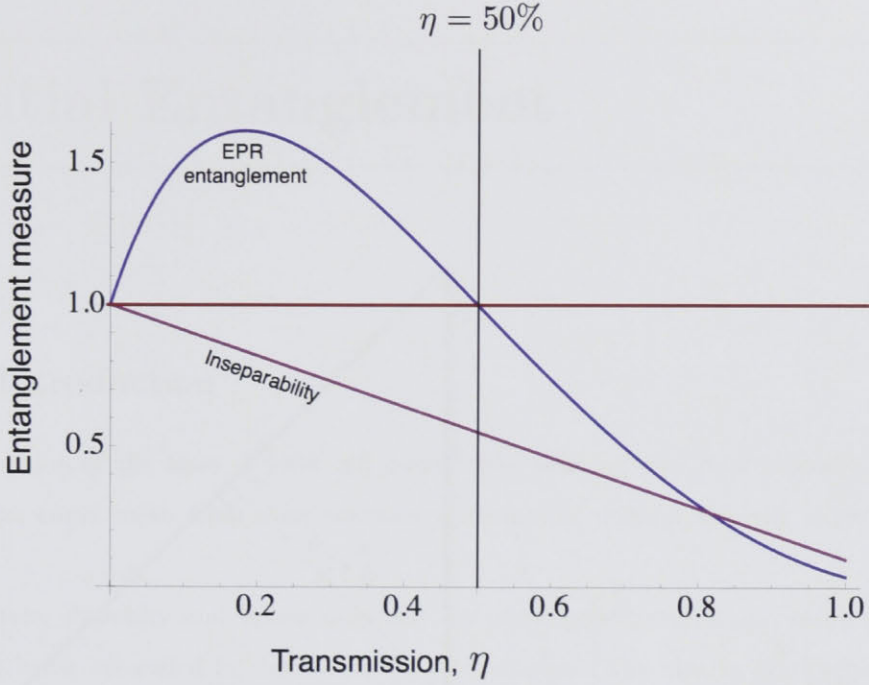


Figure 3.12: The EPR and Inseparability entanglement measured as a function of transmission, η , for a symmetric system with an original amount of squeezing 10dB.

modes must be squeezed.

Looking at a small section of the correlation ellipse that can be approximated to a triangle, shown in Figure 3.13, it can be seen that $\sigma_{x+y}^+ \approx \frac{1}{\sqrt{2}}\sigma_{x|y}^+$.

In order to measure EPR entanglement in a symmetric system, we need to have

$$\begin{aligned}
 \sigma_{x|y}^+ &< 1 \\
 \Rightarrow \sqrt{2}\sigma_{x+y}^+ &< 1 \\
 \Rightarrow \sqrt{2}\sigma_0^+ &< 1 \\
 \Rightarrow \sigma_0^+ &< \frac{1}{\sqrt{2}} \\
 \Rightarrow V_0^+ &< \frac{1}{2}
 \end{aligned} \tag{3.37}$$

This is equivalent to requiring 3dB of squeezing, as is generally needed for EPR entanglement measurements.

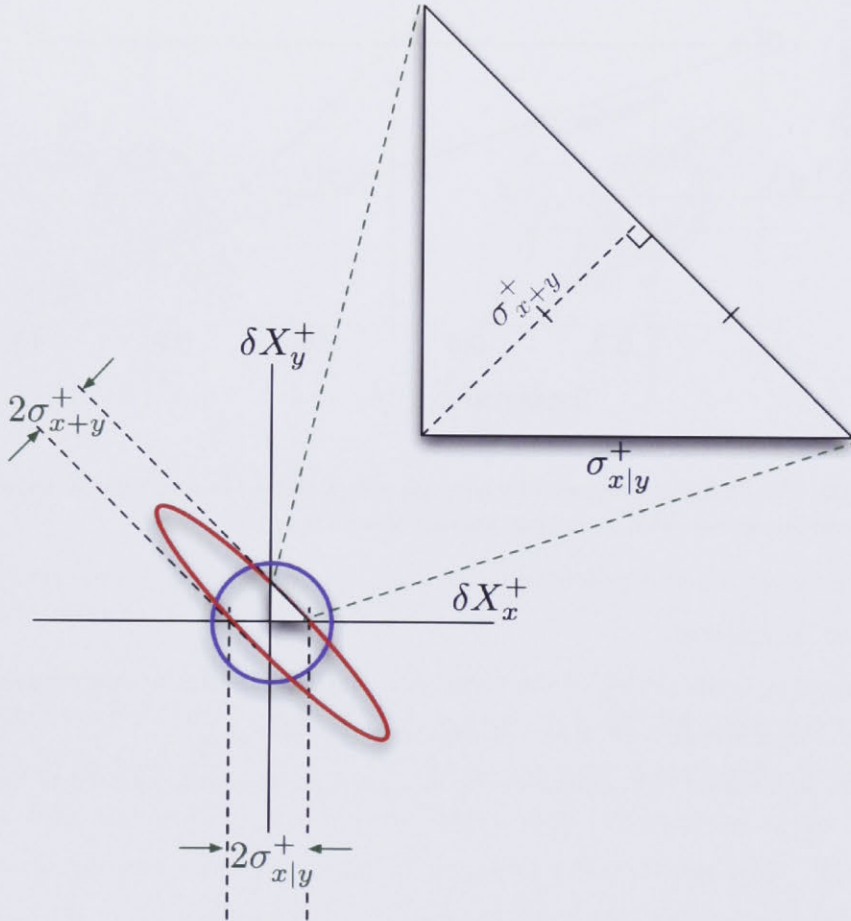


Figure 3.13: Looking at a small section of the correlation ellipse that can be approximated to a triangle, it can be seen that $\sigma_{x+y}^+ = \frac{1}{\sqrt{2}}\sigma_{x|y}^+$. Given that Inseparability entanglement can be observed for any initial degree of squeezing, this shows why the rule of thumb for needing 3dB of squeezing in order to observe EPR entanglement holds.

Spatial Entanglement

4.1 Introduction

The invention of the laser in 1958 [27] meant that many of the ideas behind quantum mechanics could move from their previously theoretical domain into the experimental world.

Einstein, Podolsky and Rosen originally envisioned the position and momentum of particles being entangled in their Gedanken experiment. The idea in this section is to apply this concept of entanglement to the now ubiquitous medium of laser beams. The purpose, then, is to create a system where the position and momentum of two laser beams are entangled.

This chapter will first cover how to measure the position and momentum for laser beams at a quantum noise limited level. We will then discuss how this can be translated into a functioning experiment with EPR entanglement between the position and momentum of two beams, and present the results that were found.

This work has been published in Science 321, 541 (2008).

4.2 Displacement and tilt of a beam

Before we can entangle the position and momentum of laser beams, we must first discuss how the displacement and tilt of a beam can be measured, and find the quantum noise limit for the position and momentum of a laser beam.

4.2.1 Classical displacement and tilt of a beam

While we can create laser beams in higher order spatial modes, a laser will generally produce a TEM_{00} mode shape. It is this mode shape whose position and momentum we will look at for this experiment.

If we consider a TEM_{00} beam, we can define a displacement d from the beam's average position d_0 , as seen in Figure 4.1. We can also define the tilt θ from the average direction of the laser beam. If we wish to measure the position of the beam, this is then equivalent to measuring this displacement, and similarly a measurement of the tilt of the beam is equivalent to measuring the transverse momentum of the beam.

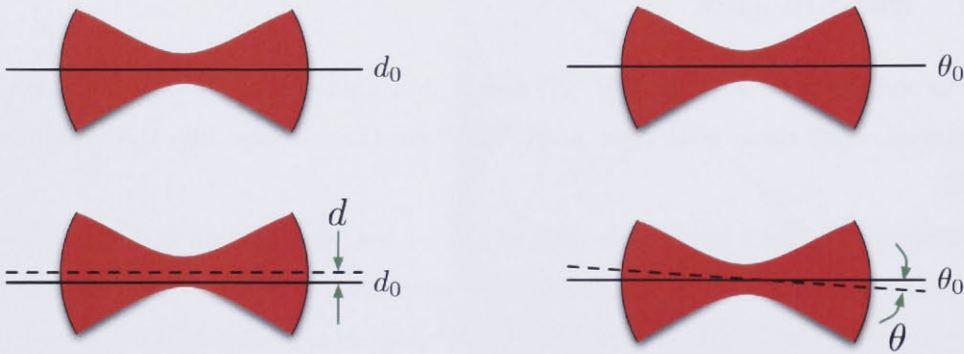


Figure 4.1: A laser beam has uncertainty in its position and angle in normal operation. We look at small displacements from the average position d and small angles from the normal direction θ .

For an laser beam originally described by the field profile $E(x)$, the electric field profile for the beam displaced by a distance d can be described by the Taylor expansion:

$$E_d(x) = E(x) + d \frac{\partial E(x)}{\partial x} + \frac{d^2}{2} \frac{\partial^2 E(x)}{\partial x^2} + \dots \quad (4.1)$$

For a small displacement d , the higher order terms are negligible, and we're left with:

$$E_d(x) \approx E(x) + d \frac{\partial E(x)}{\partial x}. \quad (4.2)$$

Similarly, if we look at the tilt, or transverse momentum, of the beam, we find:

$$E_p(x) = e^{\frac{i2\pi x \sin \theta}{\lambda}} E(x \cos \theta) \quad (4.3)$$

which can be simplified, for small angles, to:

$$E_p(x) = E(x) + ipxE(x). \quad (4.4)$$

Note that θ and p are related by $p = \frac{2\pi \sin \theta}{\lambda} \approx \frac{2\pi\theta}{\lambda}$ for small angles.

If we write these expressions in terms of the mode components themselves, we arrive at the expression [28]:

$$E_{d,p}(x) = A_0 \left[u_0(x) + \left(\frac{d}{w_0} + i\frac{w_0 p}{2} \right) u_1(x) \right] \quad (4.5)$$

where $u_n(x)$ represent the mode profiles for a given transverse basis, and w_0 is the beam waist. The implication of this expressions is that a tilt or displacement of a TEM₀₀ beam in the the x direction can be measured by detecting the TEM₁₀ component of the beam¹. The displacement of the beam can be measured on the ‘in phase’ part of the TEM₁₀ field, relative to the TEM₀₀ carrier mode. The information about the tilt of the beam is contained in the TEM₁₀ mode when the phase is ‘in quadrature’ relative to the TEM₀₀ mode, as signified by the ‘ i ’ in Equation 4.4².

These approximations are only valid for small displacements and tilts of the laser beam. For the position calculation, the assumption is made that $d \ll w_0$. For the momentum calculation, it is assumed that the tilt is small ($\theta < \lambda/w_0$) and that the paraxial approximation applies, so $\lambda \ll w_0$.

4.2.2 Heisenberg limit

The most familiar example of the Heisenberg limit for most physicists is the position-momentum inequality, $\Delta x \Delta p \geq \frac{\hbar}{2}$, which reflects the limitation on the accuracy of simultaneous measurements on the position and momentum of an object. Here we will identify the Heisenberg limit for the position and momentum of laser beams by first looking at the positive frequency component of the electric field operator:

$$\epsilon^+(x) = i\sqrt{\frac{\hbar\omega}{2\epsilon_0 c T}} \sum_{n=0}^{\infty} \hat{a}_n u_n(x) \quad (4.6)$$

¹Similarly, a tilt or displacement in the y direction can be measured by detecting the TEM₀₁ component of the beam.

²In order to make this measurement, the detector plane must be aligned carefully. The waist of the TEM₀₀ beam in question must be imaged onto the detector plane.

Since we are primarily interested in experimentally measurable quantities, we can rewrite the annihilation operator in terms of the amplitude and phase quadratures.

$$\epsilon^+(x) = i\sqrt{\frac{\hbar\omega}{2\epsilon_0cT}} \sum_{n=0}^{\infty} \left(\frac{\hat{X}_n^+ + i\hat{X}_n^-}{2} \right) u_n(x) \quad (4.7)$$

If we expand this expression for a bright TEM₀₀ mode with mean photon number N

$$\begin{aligned} \epsilon^+(x) = & \quad (4.8) \\ i \sqrt{\frac{\hbar\omega}{2\epsilon_0cT}} & \left[\sqrt{N} \left(u_0(x) + \left(\frac{d}{w_0} + i\frac{w_0p}{2} \right) u_1(x) \right) + \sum_{n=0}^{\infty} \left(\frac{\delta\hat{X}_n^+ + i\delta\hat{X}_n^-}{2} \right) u_n(x) \right] \end{aligned}$$

where d and p are the mean values of the position and momentum operators, $d = \langle \hat{x} \rangle$ and $p = \langle \hat{p} \rangle$. We can identify the TEM₁₀ components of Equation 4.9 to arrive at the position and momentum operators for the bright TEM₀₀ mode:

$$\begin{aligned} \hat{x} &= \frac{w_0}{2\sqrt{N}} \hat{X}_1^+ \\ \hat{p} &= \frac{1}{w_0\sqrt{N}} \hat{X}_1^- \end{aligned} \quad (4.9)$$

as shown in [29]. From here, the commutation relation can be shown to be:

$$[\hat{x}, \hat{p}] = \frac{i}{N}. \quad (4.10)$$

From Equation 4.9, we can see that by replacing the vacuum mode that originally fills the TEM₁₀ space with an amplitude-squeezed TEM₁₀ mode, any displacement of the bright TEM₀₀ mode can then be measured more accurately than the standard quantum limit would otherwise allow in what is referred to as a position-squeezed beam. A position-squeezed beam was first produced by Treppe et. al. [30, 31] in 2002 using this same method, and measurements for the displacement of the bright beam showed that the sensitivity improved by a factor of 1.7 in both the x and y direction. Using a similarly made tilt-squeezed beam [32], these measurements were extended so that the tilt of a bright laser beam was measured at a higher sensitivity than the quantum noise limit normally allows.

Normally, to produce amplitude-phase entanglement, we first require either amplitude or phase squeezed beams. Similarly, in order to produce position-momentum entanglement, we first must have position or momentum squeezed beams. As with the standard method of entangling laser beams (shown in Section 3.4), mixing two position squeezed

beams together with a $\pi/2$ phase shift results in laser beams that are position-momentum entangled.

4.3 Squeezing in higher order spatial modes

There are several different techniques that can be used to produce squeezed beams of light, and while that squeezing is generally applied to a TEM_{00} mode, in many cases slight adjustments can be made to the technique to produce squeezed higher order modes.

Multimode squeezing has been produced very successfully using four wave mixing in an atomic vapour [33], and can also be produced using optical parametric amplification. Since optical parametric amplifiers (OPAs) are the squeezers we have chosen to use, these will be dealt with in some detail in this section.

4.3.1 OPA layout

While the theory behind optical parametric amplification has already been outlined in Section 3.3.1, there are considerations to be taken into account in the overall design of the OPA in order to have an optimally functioning squeezer.

Mechanical stability is an important consideration in the design of an OPA, so that a constant output and stable locking systems can be achieved. For this reason all elements should be securely fastened, and there is generally a preference for having fewer elements in the cavity. While there are many possible designs that the OPA can be based upon, there have emerged some layouts that are known to be stable and are commonly seen in quantum optics experiments. The two designs most commonly used are the linear cavity and the bow-tie cavity, which are shown in Figure 4.2. The linear cavity itself has several different designs - it can have two mirrors external to the crystal, or it can have a monolithic or hemilithic configuration, where two or one of the faces of the nonlinear crystal act as partially reflective mirrors to form a cavity. The monolithic configuration is the most mechanically stable layout for an OPA.

Another important consideration to be taken into account for the design of an OPA is how the cavity is to be locked. Typically, two locks are required for one OPA - the seed beam must be locked to the cavity, and the green pump beam must be locked to the phase of the seed beam, in order to control whether the squeezing is on the phase or amplitude quadrature. As covered in Section 2.9.1, locking a cavity requires an actuator to maintain the correct cavity length, compensating for any air currents or drifts in the equipment.

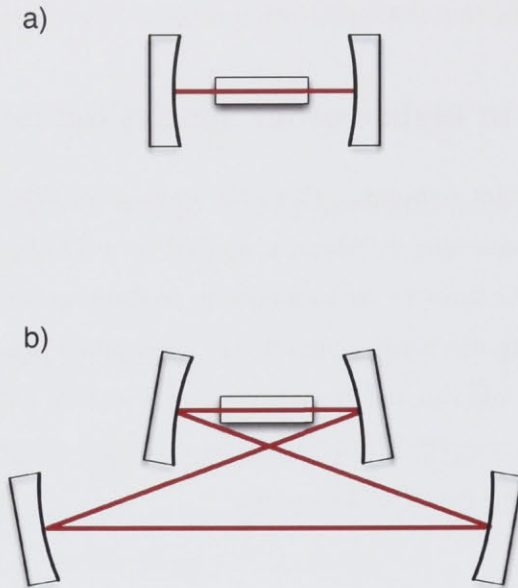


Figure 4.2: Two common cavity configurations for OPAs: a) a linear cavity, and b) a bow-tie cavity.

This is usually achieved in the form of a PZT, which changes its size (and hence position) depending on the voltage applied to it. While it has superior mechanical stability, the monolithic cavity has no PZT to control the length of the cavity as we require to keep the cavity frequency set to the laser frequency, so instead the laser frequency must be locked to the cavity frequency - a setup that can only work for an experiment with no more than one OPA.

One advantage of the bowtie configuration is that two beams can independently be sent in both the clockwise and the anticlockwise directions simultaneously. The squeezed light is only generated in the direction in which the pump beam is travelling, so the pump (and seed, if required) can be sent in one direction, and the locking beam can be sent in the opposite direction, to avoid noise being coupled into the resultant squeezed beam. Alternatively, the seed can still be used to lock the cavity, and the other direction can be used as a second independent OPA, to achieve two independent squeezed beams [11].

4.3.2 Ideal pump mode shape

The pump beam is a vital component in an OPA, providing the intensity needed to induce the nonlinear behaviour in the crystal that allows squeezing to be achieved.

For a seeded OPA that produces a TEM₀₀ squeezed mode, the requirement for optimum nonlinearity is that the pump beam has a waist as determined by the Boyd-Kleinman factor that was introduced in Section 3.3.2. The seed beam is aligned to overlap with this beam, and has a beam waist of $\sqrt{2}w_p$.

Here we have a type I nonlinear interaction, where we transfer photons from the harmonic mode (532nm) to the fundamental mode (1064nm) using the $\chi^{(2)}$ property of the crystal. The quadratic relationship requires that the mode shape of the harmonic mode be the square of the mode shape of the fundamental mode, for optimal interaction. Thus for a TEM₀₀ squeezed mode, we aim to have the waist of the seed beam related to the waist of the pump beam by a factor of $\sqrt{2}$. For higher order squeezed modes, the optimal pump mode shape is more complicated since, for example, the square of a TEM₁₀ mode is no longer a TEM₁₀ mode. The ideal mode to pump with to achieve TEM₁₀ squeezing is actually a combination of TEM₀₀ mode and TEM₂₀ mode [34]. However, the power lost in conversion to different modes and the added degree of complexity that implementing this would entail makes the option of simply using TEM₀₀ mode more practical. The effect of the resultant imperfect overlap is that the threshold power is substantially higher for higher order mode squeezing. Note that even apart from the imperfect pump/seed overlap, the effective nonlinearity for a crystal in an OPA is lower when using higher order modes, since they are spatially less compact.

The Boyd-Kleinman factor, which calculates the ideal waist size for a pump beam in the OPA, does change slightly for different higher order modes. For TEM₁₀ mode, we still have $\xi = \frac{\lambda}{2\pi w_p^2} = 2.84$, but for TEM₂₀ this value changes to 2.45 [35]. Thus the squeezing of spatial modes with $n, m > 1$ may require an adjustment of the cavity mirrors for optimal operation.

4.3.3 Squeezing for different pump powers

The production of a squeezed beam from an OPA relies on there being enough power in the pump beam to induce a nonlinear effect of sufficient magnitude within the crystal. Here we will discuss how the pump power effects the level of squeezing for an OPA.

The relative phase between the seed beam and the pump beam determines whether

the OPA will be operating in the amplification or the de-amplification regime. As the name implies, the power in the seed beam will increase when the OPA is amplifying and it will decrease when the OPA is de-amplifying.

The ratio of the transmitted power in the seed beam when the OPA is amplifying to the transmitted power in the seed beam when there is no pump beam is called the *regenerative gain*. The gain of the OPA changes with the pump power according to:

$$G = 1 + \frac{8(1 - L_{overall})r_{thr}^2}{(\omega^2 + 1 + r_{thr}^2)^2 + 4\omega^2} \quad (4.11)$$

where $L_{overall}$ takes into account both the loss inside the OPA and the external loss, and the parameter r_{thr} is related to the ratio of the power in the pump beam to the threshold power of the OPA: $r_{thr} = \sqrt{\frac{P}{P_{thr}}}$. The cavity has a finite window of frequencies over which it transmits, and the detection frequency must be within this range, as seen in Equation 2.46. ω is the ratio of the detection frequency (with respect to the carrier frequency) to the cavity linewidth.

The squeezing and antisqueezing that is obtained from an OPA was previously found in Equation 3.10, and can be rewritten in terms of OPA parameters that are more easily measured, and as seen in [36].

$$\begin{aligned} V^+ &= 1 - \frac{4(1 - L_{overall})r_{thr}}{\omega^2 + (1 + r_{thr})^2} \\ V^- &= 1 + \frac{4(1 - L_{overall})r_{thr}}{\omega^2 + (1 - r_{thr})^2} \end{aligned} \quad (4.12)$$

where V is the variance for each quadrature. If some of the parameters of the cavity are unknown, they can be found by measuring the quadrature variances and the OPA gain for a range of pump powers, and by adjusting the parameters to fit a curve to this data. $L_{overall}$ includes both loss inside and outside the cavity. These can be distinguished by comparing the measured and predicted finesse for the cavity; this ratio can be used to find the loss that arises inside the cavity, as seen in [36]. This model assumes that there is no extra noise being added to the squeezed beam.

Because the effective nonlinearity is lower when using higher order modes, the ideal setup of the cavity is different. A different gain implies that a different output coupler reflectivity is required to obtain the highest possible amount of squeezing. This is best seen

using the earlier expressions for the output variance of an OPA, shown in Equation 3.10. If we plot the output variance as the output coupling term is varied, we obtain a graph as in Figure 4.3. When the gain of the system changes, the best squeezing is obtained for a different value of the output coupling term, which corresponds to a different output coupler reflectivity.

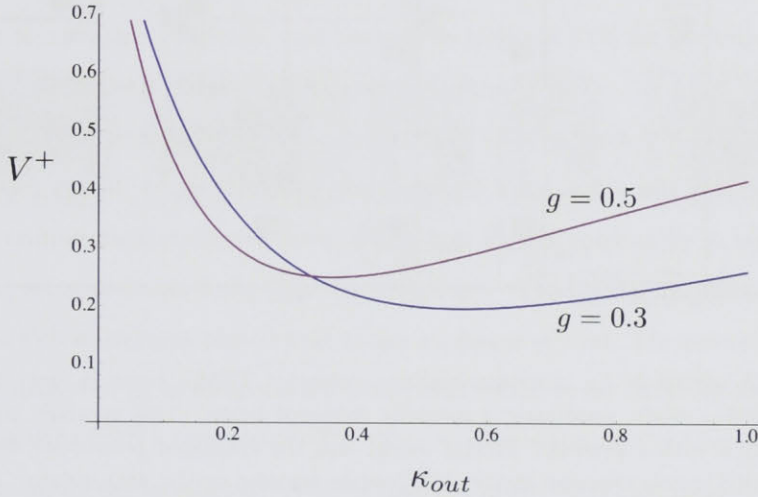


Figure 4.3: The squeezed variance for an OPA with a varying output coupling term κ_{out} with a gain of either 0.5 or 0.3. The parameters used were $\kappa_l = 0.05$, $\kappa_{in} = 0.01$, and $\omega = 0$ for a beam with an original variance of one.

4.4 Experimental setup

The setup for the most important components of the experiment is shown in Figure 4.4. Two squeezed TEM_{10} beams are combined on an entanglement beamsplitter together with a bright TEM_{00} reference beam. The two entangled beams are then measured on homodyne detectors, with local oscillators in the TEM_{10} mode.

4.4.1 The laser

The light source for these quantum optics experiments was a Diabolo continuous wave laser based on a Nd:YAG crystal (Innolight GmbH). Encased in the laser's housing is both the Nd:YAG crystal that makes a 1064nm laser beam, and a frequency doubling unit that uses the process of second harmonic generation to create a second beam at 532nm.

4.4.2 Optical Parametric Amplifiers

For this experiment we use a hemilithic cavity for each of our OPAs; that is, the crystal has one curved surface that acts as a mirror, and one external partially reflecting mirror, that is known as an output coupler. The layout of the OPA can be seen in Figure 4.5 below. The input coupler, positioned on one surface of the crystal, has a radius of curvature of 8mm, and a reflectivity of 99.5% for 1064nm and 100% for 532nm. The output coupler has a radius of curvature of 25mm, and has a reflectivity of 94% for 1064nm and 10% for 532nm. The optical path length of the cavity is 30mm.

The nonlinear crystal itself is made from bulk LiNbO_3 , with 7% MgO doping. The crystal has two curved edges, and has dimensions $2 \times 2.5 \times 6.5 \text{ mm}^3$. The crystal was housed in a temperature stabilized oven, which was heated constantly to temperature of around 60°C using resistors built into the oven base. The crystal temperature was fine tuned using a Peltier element placed next to the nonlinear crystal. The power to the Peltier element was delivered by a temperature controller, which monitored the temperature of the crystal housing with a thermistor. The purpose of fine tuning the temperature was to maximise the nonlinear interaction by achieving the phase matching condition.

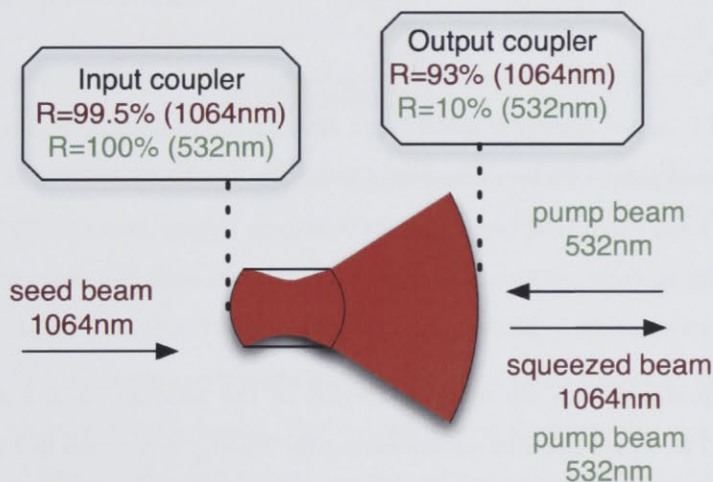


Figure 4.5: The OPAs used in this experiment are based on a hemilithic design, with a LiNbO_3 crystal.

This OPA has been used to produce both TEM_{00} squeezed light and TEM_{10} squeezed

light. The squeezing and antisqueezing for TEM_{00} are shown in Figure 4.6, with 5dB of squeezing and 8dB of antisqueezing at 4.5MHz. This graph also shows several peaks resulting from modulations that have been applied for locking purposes. These peaks result from both the modulations directly, and from beating between different modulations that are applied. A complete list of locking frequencies used is shown in Section 4.4.4.

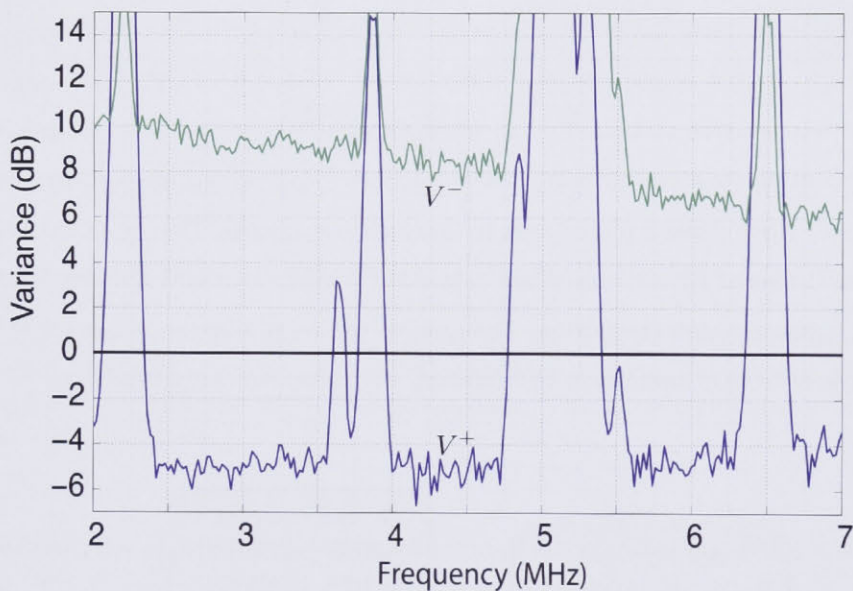


Figure 4.6: The measured degree of squeezing and antisqueezing for the TEM_{00} mode across a range of frequencies.

For this experiment, we are more interested in the production of squeezing in the TEM_{10} mode. The squeezing and antisqueezing for TEM_{10} are shown in Figure 4.7, with nearly 4dB of squeezing and 5dB of antisqueezing for the range of frequencies 3-4.5MHz.

The squeezing and antisqueezing changes with the pump power, as the results in Figure 4.8 show. The curve is based on Equations 4.12, using the measured parameters: detection frequency $f = 4\text{MHz}$, free spectral range $\nu_{FSR} = 3.74\text{GHz}$ and finesse $F_m = 130$. ω is then found from $\omega = f \frac{2f_m}{\nu_{FSR}}$ and the overall loss is obtained from the curve fitting, and is found to be $L_{overall} = 0.23$.

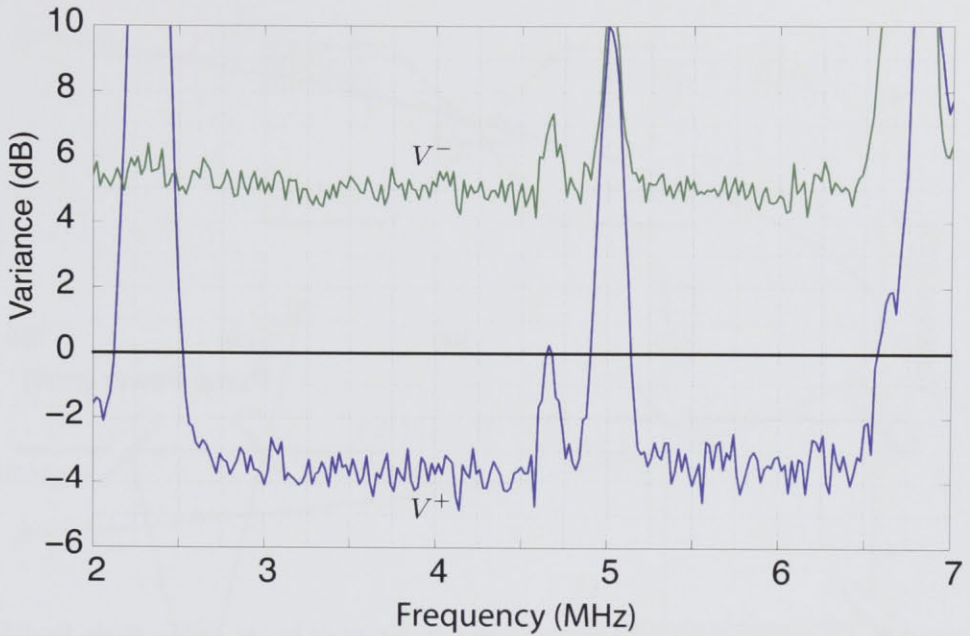


Figure 4.7: The measured degree of squeezing and antisqueezing for the TEM_{10} mode across a range of frequencies.

4.4.3 Mode combination

Once the squeezed TEM_{10} modes are produced, they need to be incorporated into the rest of the experiment by combining them with the TEM_{00} reference beam. There are several methods by which different spatial modes can be combined. The simplest method uses a beamsplitter with different spatial modes at the two input ports, as shown in Figure 4.9a. The two output ports will then each have a combination of the two original spatial modes. What has here been termed a TEM_{00} reference beam could more accurately be described as a coherent TEM_{00} mode copropagating with vacuum noise for all of the other spatial modes in the Hermite Gauss basis. The output states then contain a coherent TEM_{00} mode, and the TEM_{10} mode will have a mixture of the squeezed beam with the vacuum mode that was copropagating with the original TEM_{00} mode. The mixture of the squeezed state with vacuum noise will rapidly diminish the quality of the squeezing in the output beams. The beamsplitter can be non 50:50, in order to place most of the TEM_{10} mode noise on one of the outputs.

It is possible to combine two different modes of light in a near lossless manner, if this is required. There are two main lossless combination methods, and these involve the use

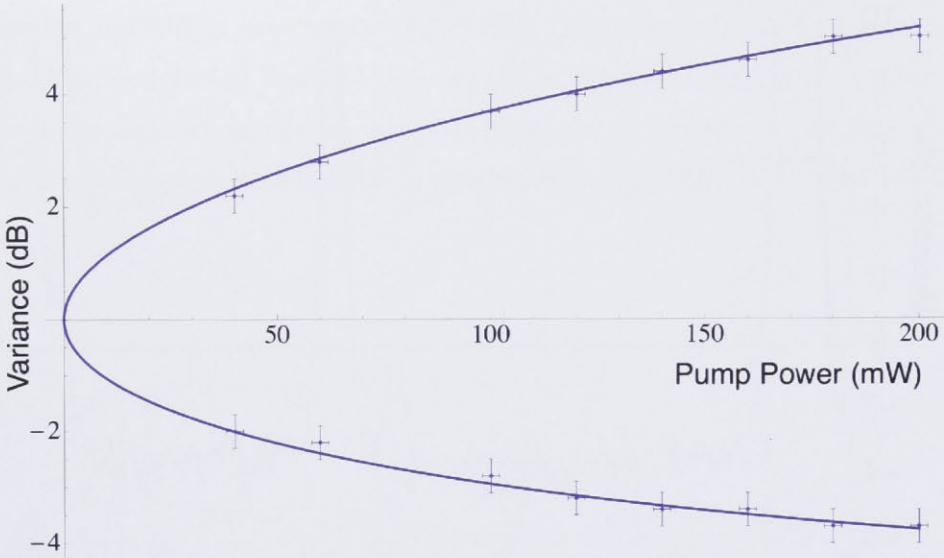


Figure 4.8: The measured degree of squeezing and antisqueezing for the TEM_{10} mode, for different pump powers. The continuous line shows the fit to the theoretical curve.

of either a cavity or an adapted Mach Zehnder interferometer. When a mode cleaning cavity, or MCC, is used the cavity is locked onto one mode, say TEM_{00} mode, so that it transmits this mode, but reflects all other modes in the Hermite Gauss basis. The TEM_{10} mode is then sent onto the output mirror of the cavity, such that its reflection ends up co-propagating with the original beam, as seen in Figure 4.9b.

A third option that is available for some kinds of mode combination is an adapted Mach Zehnder (MZ) interferometer, as shown in Figure 4.9c. In contrast to a standard Mach Zehnder setup, there is an extra mirror on one of the arms before the two beams are interfered. In this case we are interested in having one even mode input and one odd mode input, and we can describe these modes as:

$$\begin{aligned}
 E_{in,e}(x) &= A_e u_e(x) \\
 E_{in,o}(x) &= A_o u_o(x) e^{i\phi_{rel}}
 \end{aligned}
 \tag{4.13}$$

where u_e and u_o indicate that the even and odd mode profiles respectively, $A_{e,o}$ correspond to the field amplitudes, and ϕ_{rel} is the relative phase difference between the two input fields.

If the two arms of the interferometer are recombined with a phase shift Φ , then the

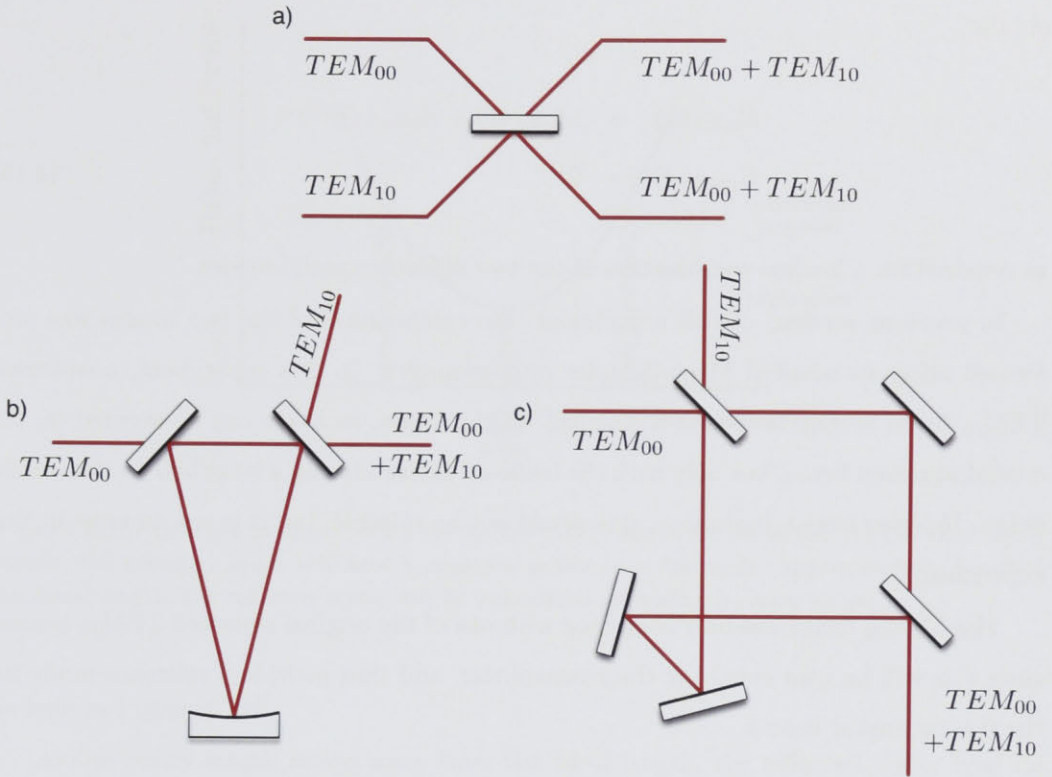


Figure 4.9: There are various methods of combining different modes in an experiment. a) A beamsplitter can be used to combine two modes, but couples loss into the output beams. b) A cavity on resonance for one mode and off resonance for a second mode can be used. c) An adapted Mach-Zehnder interferometer, used as a mode combiner, or mode separator. This method is only useful if one mode is symmetric, and the other mode is anti-symmetric.

newly formed output fields are given by:

$$\begin{aligned}
 E_{out,1}(x) &= \frac{1}{2} \left[iA_e u_e(x) (1 + e^{i\Phi}) - A_o u_o(x) e^{i\phi_{rel}} (1 + e^{i\phi}) \right] \\
 E_{out,2}(x) &= \frac{1}{2} \left[A_e u_e(x) (1 - e^{i\Phi}) + A_o u_o(x) e^{i\phi_{rel}} (1 - e^{i\phi}) \right]. \quad (4.14)
 \end{aligned}$$

The difference between these output fields and those that would be obtained with a symmetric Mach Zehnder interferometer is due to the additional phase shift that is experienced by the odd mode on the arm with the additional reflection. This additional phase shift occurs due to the effects of reflection on the the mode profile of an odd mode as opposed to an even mode; the odd mode undergoes the transformation $u_o(-x) \rightarrow -u_o(x)$ whereas the even mode undergoes no such transformation and $u_e(-x) \rightarrow u_e(x)$.

We can then take the case where the phase difference upon recombination is zero to obtain:

$$\begin{aligned} E_{out,1}(x) &= iA_e u_e(x) - A_o u_o(x) e^{i\phi_{rel}} \\ E_{out,2}(x) &= 0 \end{aligned} \tag{4.15}$$

as required for a lossless combination of the two different spatial modes.

In previous versions of this experiment, the combination of the two modes was performed using an adapted Mach-Zehnder interferometer. In this experiment, a squeezed TEM₁₀ beam is combined with a classical TEM₀₀ beam, so losses can be avoided on the crucial squeezed beam, but only with the trade-off of introducing a large loss on the second beam. If power were a limitation, this would not be suitable, but it is not an issue in this experiment.

The TEM₀₀ beam was only combined with one of the original squeezed TEM₁₀ beams, since this will be split evenly at the beamsplitter, and thus provide a reference mode for the two entangled beams.

4.4.4 Locking Scheme

There were several locking loops required to perform the experiment, for locking the OPAs, the mode cleaning and transfer cavities, and for locking to the phase of the two beams on the beamsplitter, and for locking to the correct phase of the local oscillator.

PDH locking is used, as well as two other forms of locking that will be discussed here: dither locking, DC locking and split detector locking.

Dither locking

Dither locking is a form of modulation locking that can be applied to cavities. Unlike PDH locking, where the beam is phase modulated prior to reaching the cavity, for dither locking the modulation is applied to the length of the cavity directly, thus modulating the resonant frequency of the cavity.

We consider a setup where the beam reflected from the cavity is detected and used to produce the error signal. When the cavity has a length for which the beam is resonant, the reflected power is at a minimum, and at a stationary point. At this position, a small modulation in the cavity length will not result in a large modulation to the reflected power,

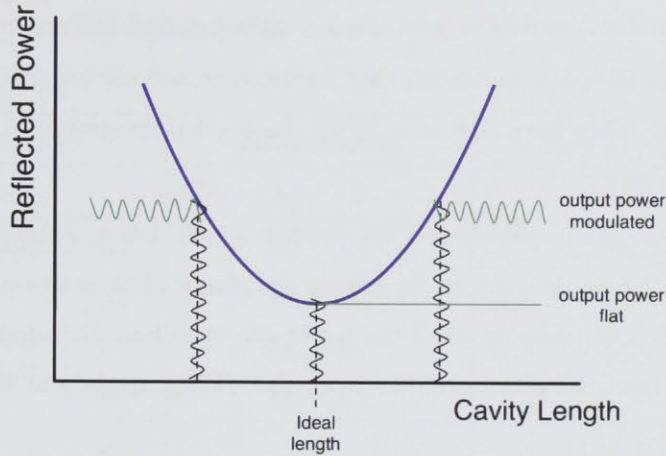


Figure 4.10: In order to dither lock a cavity, the cavity length is modulated. At the ideal cavity length, the reflected beam will have a constant power to a first order approximation, but at a non-ideal length, the reflected power will be modulated, providing an error signal.

as seen in Figure 4.10³.

As the cavity length moves away from this ideal length, the reflected power level increases, and the modulation that is applied to the length of the cavity causes a modulation in the output power that depends on the gradient of the curve in Figure 4.10. The oscillating power on the reflected field can then be used as an error signal, since its sign depends on which direction the length needs to change, and its amplitude depends on how far the cavity is from the correct length.

For dither locked cavities, the modulation is applied using a PZT rather than an EOM, making the setup somewhat simpler. The use of a PZT for the modulation means that the frequencies that can be used must be hundreds of kilohertz or lower, unlike PDH locking, where the modulation frequencies used are often of the order of megahertz.

In this experiment, dither locking is used for locking low finesse cavities, such as interferometric systems where we lock the phase of two beams.

Split detector locking

Split detector locking is a well established method [37, 38, 39] that can be applied in order to lock the phases of two different spatial modes, in particular the TEM_{00} mode and the

³If Ω_M is the modulation frequency, there is a small modulation in the reflected beam that occurs at $2\Omega_M$, to a second order approximation.

TEM₁₀ mode.

Different spatial modes within one basis are orthogonal, so the overlap integral is zero when taken across all space, indicating that interference will not occur in this case. If the overlap integral is taken from 0 to ∞ , then the overlap integral is no longer zero, and interference can occur.

Experimentally, the implication of this is that a split detector rather than a normal photodetector is the required device for locking the phases of these two orthogonal beams. The left and right DC components of the power can then be subtracted to give an error signal that will keep the phase shift between the TEM₀₀ mode and the TEM₁₀ mode constant.

The error signal obtained from the subtraction of the two halves of the split detector locks the phase between the two spatial modes to $\phi_{rel} = \pi/2$ at the split detector plane. Furthermore, the beam containing the two modes is focussed before reaching the split-detector, introducing a Gouy phase shift, so the phase difference in the split detector plane is not the same as the phase difference for the collimated beams.

A position squeezed beam has a relative phase difference between the two modes of $\phi_{rel} = 0$ if the TEM₁₀ mode has amplitude squeezing, so we cannot accurately claim that we have made a position squeezed beam. However, position squeezed beams are not strictly necessary for the measurement of position-momentum entanglement between two laser beams. For instance, we could also use two momentum-squeezed beams locked in quadrature at the entanglement beamsplitter.

As long as the relative phase shift between the two spatial modes is constant, and the two TEM₁₀ components of the beams are mixed with a $\pi/2$ phase shift, we can obtain spatial entanglement.

Locking systems

There are many locking loops in the spatial entanglement experiment, for the many cavities that must maintain a precisely set length and for setting the phase between beams that are being mixed. For the Pound-Drever-Hall (PDH) locking loops, there are three different applied modulation frequencies: a 12MHz phase modulation is applied to the beams inside the laser; and the external electro-optic modulator (EOM) is used to impart a 14.3MHz and a 21.3MHz phase modulation on the infrared beam. The locks to the amplitude quadrature at the homodyne detectors used lower frequency modulations, in

the kHz range. These were applied with a signal sent to the PZT that modulated the phase of the beams directly. The details of each of the locking loops are shown in the table below.

Locking loop		Error signal	Locking Frequency
Entanglement		$(D_1 + D_2) - (D_3 + D_4)$	DC
Local oscillator	X_x^+	$D_1 - D_2$	359kHz
	X_x^-	$D_1 - D_2$	DC
	X_y^+	$D_3 - D_4$	368kHz
	X_y^-	$D_3 - D_4$	DC
OPA ₁	seed	D_5	14.3MHz
	pump	D_5	21.3MHz
OPA ₂	seed	D_6	14.3MHz
	pump	D_6	21.3MHz
MCC ₁		D_7	12MHz
MCC ₂		D_8	14.3MHz
MTC		D_9	14.3MHz
Reference Beam		$SD_{left} - SD_{right}$	DC

Here SD means split detector.

The locks for the homodyne detection system is shown in Figure 4.11.

A DC lock is performed by taking a subtraction of the DC powers for two or more photodetectors. This type of locking system is particularly sensitive to asymmetries in the experiment. If there is an extra loss present in one of the entangled beams, then $(D_1 + D_2) - (D_3 + D_4)$ no longer gives an error signal that locks to the required $\pi/2$ phase shift. This can be compensated for by introducing a DC offset to the error signal in the control electronics.

In this experiment we use pre-loaded PZT systems in the cavities, where the curved mirror that is used to adjust the length of the cavity is controlled by a ring PZT actuator that pushes against the front of the mirror. The back of the mirror is then pushed against a rubber o-ring. This pre-loaded setup effectively increases the mechanical resonance frequency of the PZT, which increases the locking bandwidth of the cavity, leading to a more stable lock.

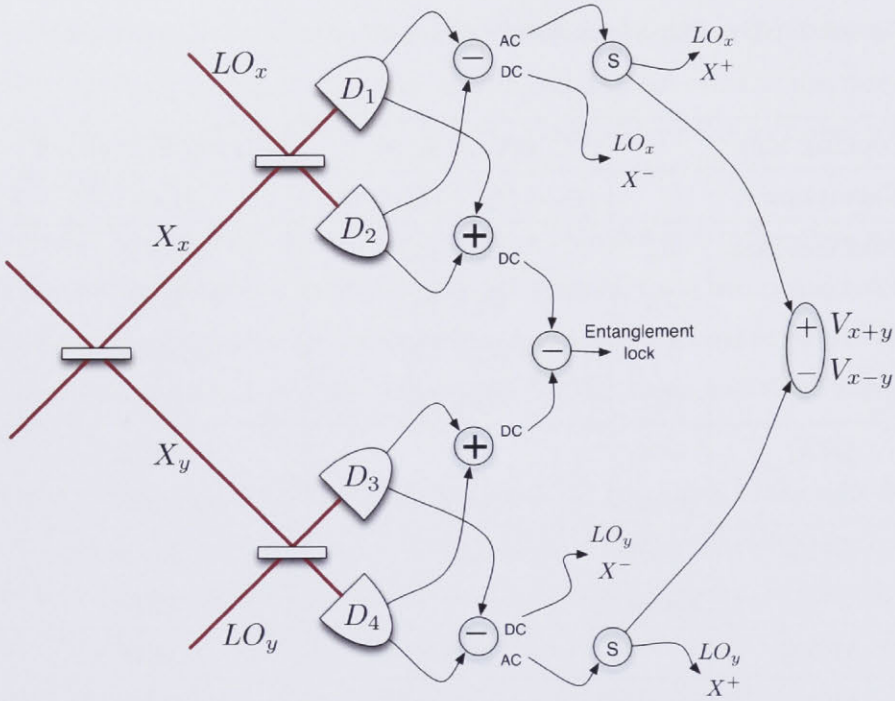


Figure 4.11: The homodyne detectors, showing the use of the different signals. Here S signifies the use of an electronic splitter.

4.4.5 Measurement method

Like many other quantum states of light, entanglement can be observed using a spectrum analyser. A spectrum analyser measures the power spectrum $S(\omega)$ of the fluctuations of the field at frequencies around the optical carrier frequency. There are two ways a spectrum analyser can be used to measure EPR entanglement, based on the following expressions [4]:

$$V_{x|y} = \min_g \langle (\delta X_x - g \delta X_y)^2 \rangle \tag{4.16}$$

$$= V_x - \frac{|\langle \delta X_x \delta X_y \rangle|^2}{V_y} \tag{4.17}$$

Using the first expression, the entanglement can be found directly, by subtracting the two AC signals from the homodyne detector with an appropriate gain applied to one arm. However, there is an alternative that can be found based on the second expression that doesn't require the fine adjustment of g . We know that:

$$V_{x+y} = \frac{V_x + V_y + 2\langle\delta X_x \delta X_y\rangle}{2} \quad (4.18)$$

$$\implies \langle\delta X_x \delta X_y\rangle = V_{x+y} - \frac{V_x + V_y}{2}. \quad (4.19)$$

We can then substitute this expression for both quadratures into our definition for ϵ .

$$\epsilon = V_{x|y}^+ V_{x|y}^- \quad (4.20)$$

$$= \left(V_x^+ - \frac{|\langle\delta X_x^+ \delta X_y^+\rangle|^2}{V_y^+} \right) \left(V_x^- - \frac{|\langle\delta X_x^- \delta X_y^-\rangle|^2}{V_y^-} \right). \quad (4.21)$$

Thus we can find our value for ϵ from measurements of the variances of each beam for X^+ and X^- , combined with variances V_{x+y}^+ and V_{x-y}^- .

This is the method used in the experiment here, since it does not require fine-tuning for g and separate measurements for the Inseparability and for EPR, which would otherwise be required in an asymmetric experiment such as we have.

Some experiments have two possible values that can be obtained for the EPR entanglement: $\epsilon_{x|y}$, where the fluctuations in x are predicted from the measured fluctuations of y , and $\epsilon_{y|x}$, where the fluctuations in y are predicted from the measured fluctuations of x . The two values can be calculated using the same method.

4.5 Experimental results

Using the method outlined in Section 4.4.5, the EPR entanglement was observed. The same data allowed another entanglement criterion, the Inseparability of the system, to be observed.

The local oscillator beams used at the homodyne detectors were set to 3mW in the TEM₁₀ mode. This value is high enough to be at least 10 times more powerful than the carrier beams, but is not so high as to saturate the detector photodiodes. The detectors were built at ANU, using ETX500 photodiodes with quantum efficiency of 95±3%.

The spectrum analyser⁴ curves that are required to calculate EPR entanglement are shown for the position and momentum of the beams in Figures 4.12 and 4.14. The lowest

⁴The relevant spectrum analyser settings were as follows: VBW=100Hz, RBW=100kHz, Det: sample, Scale: 2dB/div. The scale is an important parameter on some spectrum analysers, since in some cases (as here) the measurements are inconsistent across some scales. Measurements were performed to investigate this, and it was found that with our spectrum analyser any scale greater than 1dB/div was accurate.

curves on each of these figures show V_{x+y}^+ and V_{x-y}^- , and can be used to calculate the Inseparability directly, or the three curves on each graph can be used to calculate the conditional variance for that observable. All curves are shown relative to the coherent state quantum noise limited case. The conditional variances are shown in Figures 4.13 and 4.15. Both the traces show these to be substantially lower than one over a broad frequency range.

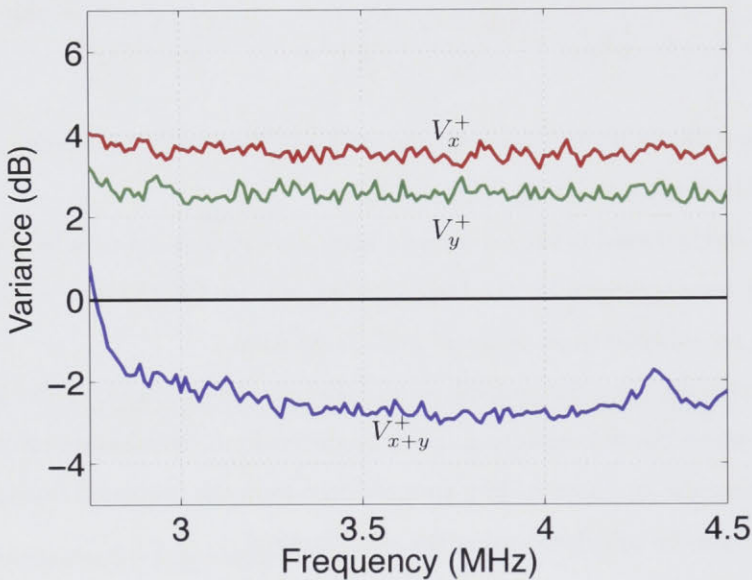


Figure 4.12: The three curves required to calculate the conditional variance for the amplitude quadrature (direction) of our laser beam, normalised to the corresponding coherent state variance.

The two traces shown for the conditional variances then allow us to find the value for EPR entanglement.

For a perfectly symmetric system, one would expect for the different measured variances after the entanglement beamsplitter to be identical, ie. $V_x^+ = V_y^+ = V_x^- = V_y^-$. It is apparent from the traces of V_x and V_y that this is not the case in this experiment, and the symmetry has been broken at some point.

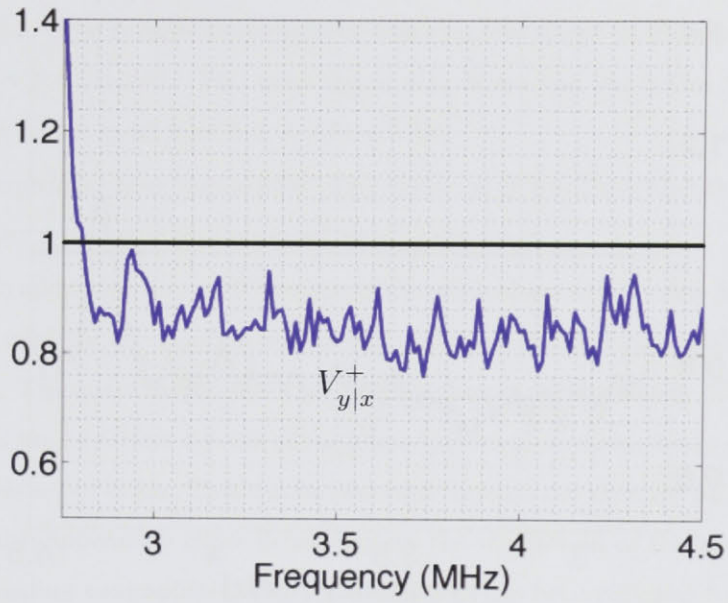


Figure 4.13: The conditional variance for the amplitude quadrature (direction) of our laser beam.

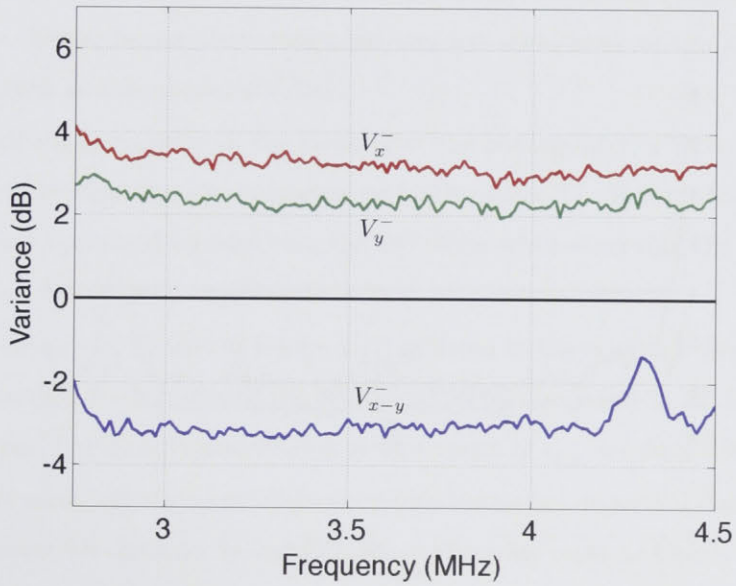


Figure 4.14: The three curves required to calculate the conditional variance for the phase quadrature (tilt) of our laser beam.

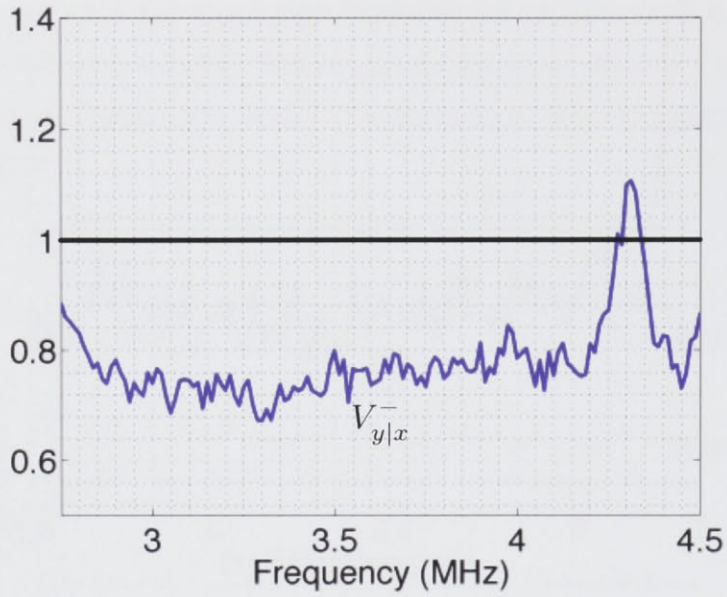


Figure 4.15: The conditional variance for the phase quadrature (tilt) of our laser beam.

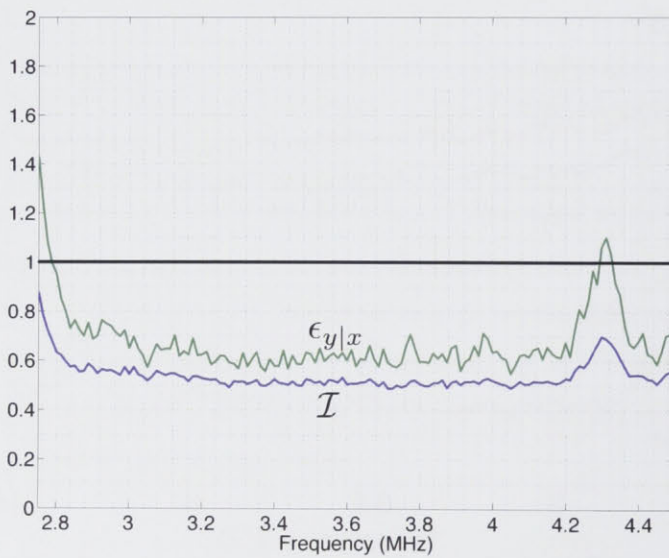


Figure 4.16: The results for Inseparability and EPR entanglement.

In asymmetric systems⁵ there are two possible values for EPR entanglement, since the conditional variance depends on the direction in which the inference is made, as discussed in Section 3.4.2. The reverse reconciliation case ($\epsilon_{y|x}$) is shown in Figure 4.16, and has a value of $\epsilon = 0.62 \pm 0.03$. The same figure also shows the results for the amount of Inseparability, which at its best is $\mathcal{I} = 0.51 \pm 0.02$.

Since the squeezers have very similar characteristics, it is unlikely that this is the source of the asymmetry, and that this occurred later in the setup.

There is an additional loss of 10% on one of the original squeezed beams due to the 90:10 beamsplitter used for the combination of the squeezed TEM₁₀ beam with the coherent TEM₀₀ beam. The quantum efficiency for the detectors is approximately 95%, and on top of this there is the imperfect overlap of the homodyne local oscillator beam with the mode profile of the detected beam. This can be observed through the visibility at the homodyne detectors, which appears to differ depending on the interaction of the beam of interest with the entangling beamsplitter. For the beam that has been reflected from the coated side of the beamsplitter, the visibility is approximately 96% when observing TEM₁₀ mode. If the beam has been transmitted through the beamsplitter, the visibility deteriorates to approximately 90%, and for a beam that travels through the glass, is reflected, and travels through the glass again, the visibility is 85%. This additional loss is suspected to arise due to phase distortion imparted onto the beam by the entangling beamsplitter. It may be that for a thinner beamsplitter this issue does not arise, however this could introduce other issues such as a decreased stability.

Because of the asymmetry in the losses after the beamsplitter, a DC offset was introduced in the error signal for the entanglement locking loop. The lock for the entanglement phase shift was optimised by adjusting the DC offset while observing the traces of V_{x+y}^+ or V_{x-y}^- , which we sought to minimise.

The two values can be seen in Figure 4.17, as fitted to the expected theoretical curves. Both the direct reconciliation and the reverse reconciliation result in an EPR trace that goes below one. The direct reconciliation gives a result of $\epsilon_{x|y} = 0.94 \pm 0.03$.

Finally we must test the mode of the entangled beams before we can claim to have spatial entanglement for our laser beams. The beam intensity must be mainly in the TEM₀₀ mode, since this is the mode for which we are measuring the position and momentum. Our entangled beam is mainly comprised of TEM₀₀ mode, with over 90% of the intensity

⁵For more details on how these two values arise, see Chapter 6 on Asymmetric Entanglement.

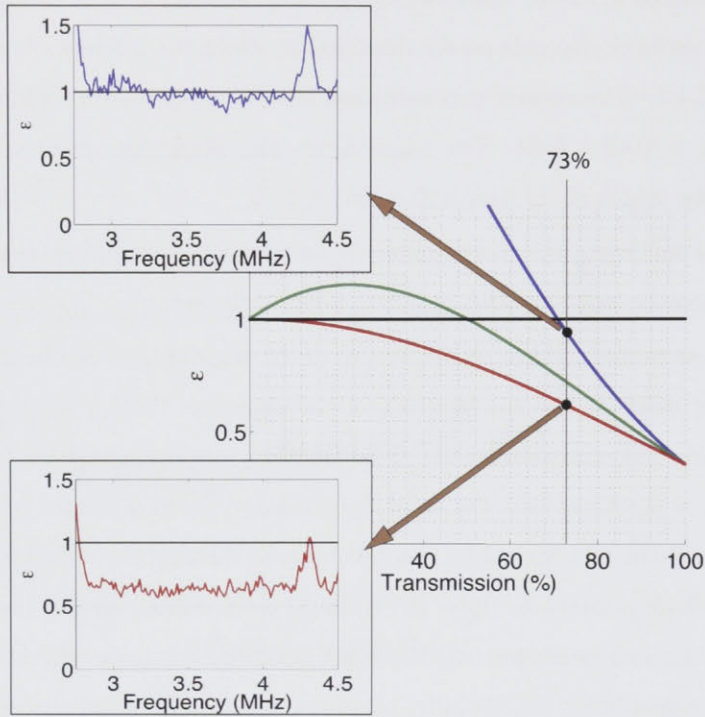


Figure 4.17: The two results for the value of ϵ . The lower curve shows the case for ‘direct reconciliation’, the upper curve shows the case for ‘reverse reconciliation’, and the middle curve is what a symmetric system with the same overall losses would expect to find.

being in the TEM_{00} mode.

Over the same time frame, Boyer and others have been using four wave mixing to achieve spatial quantum behaviour. The group initially produced squeezing of 6.5 dB using four wave mixing in a hot ^{85}Rb vapour and used this to measure spatial quantum correlations between Laguerre-Gauss modes [33]. The same method was later used to create entanglement between T shaped images, and an inseparability of 0.37 ± 0.02 (when normalised to one) and an EPR value of 0.55 was measured [40]. The group also produced two beams that were entangled for many different spatial mode local oscillators.

4.6 Conclusion

We have demonstrated spatial entanglement, or entanglement between the position and momentum observables, between two laser beams. OPAs were used to produce two TEM_{10} squeezed beams, one of which was mixed with a bright TEM_{00} beam. The two beams were then mixed on a beamsplitter with a phase shift of $\pi/2$ to produce position momentum

entangled beams.

The entanglement was characterised using two entanglement criteria: the EPR criterion and the Inseparability criterion. Entanglement was observed over a broad range of frequencies, with the best Inseparability result being $\mathcal{I} = 0.51 \pm 0.02$. Asymmetry in the experiment led to two different values for the EPR entanglement, depending on the direction of inference that was used. The two values were found to be $\epsilon_{y|x} = 0.62 \pm 0.03$ and $\epsilon_{x|y} = 0.94 \pm 0.03$.

Multimode Entanglement

5.1 Introduction

Although entanglement has been demonstrated for many different optical systems with two beams of light [36], there has been a trend towards extending entanglement into multimode systems that potentially allow more complex processes to be handled [41, 42, 43]. Tripartite GHZ correlations and, more recently, cluster states combining four individual squeezed modes, have been demonstrated with impressive reliability [12, 44]. However, using separate beams to build the quantum state requires the combination of complex resources, in particular several squeezers, and many beam splitters, phase shifters and a set of separate homodyne detectors. This technology is difficult to simplify as it is very sensitive to losses and any mode-mismatch.

An alternative approach is to consider multiple orthogonal modes within a single beam. There have been proposals to use correlated modes with different frequencies generated in one source [45], to correlate several frequency sidebands [46] or to use temporal modes that describe different pulse shapes [47]. Spatial modes, on the basis of Hermite-Gaussian (H-G) modes TEM_{nm} , can be generated efficiently, superposed with low losses [48] and many modes can be measured simultaneously using a single multi pixel homodyne detector [49, 50]. It has also been shown that these spatial structures can also be noiselessly amplified, even though the noise factor for amplification when working in the high gain, coherent state input regime is quantum noise limited to 3dB. Choi et. al. [51] bypassed this using optical parametric amplification to achieve a gain of 2.5 on a two slit image with a noise factor of 0.2 ± 0.6 dB. Later Lopez et. al [52], extended this noiseless amplification to a range of images and for a range of gains using a confocal OPO. Such amplification would be very useful for any potential quantum communication scheme using the spatial characteristics of beams. Shaping the local oscillator using a spatial light modulator and varying the gains on the pixels of the detector changes the measurement basis. This creates

a family of orthogonal measurements. As an in-principle demonstration we perform the entanglement of two spatial modes, TEM_{01} and TEM_{10} , within one beam.

The steps required to generate entanglement between two modes in one beam are the same as those required for a more traditional entanglement setup. We require two squeezed modes - in this case we need a squeezed TEM_{01} mode and TEM_{10} mode in one beam. We require a $\pi/2$ phase difference between the two modes before they are mixed with a 50:50 ratio. We must then detect the correlations between the two modes for two quadratures separated by $\pi/2$.

This work has been published in *Nature Photonics* 3, 399 (2009).

5.2 Producing the squeezed beam

Methods of creating squeezed higher order spatial modes have already been discussed in Section 4.3. Essentially, the OPA (optical parametric amplifier) can be seeded with the required spatial mode, and locked at a length that allows that mode to constructively interfere and pass through the cavity. The required cavity length generally changes slightly for different spatial modes, due to the Gouy phase shift, described in Section 2.8.2. For the TEM_{10} and the TEM_{01} modes, this phase shift is identical, implying that when a linear cavity is locked for one of these modes, it is automatically locked for the other. If the cavity is an OPA, then the degeneracy that occurs due to the rotational symmetry means that two squeezed spatial modes can be obtained using one squeezer.

Squeezed light in two orthogonal spatial modes is produced using a degenerate OPA operating below threshold, as seen in Figure 5.1. The OPA contains a magnesium oxide doped lithium niobate crystal as the nonlinear material. The technical details of the OPA, such as the dimensions and the reflectivity of the surfaces are discussed in Section 4.4.2.

The OPA is seeded with a weak TEM_{01} field incident on the high-reflecting side of the OPA crystal. The alignment of the OPA is more crucial in this experiment, in order to achieve the degeneracy required - the cavity frequency for the two different spatial modes must be very close to equal. The degeneracy between the two modes is optimized by changing the temperature of the laser crystal. For a squeezer to operate in the TEM_{10} mode, the ideal pump mode shape is a combination of TEM_{00} and TEM_{20} mode [34]. To produce both a squeezed TEM_{10} mode and a squeezed TEM_{01} mode, the ideal pump mode shape is more complicated again, with components in the TEM_{00} , TEM_{20} , and TEM_{02} modes. The OPA is here operated as a de-amplifier with a gain of 0.4 using

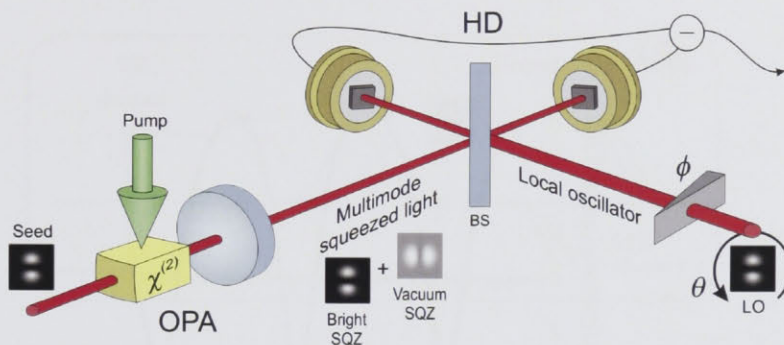


Figure 5.1: Schematic layout of the squeezing experimental setup. The squeezed beam is measured with a homodyne detector, and the TEM_{01} local oscillator (LO) is rotated to measure squeezing in different spatial modes. OPA: optical parametric amplifier; BS: 50:50 beamsplitter. Picture from [53].

180 mW of pump power in the TEM_{00} mode, which while not the ideal mode shape, nonetheless provides sufficient nonlinear gain. As a result, multimode squeezed light with a low intensity amplitude squeezed field in TEM_{01} mode and vacuum squeezed field in TEM_{10} mode, is produced. We then measured the field from the OPA using a standard homodyne detection setup. The local oscillator (LO) mode shape determines which spatial mode we will measure, and we originally set this to the TEM_{01} mode. In order to measure the squeezing in TEM_{10} mode, we then rotated the LO by 90° . The rotation is achieved using a Dove prism - an optical device that uses total internal reflection to rotate a beam. By rotating a Dove prism by an angle γ , the beam is rotated by an angle 2γ . For TEM_{01} operation we typically observed 4 dB of squeezing and 6.5 dB of anti-squeezing, as seen in Figure 5.2a. When the LO TEM_{01} mode is rotated with respect to the x -axis, we observed states of approximately the same squeezing and antisqueezing, as shown in Figure 5.2b. This demonstrates multi-mode squeezing generation using a single linear degenerate OPA.

Note that since the measurements of the different spatial modes were not simultaneous with this setup, we cannot say anything about the relative phase of the two modes, or measure correlations between the different spatial modes.

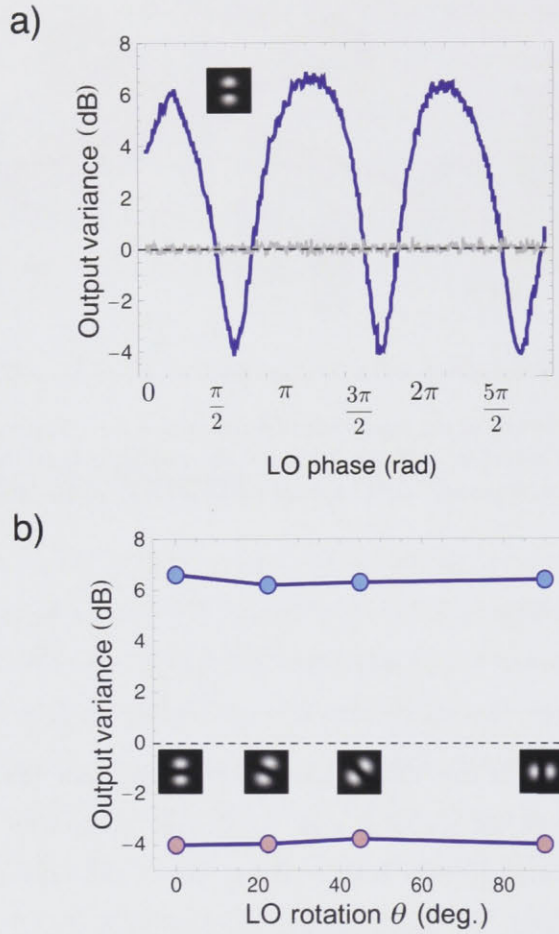


Figure 5.2: a) Measurement of squeezed field in TEM_{01} mode and scanning the phase of LO. b) Measurements of squeezing/antisqueezing when the TEM_{01} LO beam is spatially rotated by θ along the x -axis using a Dove prism.

5.3 Simultaneous mode detection

5.3.1 Quadrant Detector

In order to measure the correlations between the modes simultaneously, we replaced the standard homodyne detection system with a quadrant detector. The LO beam used with the quadrant detector was in the TEM_{00} mode. By combining the electronic signals from the quadrant detector with different gains, we can effectively choose which mode we will measure.

The detector eigenmode is given by the product of the LO profile and the gain function

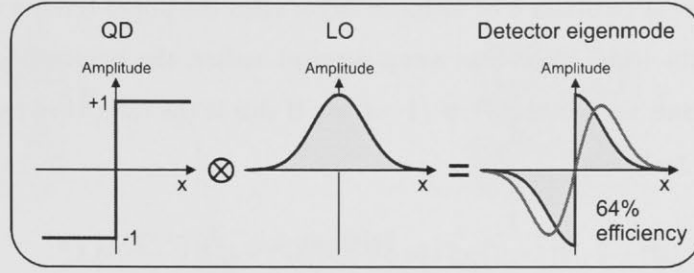


Figure 5.3: Principle of split-detection technique. The eigenmode of a split-detector is a flipped mode, resulting in 64% detection efficiency in TEM_{10} basis.

for the detector. This principle is shown for a split detector operated with a TEM_{00} LO in Figure 5.3. The overlap integral with the TEM_{10} mode then gives 64% as the upper limit for the detection efficiency. A quadrant detector can be operated as two split detectors by combining the quadrants with appropriate gains.

Rather than using two quadrant detectors in the homodyne detector, here we use a more simplified system, with 90:10 beamsplitter ratio and a single quadrant detector.

Recall from Section 2.5 that one of the outputs c for a beamsplitter with two inputs a and b , mixed with a phase difference ϕ , with a beamsplitter ratio of t can be written as:

$$c = e^{i\theta_c}(\sqrt{1-t}a + e^{i\phi}\sqrt{t}b). \quad (5.1)$$

If we linearise this, it then becomes:

$$c = e^{i\theta_c}(\sqrt{1-t}(\alpha + \delta a) + e^{i\phi}\sqrt{t}(\beta + \delta b)). \quad (5.2)$$

The intensity of this output is then:

$$\begin{aligned} c^\dagger c &= e^{i\phi}\sqrt{t(1-t)}(\alpha^*\beta + \alpha^*\delta b + \beta\delta a^\dagger) + e^{-i\phi}\sqrt{t(1-t)}(\beta^*\alpha + \beta^*\delta a + \alpha\delta b^\dagger) \\ &+ (1-t)(\alpha^*\alpha + \alpha^*\delta a + \alpha\delta a^\dagger) + t(\beta^*\beta + \beta^*\delta b + \beta\delta b^\dagger). \end{aligned} \quad (5.3)$$

If we set α and β to be real, we then find:

$$\begin{aligned} c^\dagger c &= \sqrt{t(1-t)}[\alpha\beta(e^{i\phi} + e^{-i\phi}) + \alpha(\delta b e^{i\phi} + \delta b^\dagger e^{-i\phi}) + \beta(\delta a e^{-i\phi} + \delta a^\dagger e^{i\phi})] \\ &+ (1-t)(\alpha^2 + \alpha\delta X_a^+) + t(\beta^2 + \beta\delta X_b^+). \end{aligned} \quad (5.4)$$

If we assume that our detector is on the beam c , then on this beam we need for the power coming from the local oscillator b to be much larger than the power coming from the field of interest a . In the usual homodyne setup detailed earlier, the requirement was simply that $\beta \gg \alpha$, but here we require $t\beta^2 \gg (1-t)\alpha^2$. If this is the case, then we can find the end measurement to be:

$$c^\dagger c = \underbrace{t\beta^2 + 2\sqrt{t(1-t)}\alpha\beta \cos \phi}_{DC} + \underbrace{t\beta\delta X_b^+ + \sqrt{t(1-t)}\beta\delta X_a^\phi}_{AC}. \quad (5.5)$$

If we look at the AC term for the detector, there are two parts: one depending on the noise on the beam we're interested in (δX_a^ϕ) and one with noise from the local oscillator beam (δX_b^+).

The disadvantage of this method is that there is always noise detected from the local oscillator beam. This noise can be decreased by lowering the beamsplitter transmission, t . If this value is lowered too much, then the local oscillator at the detector will not be intense enough for the assumptions made in the derivation. Here we use a 90:10 beamsplitter, giving us an extra loss of 10% on the detected beam.

5.3.2 Digital data acquisition

In most standard continuous variable entanglement experiments, there are two separate homodyne detectors, resulting in two quickly varying signals, δX_x and δX_y , as shown in Figure 5.4a. In order to measure the Inseparability of the system, these signals are normally subtracted using an electronic splitter, and the signal is then sent to the spectrum analyser, which records the variance directly.

If a digital data acquisition system is used, then the quickly varying signals δX_x and δX_y are recorded directly at a high speed - in our case they are sampled at 10MHz - and the pairs of data points can then later be subtracted, and the variance of the resulting signal can then be obtained.

The difference between the two different methods of making measurements can be understood by considering the ellipse diagrams that were introduced in Section 3.4. The ellipses are obtained by taking the quickly changing δX_x and δX_y measurements for the phase or amplitude quadrature, and plotting these parametrically. The first standard deviation for the points results in an elliptical shape, which can be compared to the quantum noise limit, which forms a circular shape. An example of one of these ellipses is

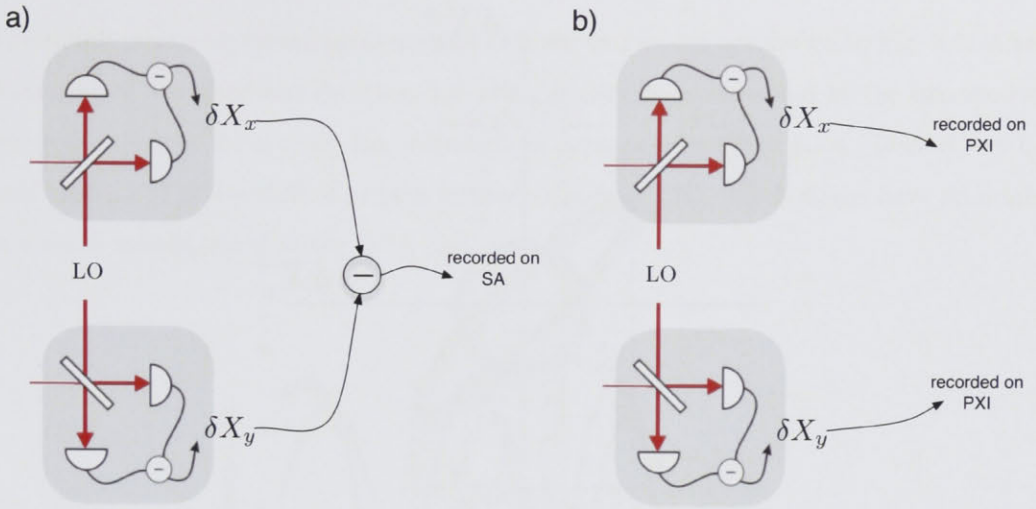


Figure 5.4: Different methods of taking the data for an entanglement experiment: **a)** the required signal can be obtained using electronic devices, and the variance for the signal measured on a spectrum analyser, or **b)** the noise of the system can be recorded directly using a digital data acquisition system.

shown in Figure 5.5, with some of the values that can be found from the ellipse labelled.

Essentially, the analogue subtraction of the two signals followed by measurement with a spectrum analyser gives us the value for σ_{x-y}^+ , whereas the digital data acquisition gives us the series of data points that allows us to draw the ellipse. As shown in Figure 5.5, this provides more versatility in the measurements that can be made.

For a spectrum analyser, different sideband frequencies are measured by mixing the original signal with a local oscillator that couples the signal into a frequency at which an appropriate filter can be used. The filter that is used around the chosen frequency sets the resolution bandwidth, or RBW, for the measurement. Using digital data acquisition, the data is usually broken up into different sideband frequency components and analysed in detail after the measurement has taken place¹.

In our experiment, we don't have two separate homodyne detectors, but rather we use a single quadrant detector with different gain functions for the photodiodes to arrive at the required signals: δX_x and δX_y . These two signals are fed into a National Instruments PXI system, and recorded simultaneously for one second with a sample rate of 10MHz.

There are several methods of analysing the data, and here the method used for this

¹Each frequency component can then be thought of as having its own ellipse.

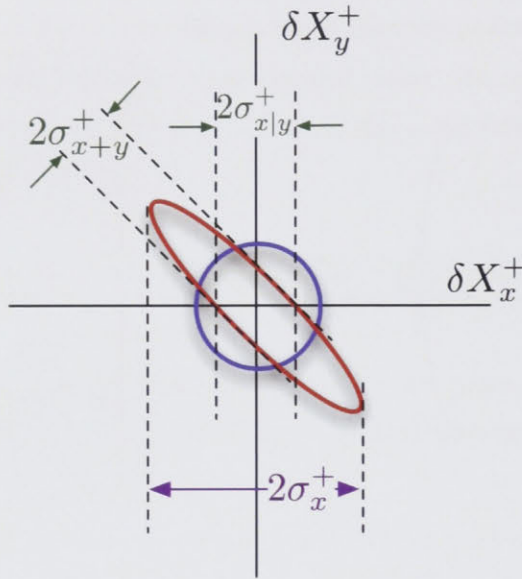


Figure 5.5: A correlation ellipse for the amplitude quadrature of symmetrically entangled beams. Some of the characteristics of the beams that can be found from the ellipse are marked.

experiment is outlined. The data was filtered for the range of frequencies between 0 and 4MHz in increments of 100kHz. The filter used was a sixth order Butterworth filter that is built into Matlab, and the width of the filter applied for each frequency increment was 100kHz^2 . The filter can be applied by taking the Fourier transform of the data, and then multiplying the resulting frequency spectrum by the filter function. This is equivalent to obtaining the Fourier transform of the filter function, and taking the convolution of the transformed filter function with the original data. Since the convolution method is substantially faster, it was used for this experiment.

The two resulting signals for a given sideband frequency, $\delta X_{x,\omega}$ and $\delta X_{y,\omega}$, can then be analysed as is required for the criterion being used. Here the sum or difference of the signals is taken for the amplitude and phase quadratures respectively, so that the Inseparability for the experiment can be found. The variance of the signals is then obtained by dividing the time-varying data into bins, and calculating the variance of each bin directly. Here the bins were set to 50,000 points, corresponding to 50ms of data for each value of variance found. The same process is performed for the quantum noise limit data, so that the variances can be compared

²This is equivalent to setting the RBW of the spectrum analyser to 100kHz.

5.3.3 Simultaneous squeezing measurements

The simultaneous squeezing measurements for the two modes are shown in Fig. 5.6. After detection on the quadrant detector, 1.7 dB of squeezing is measured in the two modes, which is sufficient for a clear demonstration of entanglement generation. Here it can be seen that a $\pi/7$ phase shift is present between the two fields, which might have an origin in a small misalignment of the OPA cavity.

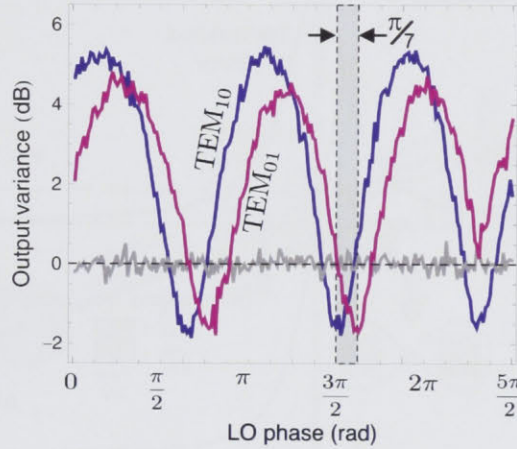


Figure 5.6: The squeezing and antisqueezing produced by the degenerate OPA in the TEM_{01} and TEM_{10} modes, as measured on a quadrant detector.

The intensity and phase responses for the transmission of our OPA is shown in Figure 5.7. The mean power and phase can be found from:

$$\begin{aligned}\tilde{P} &= \hbar f \langle \tilde{A}^\dagger \tilde{A} \rangle \\ \tilde{\phi} &= \sin^{-1} \frac{\langle \text{Im}(\tilde{A}) \rangle}{\sqrt{\tilde{P}}}\end{aligned}\quad (5.6)$$

where \tilde{A} is defined in Equation 2.39. For a perfectly aligned cavity, the two modes being transmitted are exactly in-phase. If there is a misalignment in the cavity, then there may be a slightly different cavity length for the TEM_{01} mode and the TEM_{10} mode, which then means that there will be a slightly different cavity frequency for the two transmitted modes. In our case, the cavity is locked to the TEM_{01} mode, and a small misalignment in the cavity means that this does not correspond exactly to being locked to the TEM_{10} mode. A slight mismatch has only a small impact on the power of the transmitted field (and hence the degree of squeezing) but results in a substantial change in the phase of the

transmitted beam. The vertical broken line in Figure 5.7 shows where a $\pi/7$ phase shift occurs for our cavity. The vertical broken line shows the effect that the cavity frequency mismatch has on the power of the transmitted mode - a power loss of just 2%. This type of cavity mismatch is the likely origin of the $\pi/7$ phase difference that we observe between the two squeezed modes.

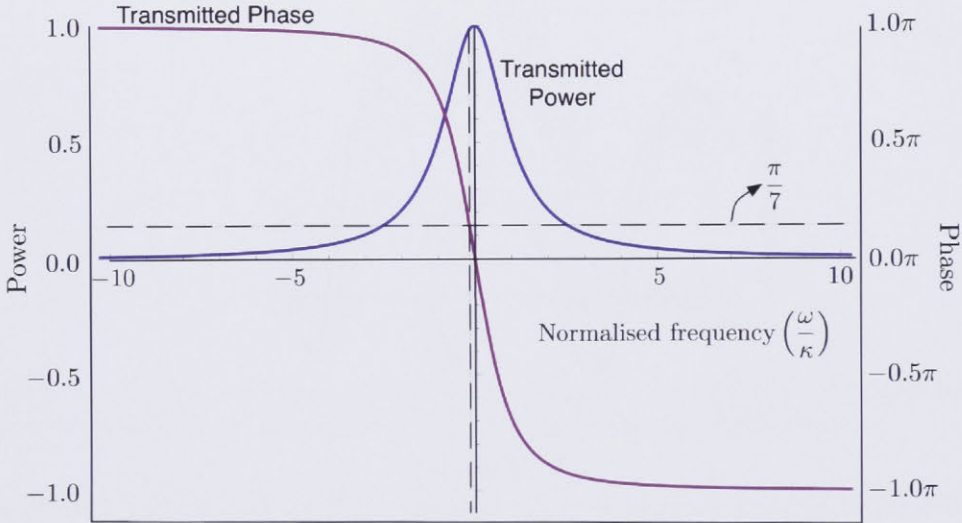


Figure 5.7: The intensity and phase response for the transmission of the OPA cavity. The misalignment that results in a $\pi/7$ phase shift between the two modes also results in a drop in power of 2%.

5.4 Entangling the two modes

There is a well-established set of requirements for entangling two optical beams, and we meet all of these in our unusual setup. A $\pi/2$ phase shift is first required between the two beams, which for standard entanglement is simply a matter of phase shifting one of the beams with respect to the other. The beams then need to be mixed together, which is generally achieved with a 50:50 beamsplitter. Finally, we need to observe a pair of conjugate observables, which requires a phase-sensitive detector in order to measure quadrature entanglement. This is usually achieved with one homodyne detector on each of the entangled beams.

5.4.1 Cylindrical lenses

In order to induce the $\pi/2$ phase shift we used an optical method employing the Gouy phase shift in higher order modes [54]. The output of the degenerate OPA was mode-matched into a symmetric two cylindrical-lens system (focal lengths $f=250$ mm, with lens separation of $\sqrt{2}f$), as shown in Figure 5.8. These cylindrical lenses then impart a $\pi/2$ phase shift on one of the modes, as seen by comparing the squeezing traces in Figures 5.6 and 5.9.

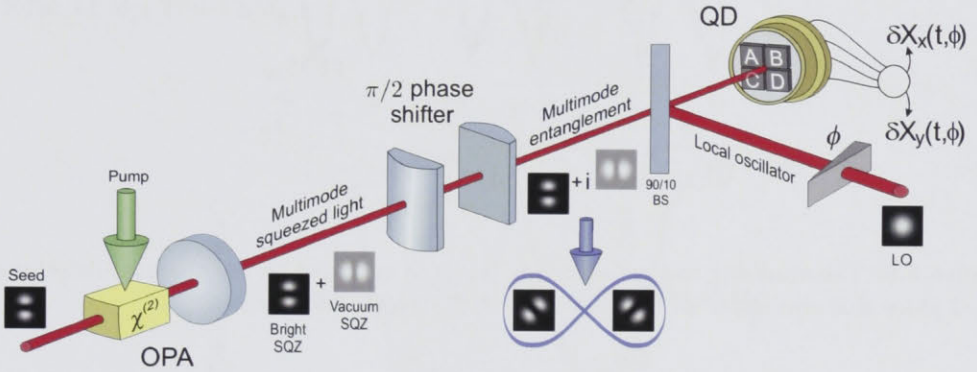


Figure 5.8: The setup for the entanglement experiment, with a pair of cylindrical lenses inducing a $\pi/2$ phase shift and a quadrant detector for simultaneous measurement of the two spatial modes. OPA: optical parametric amplifier; LO: local oscillator; HD: homodyne detection; QD: quadrant detector. Picture from [53].

The original modes detected, δX_x and δX_y are obtained from the quadrant detector shown in Figure 5.8 according to $\delta X_x = \delta X_{(A+B)-(C+D)}$ and $\delta X_y = \delta X_{(A+C)-(B+D)}$.

We then need to mix the TEM_{01} and TEM_{10} modes, equivalent to having a 50:50 beamsplitter. Any HG mode can be expressed as a superposition of two orthogonal modes of the same order as the original field. This is analogous to the superposition of polarization modes in a 2 dimensional basis. A TEM_{10} mode rotated by $\pm 45^\circ$ relative to the x -axis can be expressed as $\frac{1}{\sqrt{2}}\text{TEM}_{10} \pm \frac{1}{\sqrt{2}}\text{TEM}_{01}$. This means that our ‘beamsplitter’ can be realized by detecting in a basis that is 45° rotated relative to the axis of the cylindrical lens system. This new rotated detection basis is then written as $\delta X_{x'}$ and $\delta X_{y'}$. As expected from quantum theory, measurements of the arbitrary quadratures of entangled fields show noisy states, as seen in Figure 5.10. The variation in the output that can be seen arises because of the slight difference in the values for antisqueezing in the two original variance traces shown in Figure 5.6.

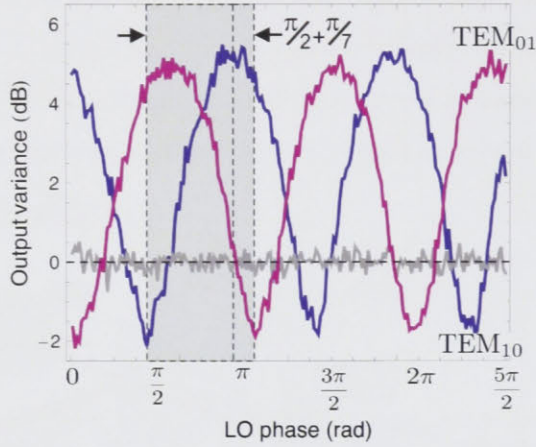


Figure 5.9: The squeezing and antisqueezing traces as measured on the quadrant detector after a $\pi/2$ phase shift was imparted onto one mode with the cylindrical lenses.

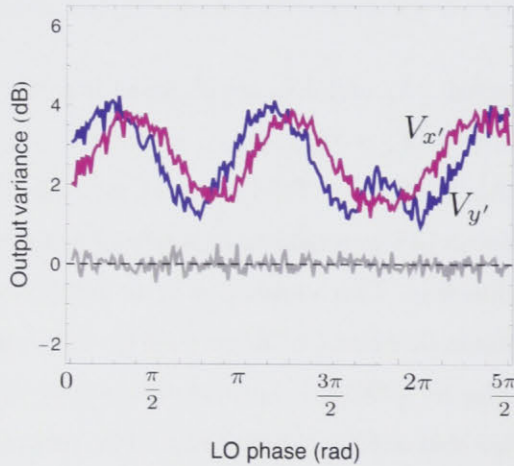


Figure 5.10: The quadrant detector rotated by 45° gives us the two entangled modes. The variance of this is higher than the QNL, as expected.

With these data we can calculate the Inseparability criterion \mathcal{I} , which is a direct witness of entanglement. With the sum and difference of the signals of the two orthogonal fields as introduced in Section 3.4.1, we evaluate the equation $\mathcal{I} = \sqrt{V_{x'+y'}(\phi_0) V_{x'-y'}(\phi_0 + \frac{\pi}{2})}$, where ϕ_0 is chosen such that \mathcal{I} is minimized. This results in values of \mathcal{I} that are lower than one over a range of detection frequencies, as shown in Figure 5.11. We demonstrate significant entanglement between two orthogonal spatial modes within one optical beam. This entanglement can be enhanced with the use of specially designed multi pixel detectors. This concept can be used to produce entanglement between any two orthogonal modes of the form TEM_{jk} and TEM_{kj} .

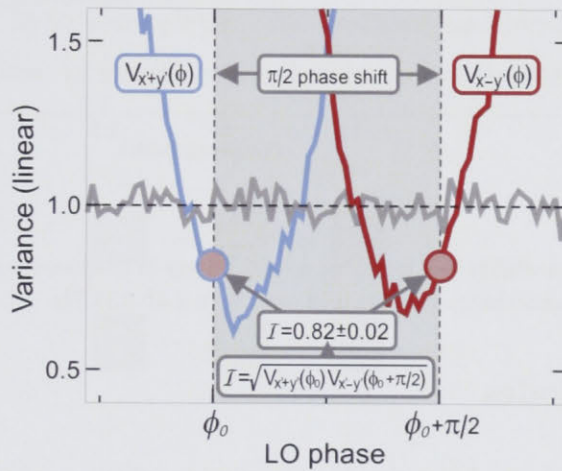


Figure 5.11: Results for Inseparability. Measurement of the variance for the sum $V_{x'+y'}(\phi)$ and difference $V_{x'-y'}(\phi)$ for the 45° rotated fields. The data, both below the QNL, are combined to one value for the inseparability.

An Inseparability of less than one can be found for a broad range of frequencies, as shown in Figure 5.12. The best value obtained occurred at 3.3MHz, and was found to be 0.79 ± 0.02 , after corrections are made for electronic noise.

During this same time frame, similar entanglement experiments were performed at the Technical University of Denmark by Lassen et. al. [55]. In this experiment, a single bow-tie squeezer was used to produce two squeezed modes (HG_{10} and HG_{01}), and measurements of the Hermite-Gauss modes were used to infer the entanglement between the $\text{LG}_0^{\pm 1}$ modes. The Denmark group used homodyne detection with a clever local oscillator beam layout that allowed them to measure different mode shapes. The group took noise measurements for HG_{10} , HG_{01} , and the $\text{LG}_0^{\pm 1}$ modes on the output of the OPO cavity.

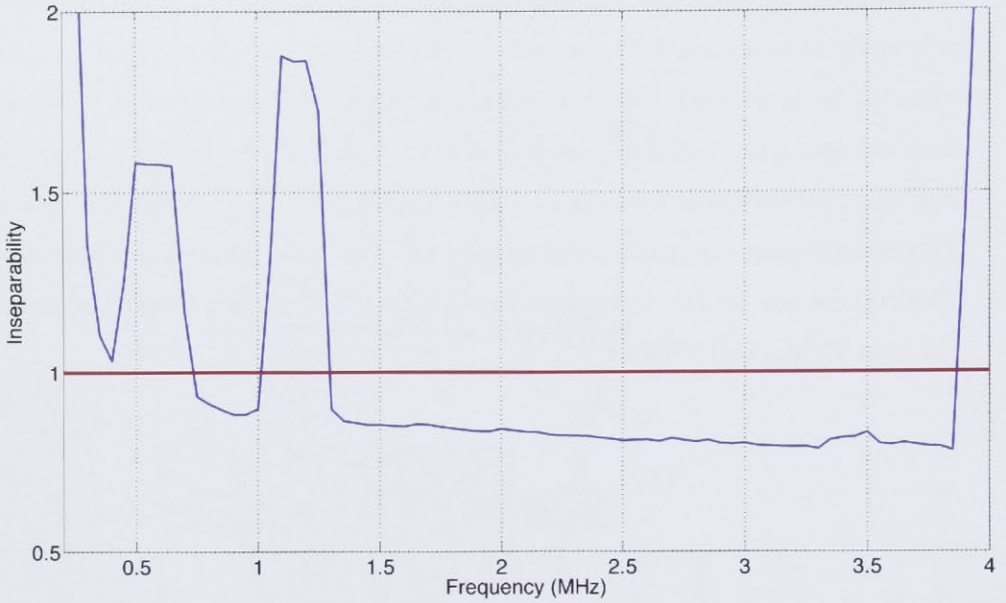


Figure 5.12: The inseparability was found for a broad range of frequencies at intervals of 100kHz. The lowest value for inseparability is 0.79 ± 0.02 , and occurs at 3.3MHz.

5.5 Spatial modes

The simplified mode profile for the fundamental mode, HG_{00} , can be found from Equation 2.30:

$$HG_{00} = A_{00}e^{-C_{00}(x^2+y^2)} \quad (5.7)$$

where A_{00} and C_{00} are constants that depend on the beam parameters.

The higher order HG modes that are of interest here are only slightly more complicated, with profiles given by:

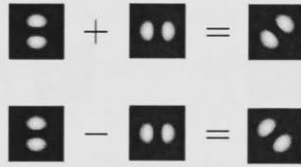
$$\begin{aligned} HG_{01} &= A_{01}e^{-C_{01}(x^2+y^2)}y \\ HG_{10} &= A_{10}e^{-C_{10}(x^2+y^2)}x. \end{aligned} \quad (5.8)$$

Let's assume that the modes are equivalent apart from the values of m and n , so that $A_{10} = A_{01}$ and $C_{10} = C_{01}$. In the experiment, we rotate the beam by $\pi/4$ about the z -axis using a Dove prism. If $a = HG_{01}$ and $b = HG_{10}$ are our original copropagating

squeezed modes and we apply the appropriate rotation matrix, the rotated HG modes can be described as:

$$\begin{aligned} HG_{10}^{R=\frac{\pi}{4}} &= \frac{A_{10}}{\sqrt{2}} e^{-C_{10}(x^2+y^2)}(y+x) = \frac{A_{10}}{\sqrt{2}}(a+b) \\ HG_{01}^{R=\frac{\pi}{4}} &= \frac{A_{10}}{\sqrt{2}} e^{-C_{10}(x^2+y^2)}(y-x) = \frac{A_{10}}{\sqrt{2}}(a-b). \end{aligned} \tag{5.9}$$

A rotation of the beam is then equivalent to mixing the two original modes. The beamsplitter expressions in Equation 2.16 show the same result when the relative phase difference between the two input beams is set to zero. The beam rotation in combination with the quadrant detector that remains oriented to measure the HG_{10} and HG_{01} modes is then the same as using a 50:50 beamsplitter. The rotational equivalence to mode mixing is shown graphically below. In the experiment, before rotating the beam we impart a phase



shift on the mode b using cylindrical lenses and the Gouy phase shift they impose. The Hermite-Gauss basis that we detect then corresponds to the equations:

$$\begin{aligned} \text{Det}_{HG_{01}} &= \frac{A_{10}}{\sqrt{2}} e^{-C_{10}(x^2+y^2)}(y+ix) = \frac{A_{10}}{\sqrt{2}}(a+ib) \\ \text{Det}_{HG_{10}} &= \frac{A_{10}}{\sqrt{2}} e^{-C_{10}(x^2+y^2)}(y-ix) = \frac{A_{10}}{\sqrt{2}}(a-ib). \end{aligned} \tag{5.10}$$



The expressions on the right hand side of Equation 5.10 are identical to the beamsplitter outputs in a standard entanglement setup, so this setup then has entanglement

between the detected HG_{01} and HG_{10} modes, as shown in the mode pictures above.

We measure the light using a homodyne detector where we scan the local oscillator phase to gain access to the different quadratures. For the equations, this corresponds to multiplication by an exponential term, so for an additional $\pi/4$ phase in the local oscillator:

$$\begin{aligned}
 \text{Det}_{HG_{01}}^{\phi_{rel}=\frac{\pi}{4}} &= e^{i\frac{\pi}{4}} \frac{A_{10}}{\sqrt{2}} e^{-C_{10}(x^2+y^2)} (y+ix) \\
 &= \frac{A_{10}}{\sqrt{2}} e^{-C_{10}(x^2+y^2)} \left[\frac{i-1}{\sqrt{2}} x + \frac{i+1}{\sqrt{2}} y \right] \\
 &= \frac{1}{\sqrt{2}} \left[\underbrace{\frac{A_{10}}{\sqrt{2}} e^{-C_{10}(x^2+y^2)} (y-x)}_{HG_{01}^{R=\frac{\pi}{4}}} + i \underbrace{\frac{A_{10}}{\sqrt{2}} e^{-C_{10}(x^2+y^2)} (y+x)}_{HG_{10}^{R=\frac{\pi}{4}}} \right] \quad (5.11)
 \end{aligned}$$

This is shown graphically below.

$$e^{i\frac{\pi}{4}} \left(\begin{array}{c} \text{HG}_{01} \\ + \\ i \text{HG}_{10} \end{array} \right) = \begin{array}{c} \text{HG}_{01}^{R=\frac{\pi}{4}} \\ + \\ i \text{HG}_{10}^{R=\frac{\pi}{4}} \end{array}$$

For the experiment, we arranged the beam orientation with respect to the detector so that we detected the ideal quadratures for entanglement while simultaneously having a 50:50 beamsplitter ratio. In the mode diagram above, we can see that as the local oscillator angle changes, the detected modes also change. Given the previously discussed equivalence between beam rotation spatial mode mixing, we must be careful when interpreting results for quadratures other than the entanglement quadratures, since here we are no longer simply mixing the two modes on a 50:50 beamsplitter.

5.6 Future work

Here we have demonstrated a simplified optical setup for two mode entanglement using two spatial modes in a single beam. Ultimately, the motivation for this experiment involves the expansion of multimode entanglement into more orthogonal spatial modes, to make the system more scalable and therefore a possible tool in future quantum networks.

The current setup for imparting a $\pi/2$ phase shift onto one of the modes with respect to the other involves a pair of cylindrical lenses. This system as it is set up here only

works for entangling TEM_{nm} mode with TEM_{mn} mode, and could be adapted for other pairs of spatial modes, though it would be more difficult. One of the motivations behind performing an entanglement experiment using different spatial modes on a single beam is the potential for scalability in the design, and use of cylindrical lenses to impart a phase shift would no longer be a simple task for more than two spatial modes. To this end, the research is currently being extended by the design of a universal mode converter. Mode conversion can be achieved using a series of *spatial light modulators*, or SLMs, with a Fourier transform in between each pair of SLMs. This system would allow both changes in the intensity and the phase of the output beam. The current incarnation of the mode converting device uses a single SLM, but has the light interacting with just one portion of the surface before being Fourier transformed and then focussed onto a second portion of the SLM surface. In this way, the single SLM is used to modulate the beam three times.

The mixing of the two modes was achieved in this experiment by rotating the quadrant detector that was used by $\pi/4$. This technique is not, in general, applicable to other spatial modes available, but the use of the mode converter described above would allow mixing between different spatial modes in the required ratios.

The detection was performed with a quadrant detector, with adjustments on the gain of the different quadrants in order to obtain detector eigenmodes that are a reasonable match for the spatial modes being measured. As the number of spatial modes that must be detected increases, so too must the number of pixels in the detector, in order to distinguish between the spatial modes present.

5.7 Conclusion

We have demonstrated an elegant technique to create and measure entanglement between two orthogonal spatial modes in a single beam of light. We have shown and tested several simplifications to traditional entanglement schemes, including generating two squeezed modes from a single OPA, using imaging components to mix the modes with the correct phase and detecting the two modes simultaneously with one quadrant detector. The results for two modes are complementary to those that can be achieved with polarisation techniques. However, this technique has the potential to be expanded to several higher order TEM_{mn} modes, creating a larger number of quantum channels.

The tools for a multimode system are being developed. We can already synthesize a

beam with several higher order spatial modes from several sources of squeezed light [48]. The mixing and entanglement could be performed for a larger number of modes using imaging techniques, such as employing a programmable spatial light modulator. One multi pixel detector with multiple gain functions applied to match the field amplitude of each orthogonal mode could be used to make simultaneous measurements of all the higher order spatial modes with one local oscillator. Accessing this expanded basis of quantum information channels within a single beam and the possible manipulation of the modes makes this technology a practical contender for optical multimode quantum communication systems.

Asymmetric entanglement

In any real entanglement experiment, there will always be losses due to the various components that are a part of the system. Normally, the assumption is made that the losses in the experimental setup occur in a symmetric fashion, but in some cases the distribution of the losses may occur in such a way that it introduces an asymmetry in the experiment - for instance, there could be a loss on one entangled arm, but not the other. Other asymmetries can emerge from having non-identical squeezers, or from deliberately limiting the number of squeezers used, and it is worthwhile to investigate these asymmetries in order to be able to effectively optimise a system.

6.1 Direction of inference

When measuring the EPR value in an entangled system, the direction of the inference that is being made can in some cases be important. The EPR value depends on the conditional variance of the system (see Equation 3.33), and the conditional variance essentially involves the measurement of one beam and the use of this value to infer the measurement that will be made on the other beam. There are two conditional variance measurements that can be made: $V_{x|y}$ and $V_{y|x}$, as defined in Equation 3.35. In the former, beam y is measured and used to predict beam x , and in the latter, beam x is measured and used to predict beam y , as explained in Section 3.4.2. These measurements are termed direct reconciliation and reverse reconciliation respectively. The two EPR values are found from these conditional variances, with $\epsilon_{x|y} = V_{x|y}^+ V_{x|y}^-$ and $\epsilon_{y|x} = V_{y|x}^+ V_{y|x}^-$.

In order to investigate the effects of losses in the system, we must first identify the possible places where losses can occur. Figure 6.1 shows a standard setup, with input beams 1 and 2, and output beams x and y . Here the OPAs and the homodyne detectors are considered to be perfect, with any losses at these elements combined into the generic losses at the appropriate positions. Each beam has a power transmission given by η_1, η_2 ,

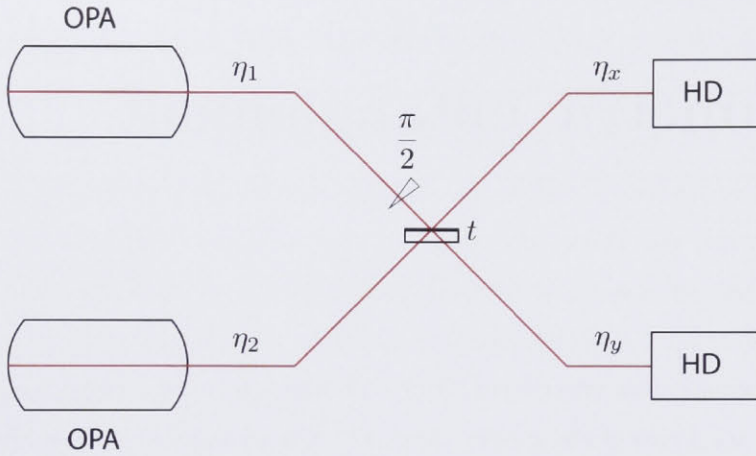


Figure 6.1: A standard entanglement experiment, showing where the losses can fall.

η_x , or η_y , and the loss on each beam is then $1 - \eta$. Note that this simple model assumes that there is no excess noise being coupled into the system.

One method of visualising the correlations that exist between the two beams is by drawing correlation ellipses, as seen in Section 3.4. This corresponds to parametrically plotting the measurements of x and y for a given quadrature until a statistical sample is obtained, and then drawing a line where the standard deviation of the distribution falls. This line ends up being an ellipse, and this can then be compared to the corresponding shot noise circles to understand the various entanglement measures. As seen in Section 3.4, the ellipses can be used to find many values that might be of interest in an experiment; V_x , V_y , $V_{x|y}$, and V_{x+y} can all be found from the ellipses.

Figure 6.2a uses these correlation ellipses to show the different measurements that lead to the two possible EPR values. This case has two 6dB squeezers incident on a 50:50 beamsplitter, with no losses in the system. For the ellipses shown here, the two measurements that can be made, $\epsilon_{x|y}$ and $\epsilon_{y|x}$, are identical, due to the symmetry of the system. When there are no losses present in the system, the semi-minor axis on the ellipse for one quadrature is the inverse of the semi-major axis on the ellipse for the other quadrature, when all measurements are normalised to the QNL. This shows that the state, if Gaussian, is minimum uncertainty, and is analogous to the case when the two quadratures for a squeezed state have a product of one. As expected, losses then increase this product.

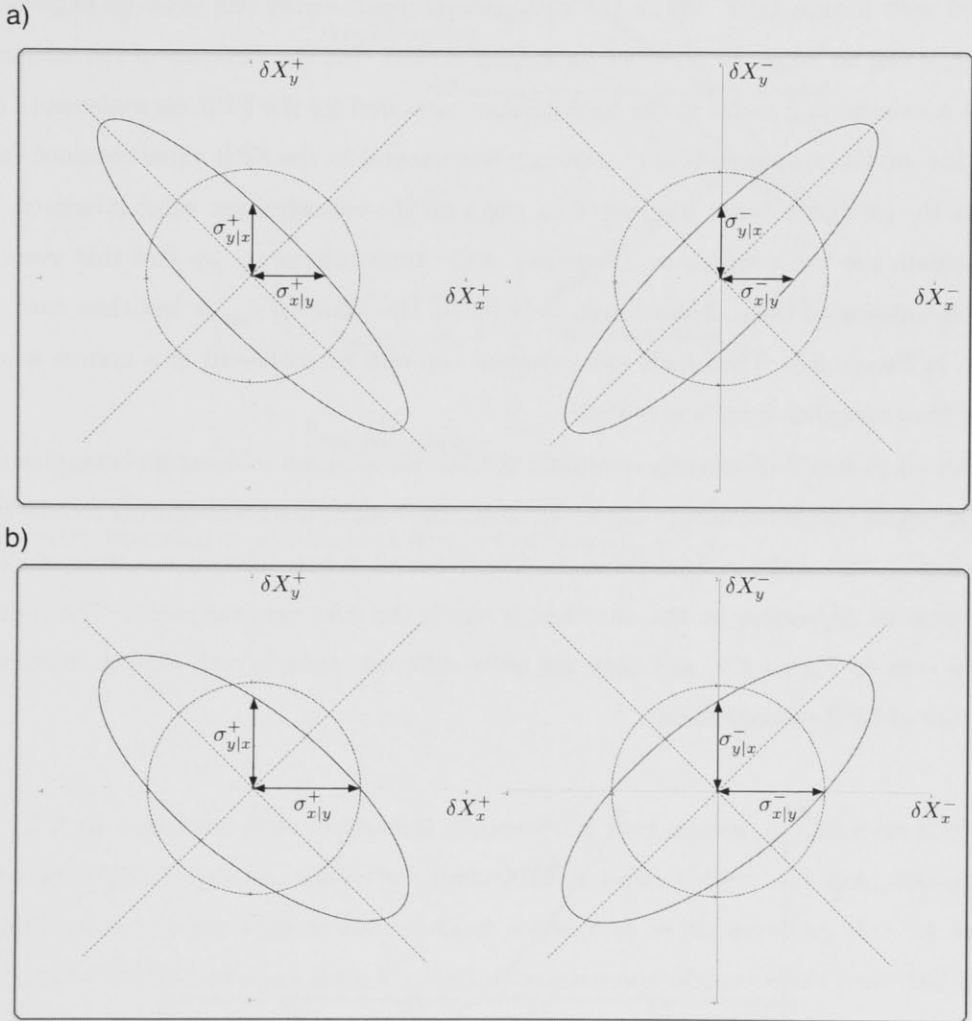


Figure 6.2: a) Correlation ellipses for a symmetric system, with $\eta_1 = \eta_2 = \eta_x = \eta_y = 1$. The initial amount of squeezing is set to 6dB. The circles show the quantum noise limit, and the conditional deviation is marked. The conditional variance is the square of this value, $V_{x|y} = (\sigma_{x|y})^2$. b) Correlation ellipses for a system with two 6dB squeezers incident on a beamsplitter. The y beam then undergoes a 50% loss, while the x beam has perfect transmission. EPR entanglement can now be seen with the measurement of $\epsilon_{y|x}$, but not with $\epsilon_{x|y}$.

If we consider the case where an extra loss is applied to one of the entangled arms, but not the other, then we arrive at the ellipses shown in Figure 6.2b. Here we have the same 6dB squeezers, but there is a 50% loss on the y beam after the beamsplitter. Now the ellipses are wider, and there is no longer symmetry about the diagonal axes, which are marked with broken lines. While the EPR measurement would still show entanglement for $\epsilon_{y|x}$, it can no longer be observed for $\epsilon_{x|y}$. It is clear that the direction of the inference is now a determining factor in the final number measured for the EPR entanglement. An extra loss on the measured beam is strongly detrimental to the EPR value obtained, but loss on the predicted beam has less of an effect on the entanglement value measured. If we evaluate the two ϵ values as a function of the transmission η_y , we find that even as the transmission of the y channel approaches zero, the value for $\epsilon_{y|x}$ is less than one¹, as shown in Figure 6.3. Thus EPR entanglement can still be witnessed in a system where one of the entangled arms is very lossy.

This effect was inadvertently encountered while the position-momentum entanglement of laser beams was performed (Chapter 4). Here, the beamsplitter was causing an effective extra loss on one of the entangled beams. This resulted in two different measures of EPR entanglement depending on the direction in which the inference was made. The results can be seen in Figure 6.4, and they are quite different, though each clearly shows the existence of EPR entanglement.

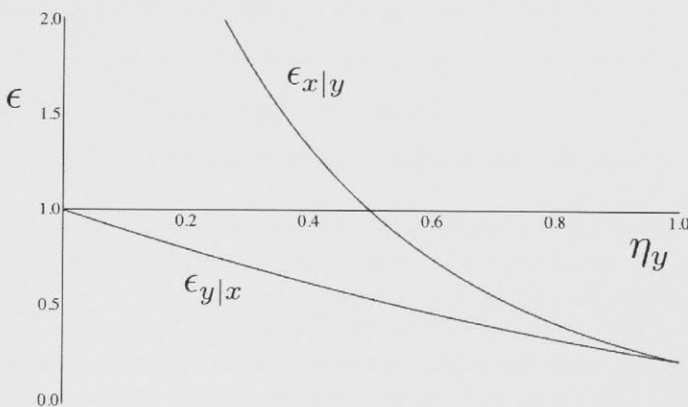


Figure 6.3: Measure of EPR entanglement, $\epsilon_{x|y}$ and $\epsilon_{y|x}$ for a system with two 6dB squeezers incident on the beamsplitter. The transmissions η_1 , η_2 and η_x are one, and the transmission η_y varies from 0 to 1.

¹Note that this is no longer the case if there is any loss on the squeezed beams before the beamsplitter.

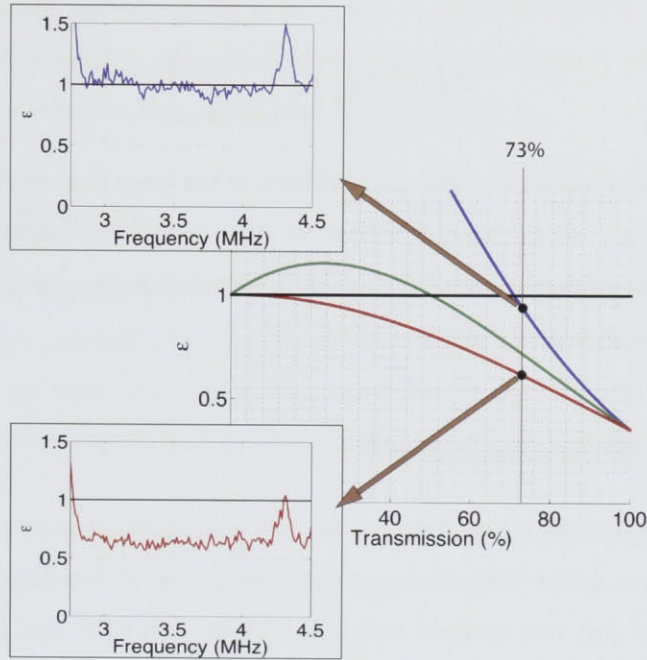


Figure 6.4: The continuous variable position-momentum entanglement experiment, showing an asymmetry depending on whether the inference made was $\epsilon_{x|y}$ or $\epsilon_{y|x}$.

EPR entanglement from directional measurement is of interest to Quantum Key Distribution (QKD) systems, where two parties, often termed Alice and Bob, attempt to establish a secure key while in the potential presence of an eavesdropper, Eve. A secure key can be established when there is a net information rate of greater than one [56]. Once a secure key has been established, the key can then be used to send encrypted information between the two parties. Reverse reconciliation is used in cryptography protocols: if Alice is creating the data to establish a key, then her measurement can be expected to have a lower loss than Bob's measurement, since his beam has travelled through a channel with some loss [57]. The two measurements must then be compared either by Bob predicting Alice's measurement (direct reconciliation) or by Alice predicting Bob's measurement (reverse reconciliation). The net information rate is then given by

$$\Delta I = \frac{1}{2} \log_2 \left(\frac{V_{A|E}^+ V_{A|E}^-}{V_{A|B}^+ V_{A|B}^-} \right) \quad (6.1)$$

for direct reconciliation or

$$\Delta I = \frac{1}{2} \log_2 \left(\frac{V_{B|E}^+ V_{B|E}^-}{V_{B|A}^+ V_{B|A}^-} \right) \quad (6.2)$$

for reverse reconciliation. Reverse reconciliation is the more favourable option, because of the loss experienced on the beam measured by Bob. This is equivalent to using $\epsilon_{y|x}$ instead of $\epsilon_{x|y}$ above. A review of quantum information protocols in the continuous variable regime can be found in Braunstein and van Loock [58].

6.2 Biased entanglement

In all of the experiments considered so far, the entanglement has been the result of two similar squeezers whose outputs were mixed with a 50:50 beamsplitter. It is possible, however, to use just one squeezer and still achieve both EPR and Inseparability entanglement. This experimental setup is known as *biased entanglement* [59], and while the entanglement doesn't exhibit the same degree of correlation as the more standard setup, the corresponding simplification of the experiment can prove to make this a worthwhile concession. Apart from negating the necessity of building and locking one extra squeezer, having one vacuum input into the beamsplitter means that the usual need to mode match the beams and lock the phase of the beams is no longer relevant.

The biased entanglement setup used in [59] consisted of a single squeezer and a 50:50 beamsplitter. This is equivalent to the setup shown in Figure 6.1 with $\eta_2 = 0$. The two output beams can then be described as:

$$V_x^\pm = V_y^\pm = \frac{1}{2} (V_1^\pm + 1) \quad (6.3)$$

and the EPR measure is found to be:

$$\epsilon_{x|y} = \frac{4V_1^+ V_1^-}{V_1^+ V_1^- + V_1^+ + V_1^- + 1}. \quad (6.4)$$

For a biased entanglement setup with a 50:50 beamsplitter, the existence of EPR entanglement can only be measured for a transmission $\eta_x > \frac{2}{3}$. A setup with $\eta_x = \eta_y = 1$ results in the correlation ellipses shown in Figure 6.5a. One of the axes of each ellipse is

coupling in vacuum noise, and so are the same as the quantum noise limit. Adding a loss to the squeezer (by decreasing η_1 from one) changes one axis on each of the ellipses, and as expected leaves the other unchanged, as seen in Figure 6.5b.

6.2.1 Beamsplitter Ratio

The 50:50 beamsplitter that has featured in experiments until now is the optimal ratio for symmetric setup, but it can easily be changed should a different ratio be preferable for a given experiment. If we investigate the more general case of any beamsplitter ratio in a biased entanglement setup, we instead get two output beams with variance:

$$\begin{aligned} V_x^\pm &= V_1^\pm (1 - t) + t \\ V_y^\pm &= V_1^\pm t + (1 - t). \end{aligned} \tag{6.5}$$

where t is the transmission of the beamsplitter used.

In terms of the correlation ellipses, such a change in beamsplitter ratio corresponds to a rotation of the ellipses from their original positions. The angle of the ellipse axis is then given by $\phi = \frac{\pi}{2}t$, as shown in Figure 6.6.

Such a rotation can lead to an improvement in the EPR entanglement for one direction, at the expense of the EPR entanglement in the other direction, as seen graphically in Figure 6.6.

The EPR measurement that can be made is then:

$$\epsilon = \frac{V_1^+ V_1^-}{(1 + t(V_1^- - 1))(1 + t(V_1^+ - 1))}. \tag{6.6}$$

In the absence of asymmetric losses after the beamsplitter, the ideal transmission, as given by differentiating the EPR value with respect to t , is given by:

$$t_{opt} = \frac{1}{2\eta_1}. \tag{6.7}$$

This is shown in more detail in Appendix 2.

If the beamsplitter is set to the optimum value, then the minimum transmission required on the squeezed beam to observe EPR entanglement decreases from $\eta_1 > \frac{2}{3}$ to

$\eta_1 > \frac{1}{2}$. This is shown for the case of a 6dB squeezer in Figure 6.7. Note that for a symmetric entanglement experiment with two identical squeezers, the transmission on each squeezer must be $\eta > \frac{1}{2}$ in order to measure EPR entanglement. While biased entanglement with a 50:50 beamsplitter requires a high quality squeezer, the use of a variable beamsplitter enables EPR entanglement measurement with any squeezer that would be sufficient for a symmetric two-squeezer experiment.

Figure 6.8 shows the EPR value for a varying transmission for the squeezer and a varying beamsplitter transmission, t . The section to the right of the EPR entanglement boundary show where the value of $\epsilon_{x|y}$ gives a value of less than one. The position that corresponds to a beamsplitter ratio of 0.5 is marked with the horizontal line. The loss of the squeezer that was used to test the theoretical results is shown with the vertical broken line.

The same technique can be applied to help counteract asymmetries in two squeezer setups, or when the Inseparability is the entanglement criterion that is of interest. The effect of the optimisation is the greatest for EPR entanglement because the direction of the inference made is important. The results for the optimal beamsplitter ratio for cases other than the EPR entanglement with a biased setup are shown in Appendix 2.

While improving the EPR value is by no means evidence of there being “more” entanglement than there was previously, there are some applications where lowering the EPR value is necessary. For example, the information transfer rate for QKD systems is strongly dependent on the EPR value of the system. Similarly, teleportation of an arbitrary state requires the existence of EPR entanglement.

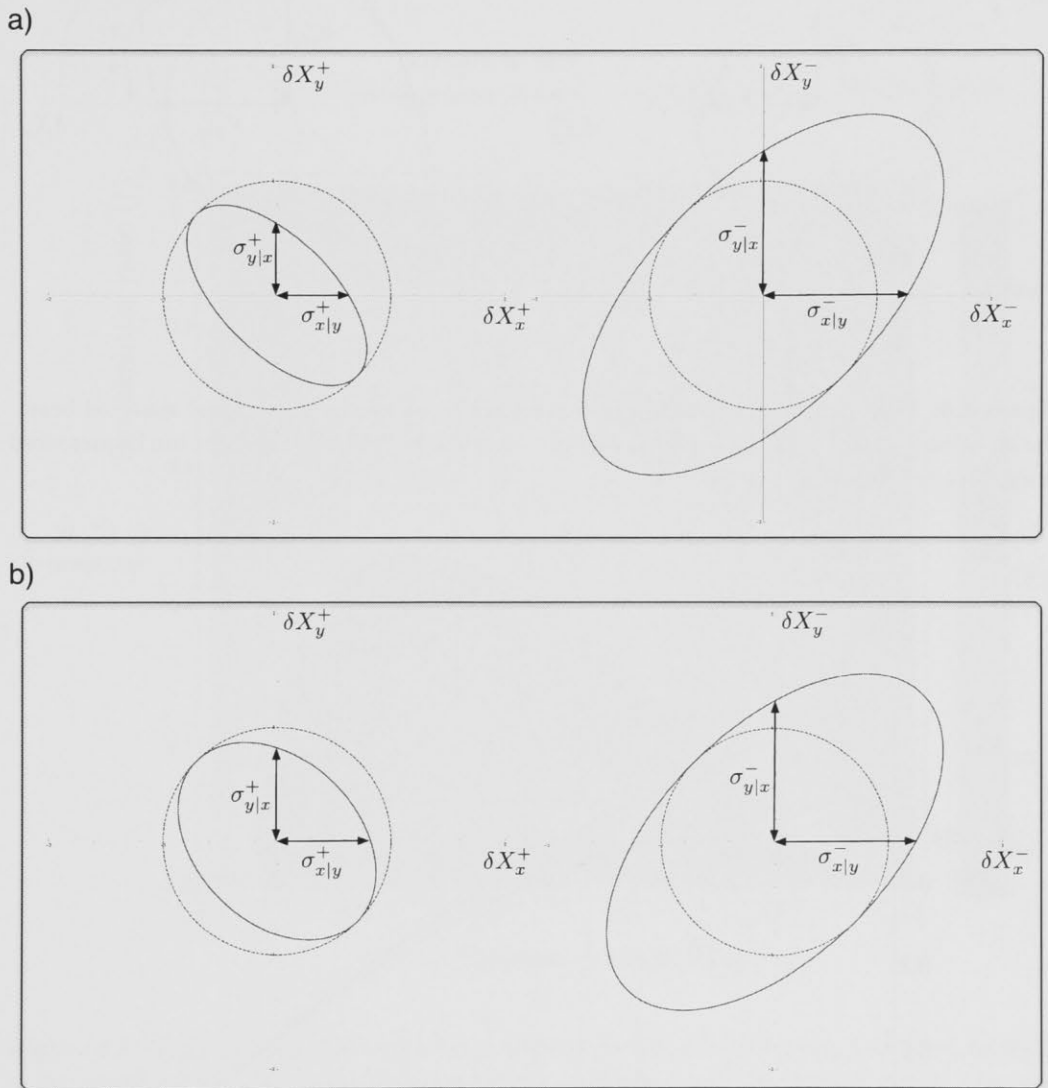


Figure 6.5: a) The correlation ellipses resulting from a biased entanglement experiment, with no loss on the original squeezed beam. The squeezer used here is 6dB. b) A biased entanglement experiment with a loss on the single squeezer.

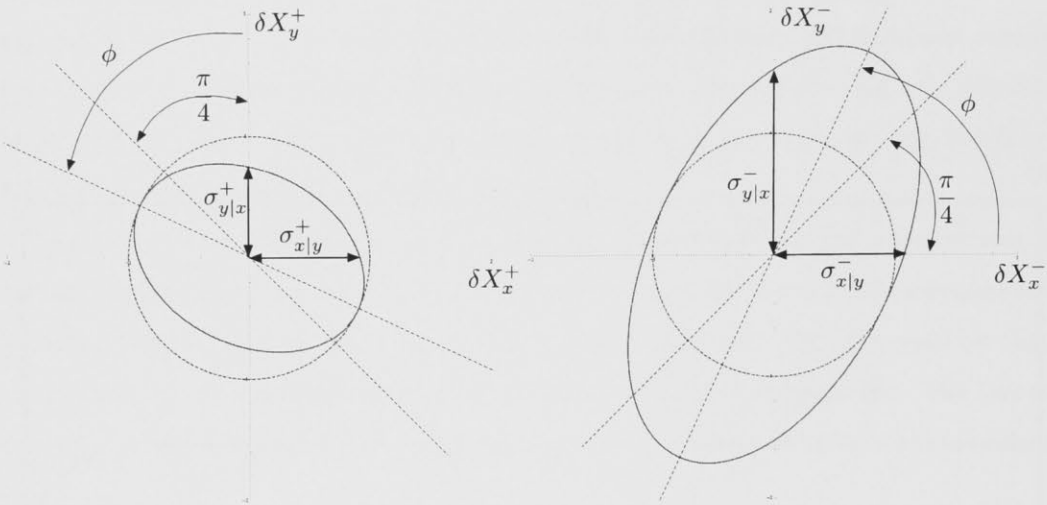


Figure 6.6: Here the biased entanglement experiment has a loss on the original squeezed beam. The beamsplitter used is 80:20 ($t = 0.8$ in Figure 6.1), and now EPR entanglement can be measured for $\epsilon_{x|y}$ but not for $\epsilon_{y|x}$.

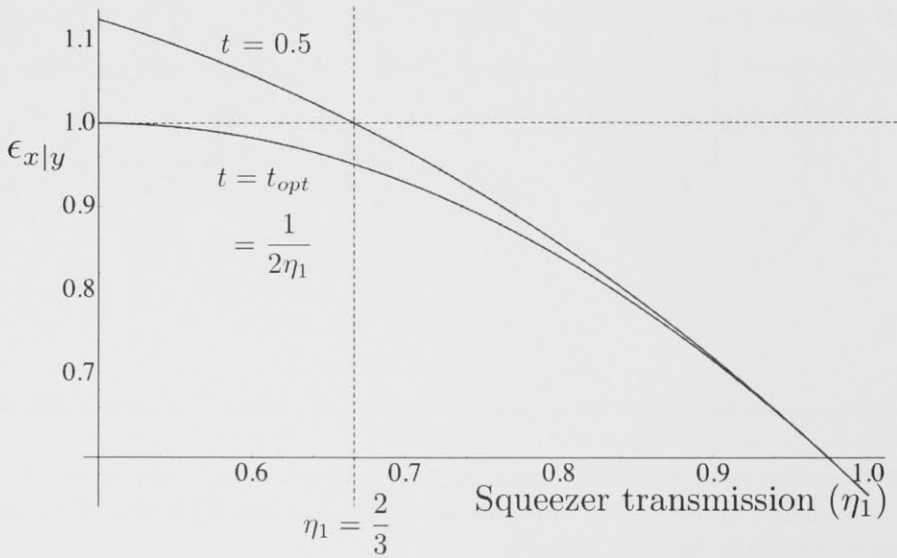


Figure 6.7: The theoretical measurement of EPR entanglement in one direction for a setup with a 50:50 beamsplitter ($t = 0.5$), and a setup where the beamsplitter ratio has been optimised according to the loss in the system ($t_{opt} = \frac{1}{2\eta_1}$).

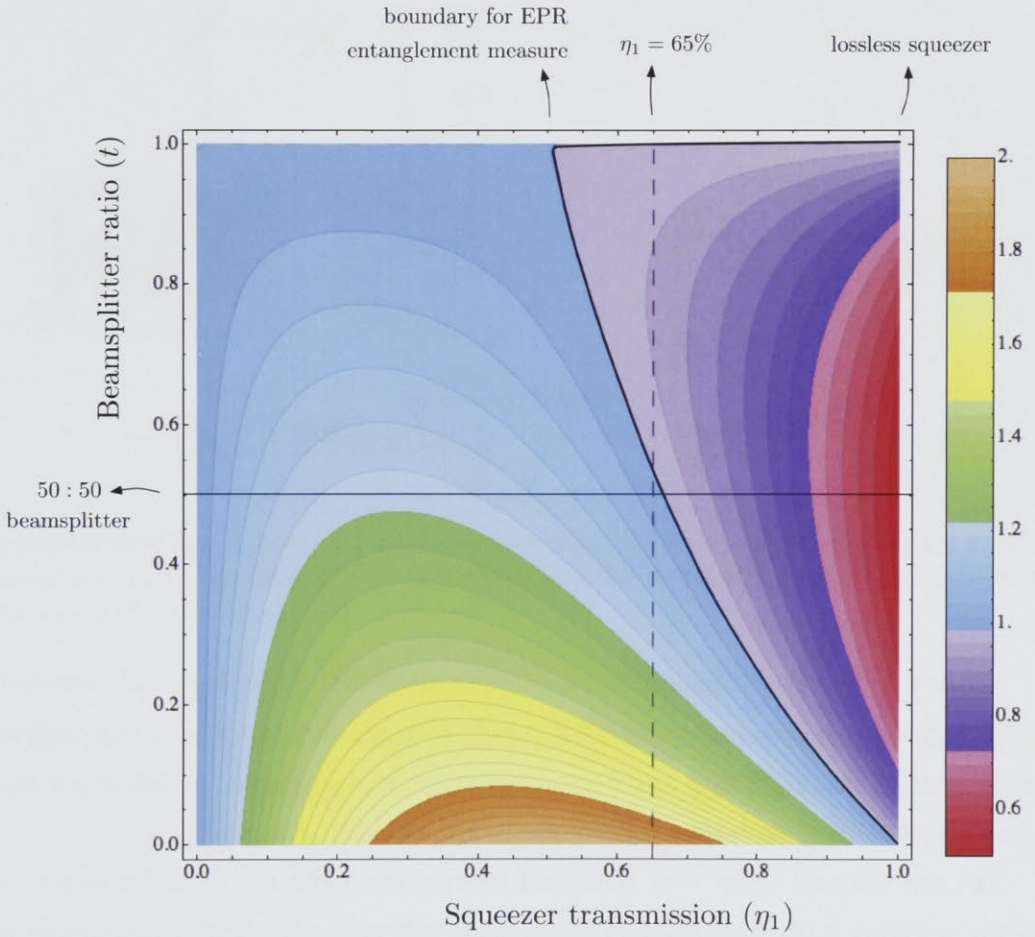


Figure 6.8: The theoretical EPR value for a biased entanglement experiment, with a varying value of loss on the squeezer (the transmission η_1) and a varying beamsplitter transmission, t . The usual case for a beamsplitter ratio being 0.5 is marked with the horizontal line, and the transmission of our squeezer at the time of the experiment is marked with the vertical broken line.

6.2.2 Experimental Details

An entanglement experiment was performed in order to test the theoretical results that show that EPR measurements can be improved in some instances by changing the beamsplitter ratio. For a given value of loss before the beamsplitter, the beamsplitter ratio was varied, and the EPR value measured at each ratio.

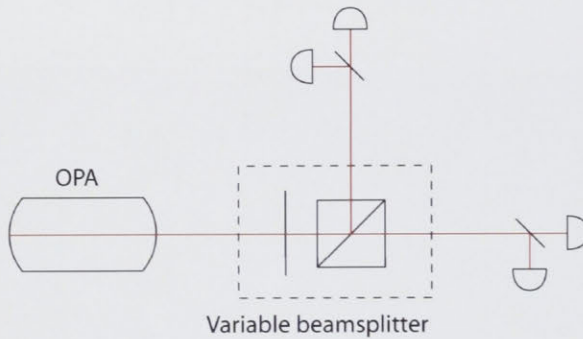


Figure 6.9: The biased entanglement experiment had a linear OPA, with a variable beamsplitter consisting of a half wave plate and a PBS, and two homodyne detectors.

Figure 6.9 shows the simplified setup for the experiment. There is a single squeezer, and a half wave plate in combination with a polarizing beamsplitter is used as a variable beamsplitter. There are then two homodyne detectors to measure the amplitude and phase information of the beams.

The experimental setup with additional information about the detection system is shown in Figure 6.10. This diagram shows extra half wave plate/PBS combinations in several beams in case we wished to put extra losses on the beams before or after the main entangling beamsplitter. Ultimately, the original loss in the system was high enough that adding extra losses does not result in EPR entanglement, so these results are not included in this section.

The data was recorded using the data acquisition system previously described in Section 5.3.2. Each detector has two outputs - the high frequency signal (termed AC, or alternating current) and the low frequency signal (termed DC or direct current). As in Section 5.3.2, the δX_x and δX_y signals from the subtracted homodyne detectors are sampled at 10MHz, and the data is processed later. The slow acquisition, at 10kHz, was used

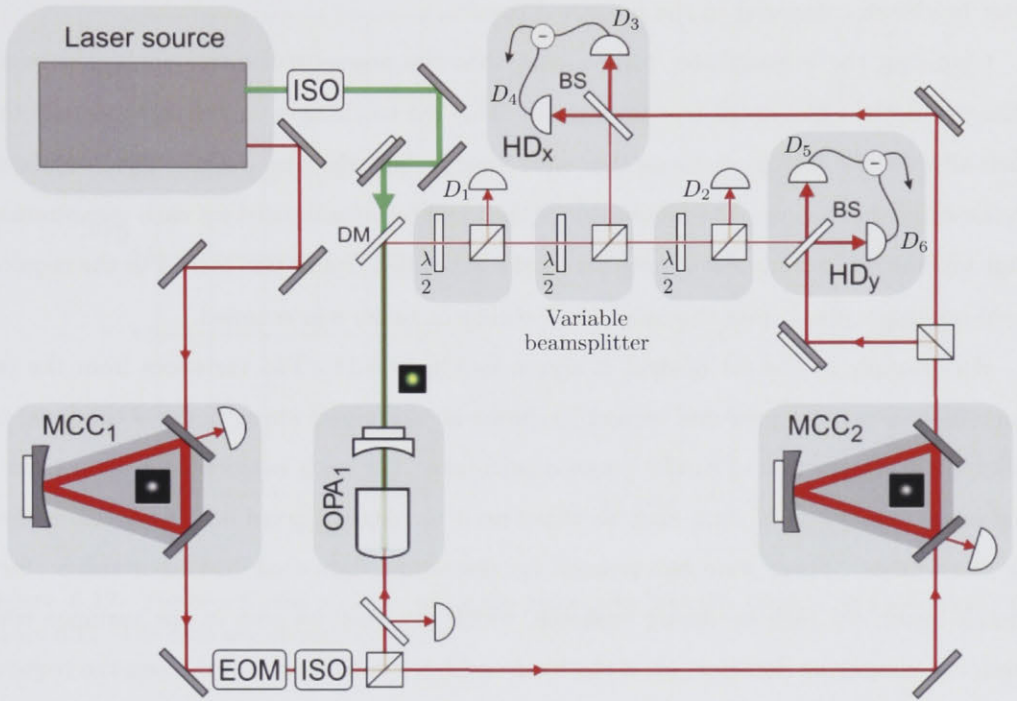


Figure 6.10: The experimental setup for the experiment. The experiment had several detectors to record both the instantaneous changes at the homodyne detectors and the DC power measurements for finding the beamsplitter ratio t .

to find the amount of power on each of the detectors, which was then used in combination with the a Labview programme to find the transmission of the entangling beamsplitter. This can be found from the detector DC signals shown labeled in Figure 6.10:

$$t = \frac{D_5 + D_6 + D_2}{D_5 + D_6 + D_2 + D_3 + D_4} \quad (6.8)$$

and this can be used in real time to adjust the ratio by rotating the half wave plate.

The data was post processed using Matlab to obtain the variances for the different values that were required, using the same details used in Section 5.3.2. The values of t , V_x and V_y for the phase and amplitude quadratures were used to work out the original amount of squeezing as accurately as possible. For each different beamsplitter transmission, these values can be used with Equation 6.5 to find the original squeezing and antisqueezing. The output of the OPA was found to be 2.9dB of squeezing and 5.3dB of antisqueezing.

These values were then used to find the theoretical results for the experiment that will later be shown compared to the measured results.

Changing the beamsplitter ratio meant that the power in the two entangled beams changed as the experiment was performed. This led to changes in the error signals that then affected the locking systems that were used to lock the phase of the local oscillators to the entangled beams. The locking loops then had to be optimised for each measurement that was made. In some cases, only one of the entangled beams was locked to the required local oscillator phase, and the other local oscillator beam was scanned.

An example of one set of data is shown in Figure 6.11. The variances from the two homodyne detectors over one second is shown in this case, where both of the local oscillator beams are locked to the phase quadrature. For each beamsplitter ratio used in the experiment, sets of data such as those used to obtain Figure 6.11 were taken three or more times. There were two reasons for discarding data that had been taken: for a locked beam, the lock becoming unstable, which can then be seen in the variance trace from the homodyne detector; or, if the local oscillator is being scanned, then the required quadrature might not be reached in some cases, making the data unusable.

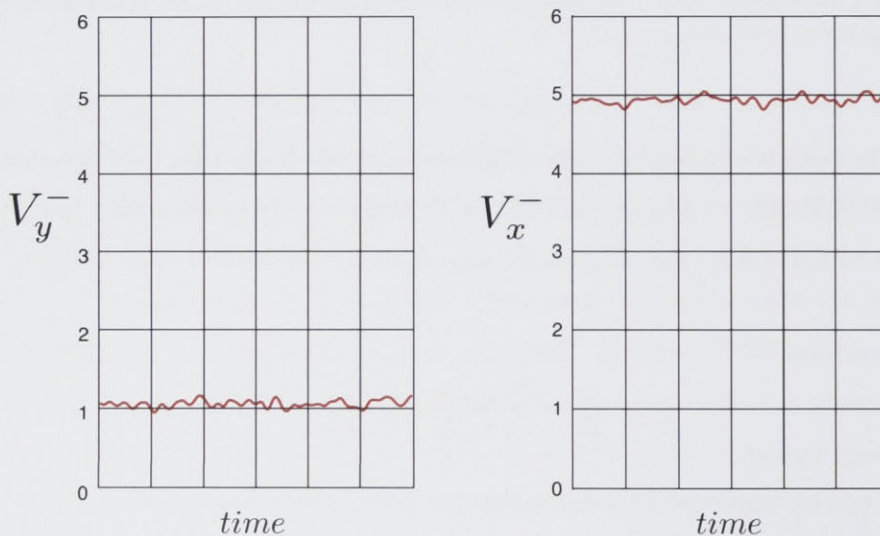


Figure 6.11: The variances for the two homodyne detectors. The data are normalised to one.

Using the same data that yields the variance for each homodyne detector, the conditional variance was found for both quadratures at every beamsplitter ratio investigated. This is shown for the example case in Figure 6.12, for the beamsplitter ratio of $t = 0.1$.

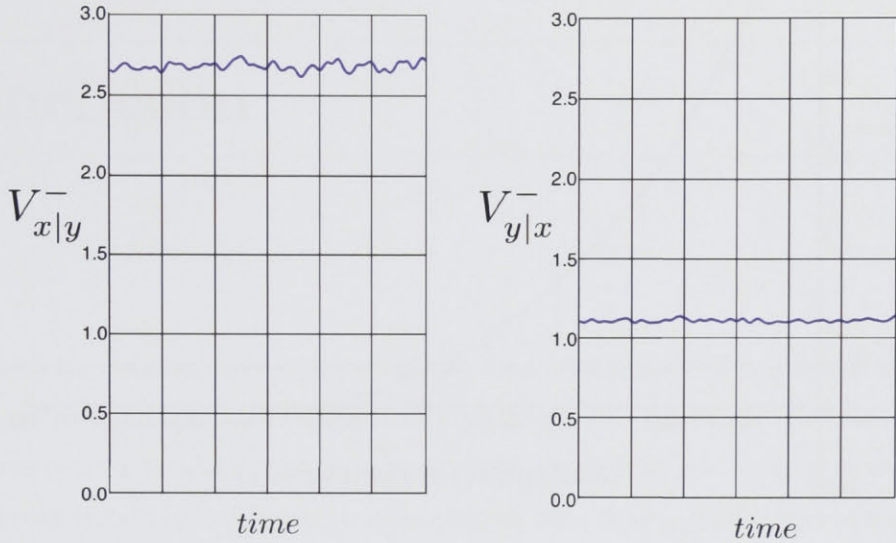


Figure 6.12: The conditional variance using the same data that was used to find the results in Figure 6.11. The data are normalised to one.

The results for the EPR entanglement with a varying beamsplitter ratio are shown in Figure 6.13, alongside the theoretical curve for the experiment. The theoretical curve is calculated using the known characteristics of the squeezer, which produces 2.9 dB of squeezing and 5.3 dB of antisqueezing, as discussed previously. The agreement between the measured and theoretical values is within experimental error, and EPR entanglement is achieved with a beamsplitter transmission of 0.78, but is not achieved with a more traditional beamsplitter transmission of 0.5. At a beamsplitter ratio of 0.78, an EPR value of 0.96 ± 0.02 was obtained. The error arises from the changes in the variance due to the locking systems.

6.3 Conclusion

We have shown that the direction of the inference that is made to perform an EPR measurement is important in cases where there is an asymmetry in the experiment. It was found that changing the beamsplitter ratio could optimise the measurement made for a lossy system, in some cases enabling an EPR measurement to be made when it would otherwise not be possible. In the case of a biased entanglement setup, with just one squeezer, the ideal beamsplitter ratio was found to be $t_{opt} = \frac{1}{2\eta_1}$. This was verified by

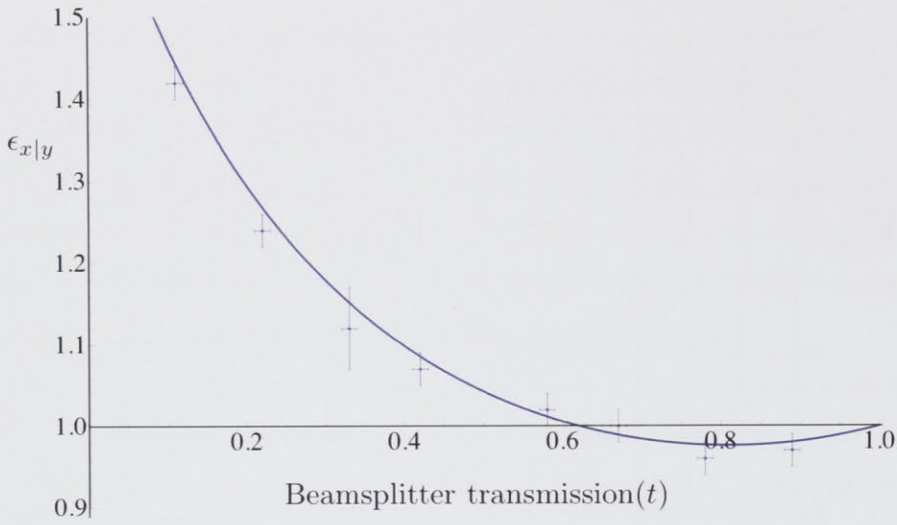


Figure 6.13: The results of the biased entanglement experiment, showing the measured EPR entanglement ($\epsilon_{x|y}$) for a varying beamsplitter ratio, t . The line is the theoretical curve based on the original level of squeezing and antisqueezing.

performing a biased entanglement experiment, with EPR entanglement measured when it could not have been measured using a 50:50 beamsplitter.

Conclusion

This thesis has detailed three experiments that have been performed that match two general aims: to extend optical entanglement experiments into higher order spatial modes, where the potential scalability of the entanglement is improved, and to simplify entanglement experiments in order to optimise entanglement when dealing with finite and imperfect resources.

The three experiments described here are:

- the spatial entanglement experiment;
- the multimode entanglement experiment; and
- the asymmetric entanglement experiment.

Spatial entanglement

The spatial entanglement experiment involved the entanglement of the position and momentum of bright laser beams. Two squeezed TEM_{10} beams were produced, and one was combined with a reference TEM_{00} beam. The two resultant beams were then mixed together on a beamsplitter with a $\pi/2$ phase shift. The aim was to observe the EPR entanglement witness, in the spirit of the original *Gedanken* experiment. The EPR value was found to be 0.62 ± 0.03 for one direction of inference, and 0.94 ± 0.03 for the other direction when normalised to a QNL of one. The inseparability for the system was also measured, returning a value of 0.51 ± 0.02 .

The spatial entanglement experiment is an example of applying the original thought experiment to macroscopic objects, in this case to intense laser beams. The demonstration of entanglement performed here makes the concept of entanglement more accessible, due to the use of the highly intuitive observables - position and momentum - and the application of these observables to laser beams, which are ubiquitous both in optics and in society at large. Further, the requirement for good quality higher order spatial mode squeezing in this

experiment led to improved techniques for producing multimode squeezed beams, making entanglement for higher order modes more attainable for this, and other, experiments.

Multimode entanglement

The multimode entanglement experiment aimed to build upon more traditional optical entanglement setups in a way that is novel, uses fewer components and has more scope for scalability. The experiment takes place on a single laser beam, using different higher order spatial modes instead of spatially separated laser beams. The importance of scalability in quantum systems cannot be overstated - the information capacity and, potentially, the computational power for quantum systems increases dramatically with an increase in the number of independent modes available.

There were several practical components in this experiment that were applied in original ways:

- The linear squeezer was aligned carefully so that it was degenerate for TEM_{10} and TEM_{01} modes, and thus one squeezer was used in place of the usual two squeezers.
- The phase shift between the two spatial modes was created using a pair of cylindrical lenses positioned on the beam. This induced a Gouy phase shift that was different for the two spatial modes, and the distance between the lenses was adjusted to that the relative phase shift was $\pi/2$, as required.
- The detector used was a quadrant detector, set up with a local oscillator to allow amplitude or phase measurement for both modes at the same time. Here we also employed the detector as a mixer (much like a beamsplitter would in other experiments) by rotating it by $\pi/4$ with respect to the entangled beam.

The multimode entanglement experiment measured the inseparability between the two entangled modes to be 0.79 ± 0.02 . As well as improving the scalability of the entanglement, the experiment also represents a simplification in entanglement setups, with fewer resources required compared to other optical entanglement experiments.

Asymmetric entanglement

In general, a biased entanglement setup consists of one squeezer and a 50:50 beamsplitter. While all entanglement experiments are susceptible to losses, this setup is particularly so, and if the loss is over 33%, EPR entanglement can no longer be measured. By using a

beamsplitter that is adjusted to suit the loss of the system, EPR entanglement can be witnessed for losses of up to 50%. The ideal beamsplitter ratio was found to be $\frac{1}{2\eta}$, where η is the transmission of the squeezer that is used. The experiment was performed using a polarizing beamsplitter with a half wave plate as a variable beamsplitter, and EPR entanglement was witnessed with a loss that would otherwise make such a measurement impossible. Optics equipment is rarely without loss or imperfection, and the knowledge of how to optimise an experiment so that this loss has as small an effect as possible on the end result will be useful for many quantum optics experiments.

Outlook

Here we have described three experiments that have been performed: the spatial entanglement experiment, with position-momentum entanglement of laser beams; the multimode entanglement experiment, where two spatial modes were entangled on a single beam; and the asymmetric entanglement experiment, where the entanglement of a system is optimised depending on the various losses encountered. While the three experiments described all work towards the two general goals stated at the beginning of this conclusion, they are also connected more directly in their application to the next experiment planned by the quantum imaging group at the ANU.

The group is working on extending the multimode entanglement experiment to more spatial modes, making use of the improved scalability that comes with this setup.

There will be several new components to this planned new experiment. The quadrant detector will be replaced with a detector of higher pixelation, to allow several modes to be measured simultaneously. In order to mix the modes and apply phase shifts between the modes, spatial light modulators are employed in a mode converter. This new experiment should be able to entangle more modes and therefore carry more information, and the type of entanglement witnessed could be extended to measures such as GHZ entanglement.

The optimisation of the beamsplitter ratio to improve the entanglement produced can be adapted to different entanglement setups and measures. Here it is applied to a biased EPR entanglement experiment, but the same method can be employed for the inseparability measure, and for setups with two squeezers and different losses on each input or on the two entangled beams.

Recent years have seen research groups developing quantum resources that can impart tuned delays on to EPR entangled beams [14], that serve as quantum memories [13], and

that are able to entangle various objects across several modes [60]. Our experiments are part of a greater movement within the quantum optics community to make these devices more practical to implement in either quantum communication networks or in many other potential applications.

In the less immediate future, the potential applications of optical entanglement are far-reaching, with schemes proposed for quantum computers, quantum communication systems, and various improvements to precision measurements. Our achievement in simplifying and optimising the production of optical entanglement will aid in the development of these applications.

Entanglement equations

The output fields of the beamsplitter, a_x and a_y , can be written in terms of the input fields, a_1 and a_2 , as follows:

$$\begin{aligned} a_x &= e^{i\phi_x} \left(\sqrt{1-t}a_1 + \sqrt{t}e^{i\beta}a_2 \right) \\ a_y &= e^{i\phi_y} \left(\sqrt{t}a_1 - \sqrt{1-t}e^{i\beta}a_2 \right). \end{aligned} \quad (\text{A.1})$$

Here β is the relative phase between the two input fields, and ϕ_x and ϕ_y are the phases required to make the expectation values α_x and α_y real. We can also obtain the creation operators for the fields:

$$\begin{aligned} a_x^\dagger &= e^{-i\phi_x} \left(\sqrt{1-t}a_1^\dagger + \sqrt{t}e^{-i\beta}a_2^\dagger \right) \\ a_y^\dagger &= e^{-i\phi_y} \left(\sqrt{t}a_1^\dagger - \sqrt{1-t}e^{-i\beta}a_2^\dagger \right). \end{aligned} \quad (\text{A.2})$$

Note that setting $\alpha_x, \alpha_y \in \mathfrak{R}$ is effectively defining the amplitude quadrature such that it corresponds to the intensity of the beam, so the quadrature measured by a simple photodetector is always the amplitude quadrature.

From here, any quadrature can be defined by the relationship:

$$X^\theta = ae^{-i\theta} + a^\dagger e^{i\theta}. \quad (\text{A.3})$$

We have expressions for the two outputs of the entanglement beamsplitter for the case where two input beams of equal power are mixed with a $\pi/2$ phase difference on a 50:50 beamsplitter. These can be found by setting $\phi_x = \pi/4$ and $\phi_y = -\pi/4$ in Equations A.1 and A.2, and then using A.3 with $\theta = 0$ for the amplitude quadrature and $\theta = \pi/2$ for the

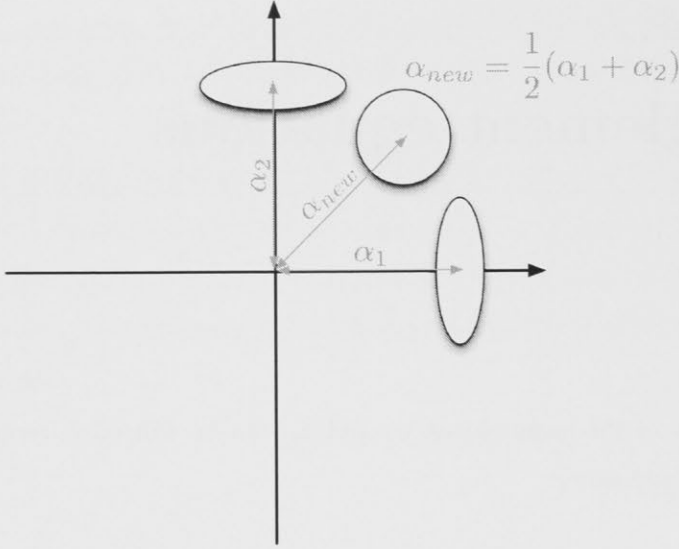


Figure A.1: Two beams mixed with a $\pi/2$ phase shift result in a new coherent amplitude.

phase quadrature. The outputs are given by:

$$\begin{aligned} X_x^\pm &= \frac{1}{2} (\pm X_1^+ + X_2^+ + X_1^- \mp X_2^-) \\ X_y^\pm &= \frac{1}{2} (X_1^+ \pm X_2^+ \mp X_1^- + X_2^-). \end{aligned} \quad (\text{A.4})$$

We can look only at the noise portion of the output beams by taking the quickly changing part of the expressions:

$$\begin{aligned} \delta X_x^\pm &= \frac{1}{2} (\pm \delta X_1^+ + \delta X_2^+ + \delta X_1^- \mp \delta X_2^-) \\ \delta X_y^\pm &= \frac{1}{2} (\delta X_1^+ \pm \delta X_2^+ \mp \delta X_1^- + \delta X_2^-). \end{aligned} \quad (\text{A.5})$$

In order to find the EPR value that can be obtained, we must first calculate the conditional variance for both quadratures. The conditional variance is given by:

$$\begin{aligned} V_{x|y} &= \min_g \langle (\delta X_x - g \delta X_y)^2 \rangle \\ &= V_x - \frac{|\langle \delta X_x \delta X_y \rangle|^2}{V_y}. \end{aligned} \quad (\text{A.6})$$

We can find the expressions for V_x and V_y by calculating $\langle (\delta X_{x,y})^2 \rangle$ using the substitutions $\langle (\delta X_{1,2})^2 \rangle \rightarrow V_{1,2}$, $\langle (\delta X_{1,2}^+ \delta X_{1,2}^-) \rangle \rightarrow i$, and $\langle (\delta X_{1,2}^- \delta X_{1,2}^+) \rangle \rightarrow -i$, and we then arrive

at:

$$V_x^\pm = V_y^\pm = \frac{1}{4} (V_1^+ + V_2^+ + V_1^- + V_2^-). \quad (\text{A.7})$$

Similarly, we can find:

$$\langle \delta X_x^\pm \delta X_y^\pm \rangle = \frac{1}{4} (\pm V_1^+ \pm V_2^+ \mp V_1^- \mp V_2^-). \quad (\text{A.8})$$

Then by calculating the conditional variance for both quadratures, we can arrive at the EPR value that will be observed. If we assume that the two squeezers are identical, such that $V_2^- = V_1^-$ and $V_2^+ = V_1^+$, then we arrive at the expression for EPR:

$$\begin{aligned} \epsilon &= V_{x|y}^+ V_{x|y}^- \\ &= 4 \left(\frac{V_1^- V_1^+}{V_1^- + V_1^+} \right)^2. \end{aligned} \quad (\text{A.9})$$

Alternatively, this can be written in terms of the original amount of squeezing V_0 and the total loss in the system η , if there is no excess classical noise being coupled into the system¹. This is found by substituting $V_1^+ \rightarrow \eta V_0^+ + (1 - \eta)$ and $V_1^- \rightarrow \eta/V_0^+ + (1 - \eta)$, and then simplifying. V_0 is the original amount of squeezing, inside the OPA. This yields:

$$\epsilon = 4 \left(1 + \eta + \frac{2\eta - 1}{\eta(V_0^+ + 1/V_0^+ - 2) + 2} \right)^2. \quad (\text{A.10})$$

¹The loss is assumed to be symmetric, so that before the beamsplitter $\eta_1 = \eta_2$, and, after the beamsplitter, $\eta_x = \eta_y$. The total loss is then the product of these two: $\eta = \eta_{x,y}\eta_{1,2}$

Biased entanglement theory

We start from the expression for the EPR entanglement for biased entanglement on a $t : (1 - t)$ beamsplitter.

$$\epsilon = \frac{V_1^+ V_1^-}{(1 + t(V_1^- - 1))(1 + t(V_1^+ - 1))} \quad (\text{B.1})$$

Instead of characterising the OPA using the squeezing and antisqueezing, V_1^+ and V_1^- , we can instead use the original amount of squeezing, V_0 , and the transmission of the beam, η_1 , by making the substitutions:

$$\begin{aligned} V_1^+ &\rightarrow \eta_1 V_0 + 1 - \eta_1 \\ V_1^- &\rightarrow \frac{\eta_1}{V_0} + 1 - \eta_1. \end{aligned}$$

This then gives us the less elegant expression:

$$\epsilon = \frac{(V_0(\eta_1 - 1) - \eta_1)(1 + (V_0 - 1)\eta_1)}{(1 + (V_0 - 1)t\eta_1)(V_0(t\eta_1 - 1) - t\eta_1)}. \quad (\text{B.2})$$

Differentiating ϵ with respect to t then gives:

$$\frac{\partial \epsilon}{\partial t} = \frac{(1 - V_0)^2 (V_0(\eta_1 - 1) + \eta_1)\eta_1(1 + (V_0 - 1)\eta_1) \overbrace{(2t\eta_1 - 1)}^*}{(1 + (V_0 - 1)t\eta_1)^2 (V_0 + t\eta_1 - V_0 t\eta_1)^2}. \quad (\text{B.3})$$

The EPR value is at a minimum when we have $\frac{\partial \epsilon}{\partial t} = 0$. Looking at the ‘*’ marked on the above equation, we can see that this then gives us the optimal beamsplitter ratio of:

$$t_{opt} = \frac{1}{2\eta_1}. \quad (\text{B.4})$$

The technique of altering the beamsplitter ratio can be useful for other experimental criterion as well. For a biased entanglement setup, the optimal beamsplitter ratio does

not depend on the loss in the squeezer, but does change for an asymmetric loss after the beamsplitter. This is shown in Figure B.1.

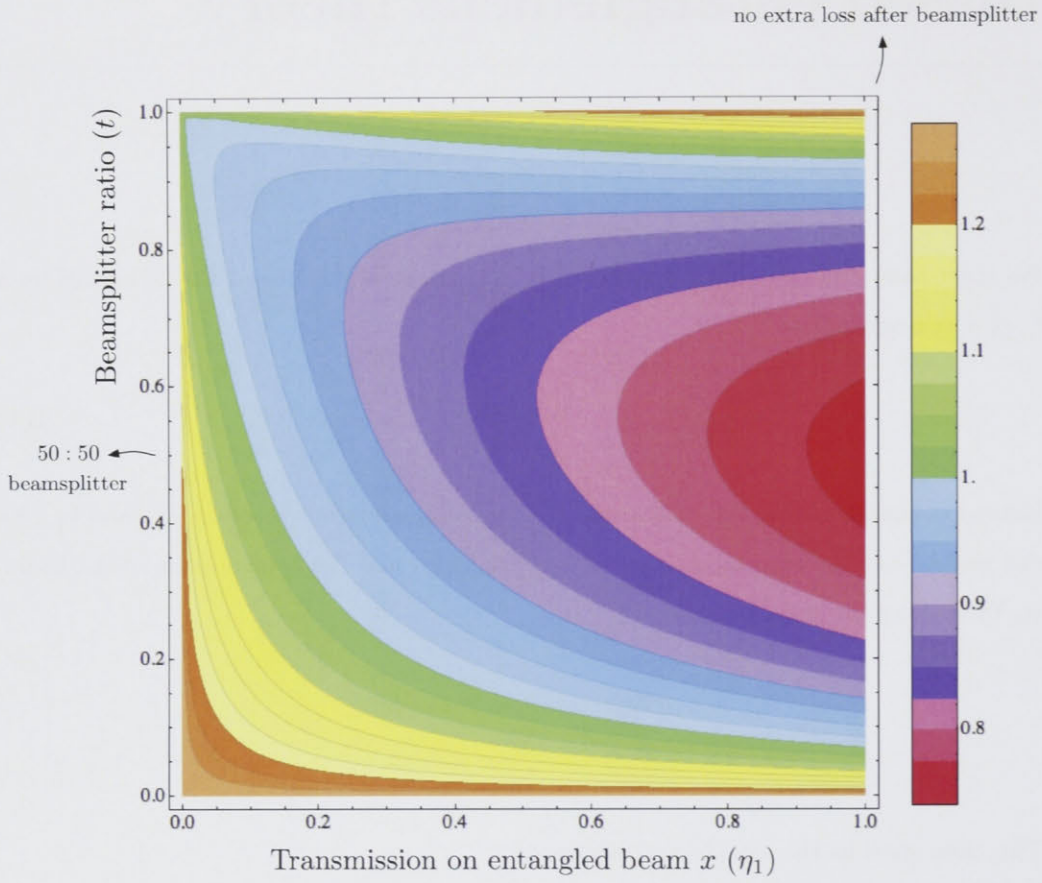


Figure B.1: Results for the Inseparability in a biased entanglement experiment.

Bibliography

- [1] A. Einstein, B. Podolsky, and N. Rosen. Can quantum-mechanical description of physical reality be considered complete? *Phys. Rev.*, 47:777, 1935.
- [2] J F Clauser and A Shimony. Bell's theorem. experimental tests and implications. *Reports on Progress in Physics*, 41(12):1881, 1978.
- [3] A. Aspect, P. Grangier, and G. Roger. Experimental Realization of Einstein-Podolsky-Rosen-Bohm Gedankenexperiment: A New Violation of Bell's Inequalities. *Phys. Rev. Lett.*, 49(2):91–94, 1982.
- [4] M. D. Reid. Demonstration of the Einstein-Podolsky-Rosen paradox using nondegenerate parametric amplification. *Phys. Rev. A*, 40(2):913–923, 1989.
- [5] Ch. Silberhorn, P. K. Lam, O. Weiss, F. Koenig, N. Korolkova, and G. Leuchs. Generation of continuous variable Einstein-Podolsky-Rosen entanglement via the Kerr nonlinearity in an optical fiber. *Phys. Rev. Lett.*, 86:4267, 2001.
- [6] O. Glöckl, U. L. Andersen, and G. Leuchs. Verifying continuous-variable entanglement of intense light pulses. *Phys. Rev. A*, 73:012306, 2006.
- [7] B. Hage, A. Sambrowski, and R. Schnabel. Towards Einstein-Podolsky-Rosen quantum channel multiplexing. *Physical Review A*, 81(6):062301, 2010.
- [8] W. P. Bowen, N. Treps, R. Schnabel, and P. K. Lam. Experimental demonstration of continuous variable polarization entanglement. *Phys. Rev. Lett.*, 89:253601, 2002.
- [9] N. Korolkova, G. Leuchs, R. Loudon, T. C. Ralph, and C. Silberhorn. Polarization squeezing and continuous-variable polarization entanglement. *Phys. Rev. A*, 65:052306, 2002.
- [10] R. Dong, J. Heersink, J. Yoshikawa, O. Glöckl, U. Andersen, and G. Leuchs. An efficient source of continuous variable polarization entanglement. *New Journal of Physics*, 9:410, 2007.

- [11] T. Aoki, G. Takahashi, T. Kajiya, J.-I. Yoshikawa, S. L. Braunstein, P. van Loock, and A. Furusawa. Quantum error correction beyond qubits. *Nat. Phys.*, 5(8):541–546, 2009.
- [12] M. Yukawa, R. Ukai, P. van Loock, and A. Furusawa. Experimental generation of four-mode continuous-variable cluster states. *Physical Review A*, 78(1):012301, 2008.
- [13] M. Hosseini, B. M. Sparkes, G. Hétet, J. J. Longdell, P. K. Lam, and B. C. Buchler. Coherent optical pulse sequencer for quantum applications. *Nature*, 461:241–245, 2009.
- [14] A. M. Marino, R. C. Pooser, V. Boyer, and P. D. Lett. Tunable delay of einstein–podolsky–rosen entanglement. *Nature*, 457:859–862, 2009.
- [15] W. Heisenberg. Über den anschaulichen Inhalt der quantentheoretischen Kinematik und Mechanik. *Zeitschrift für Physik*, 43:172, 1927.
- [16] D. F. Walls and G. J. Milburn. *Quantum optics*. Springer-Verlag, 1995.
- [17] B. Yurke. Use of cavities in squeezed state generation. *Phys. Rev. A*, 20:408, 1984.
- [18] R. W. Boyd. Intuitive explanation of the phase anomaly of focused light beams. *J. Opt. Soc. Am.*, 70(7):877–880, 1980.
- [19] C. W. Gardiner and M. J. Collett. Input and output in damped quantum systems: Quantum stochastic differential equations and the master equation. *Phys. Rev. A*, 31:3761, 1985.
- [20] H. A. Bachor and T. C. Ralph. *A Guide to Experiments in Quantum Optics*. Wiley, 2nd edition, 2004.
- [21] B. E. A. Saleh and M. C. Teich. *Fundamentals of Photonics*. Wiley, 1991.
- [22] R.W.P. Drever, J.L. Hall, F.V. Kowalski, J. Hough, G.M. Ford, A.J. Munley, and H. Ward. Laser phase and frequency stabilization using an optical resonator. *Appl. Phys. B*, 31:97, 1983.
- [23] V. Delaubert, D. A. Shaddock, P. K. Lam, B. C. Buchler, H-A. Bachor, and D. E. McClelland. Generation of a phase-flipped Gaussian mode for optical measurements. *J. Opt. A*, 4:393, 2002.

-
- [24] B. C. Buchler. Electro-optic control of quantum measurements. *PhD thesis*, 2001.
- [25] D. A. Kleinman. Theory of optical parametric noise. *Phys. Rev.*, 174(3):1027–1041, 1968.
- [26] L. M. Duan, G. Giedke, J. I. Cirac, and P. Zoller. Inseparability criterion for continuous variable systems. *Phys. Rev. Lett.*, 84:2722, 2000.
- [27] A. L. Schawlow and C. H. Townes. Infrared and optical masers. *Phys. Rev.*, 112(6):1940–1949, 1958.
- [28] V. Delaubert, N. Treps, M. Lassen, C. C. Harb, C. Fabre, P. K. Lam, and H-A. Bachor. TEM₁₀ homodyne detection as an optimal small-displacement and tilt-measurement scheme. *Phys. Rev. A*, 74(5):053823, 2006.
- [29] M. T. L. Hsu, W. P. Bowen, N. Treps, and P. K. Lam. Continuous-variable spatial entanglement for bright optical beams. *Phys. Rev. A*, 72:013802, 2005.
- [30] N. Treps, U. Andersen, B. Buchler, P. K. Lam, A. Maître, H.-A. Bachor, and C. Fabre. Surpassing the standard quantum limit for optical imaging using nonclassical multi-mode light. *Phys. Rev. Lett.*, 88:203601, 2002.
- [31] N. Treps, N. Grosse, W. P. Bowen, C. Fabre, H. A. Bachor, and P. K. Lam. A quantum laser pointer. *Science*, 301:940, 2003.
- [32] V. Delaubert, N. Treps, C. C. Harb, and H-A. Bachor. Quantum measurements of spatial conjugate variables: displacement and tilt of a Gaussian beam. *Opt. Lett.*, 31(10):1537–1539, 2006.
- [33] V. Boyer, A. M. Marino, and P. D. Lett. Generation of spatially broadband twin beams for quantum imaging. *Phys. Rev. Lett.*, 100:143601, 2008.
- [34] V. Delaubert. Quantum imaging with a small number of transverse modes. *PhD thesis*, 2007.
- [35] J. Janousek. Investigation of non-classical light and its application in ultrasensitive measurements. *PhD thesis*, 2007.
- [36] Z.Y. Ou, S.F. Pereira, H.J. Kimble, and K.C. Peng. Realization of the Einstein-Podolsky-Rosen paradox for continuous variables. *Phys. Rev. Lett.*, 68:3663, 1992.

-
- [37] D.A. Shaddock, M.B. Gray, and D.E. McClelland. Frequency locking a laser to an optical cavity by use of spatial mode interference. *Optics Letters*, 24(21):1499–1501, 1999.
- [38] B.J.J. Slagmolen, D.A. Shaddock, M.B. Gray, and D.E. McClelland. Frequency stability of spatial mode interference (tilt) locking. *IEEE Journal of Quantum Electronics*, 38(11):1521–1528, 2002.
- [39] N.P. Robins, B.J.J. Slagmolen, D.A. Shaddock, J.D. Close, and M.B. Gray. Interferometric, modulation-free laser stabilization. *Optics Letters*, 27(21):1905–1907, 2002.
- [40] V. Boyer, A. M. Marino, R. C. Pooser, and P. D. Lett. Entangled images from four-wave mixing. *Science*, 321:544–547, 2008.
- [41] A. S. Villar, M. Martinelli, C. Fabre, and P. Nussenzveig. Direct production of tripartite pump-signal-idler entanglement in the above-threshold optical parametric oscillator. *Phys. Rev. Lett.*, 97(14):140504, 2006.
- [42] A. S. Bradley, M. K. Olsen, O. Pfister, and R. C. Pooser. Bright tripartite entanglement in triply concurrent parametric oscillation. *Phys. Rev. A*, 72(5):053805, 2005.
- [43] Takao Aoki, Nobuyuki Takei, Hidehiro Yonezawa, Kentaro Wakui, Takuji Hiraoka, Akira Furusawa, and Peter van Loock. Experimental creation of a fully inseparable tripartite continuous-variable state. *Phys. Rev. Lett.*, 91(8):080404, 2003.
- [44] X. Su, A. Tan, X. Jia, J. Zhang, C. Xie, and K. Peng. Experimental preparation of quadripartite cluster and Greenberger-Horne-Zeilinger entangled states for continuous variables. *Physical Review Letters*, 98(7):070502, 2007.
- [45] N. C. Menicucci, S. T. Flammia, H. Zaidi, and O. Pfister. Ultracompact generation of continuous-variable cluster states. *Physical Review A*, 76(1):010302, 2007.
- [46] E. H. Huntington, G. N. Milford, C. Robilliard, and T. C. Ralph. Coherent analysis of quantum optical sideband modes. *Opt. Lett.*, 30(18):2481–2483, 2005.
- [47] G. J. de Valcárcel, G. Patera, N. Treps, and C. Fabre. Multimode squeezing of frequency combs. *Phys. Rev. A*, 74(6):061801, 2006.
- [48] M. Lassen, V. Delaubert, J. Janousek, K. Wagner, H. A. Bachor, P. K. Lam, N. Treps, P. Buchhave, C. Fabre, and C. C. Harb. Tools for multimode quantum information:

-
- Modulation, detection, and spatial quantum correlations. *Physical Review Letters*, 98(8):083602, 2007.
- [49] M. Beck. Quantum state tomography with array detectors. *Physical Review Letters*, 84(25):5748, 2000.
- [50] L. A. Lugiato and A. Gatti. Spatial structure of a squeezed vacuum. *Physical Review Letters*, 70(25):3868—3871, 1993.
- [51] S.-K. Choi, M. Vasilyev, and Prem Kumar. Noiseless optical amplification of images. *Phys. Rev. Lett.*, 83(10):1938–1941, 1999.
- [52] L. Lopez, N. Treps, B. Chalopin, C. Fabre, and A. Matre. Quantum processing of images by continuous wave optical parametric amplification. *Phys. Rev. Lett.*, 100:013604, 2008.
- [53] J. Janousek, K. Wagner, J.-F. Morizur, N. Treps, P. K. Lam, C. C. Harb, and H.-A. Bachor. Optical entanglement of co-propagating modes. *Nature Photonics*, 3(7):399–402, 2009.
- [54] J. Courtial and M. J. Padgett. Performance of a cylindrical lens mode converter for producing Laguerre-Gaussian laser modes. *Optics Communications*, 159(1-3):13–18, 1999.
- [55] M. Lassen, G. Leuchs, and U. L. Andersen. Continuous variable entanglement and squeezing of orbital angular momentum states. *Phys. Rev. Lett.*, 102:163602, 2009.
- [56] I. Csiszar and J. Korner. Broadcast channels with confidential messages. *IEEE Transactions on Information Theory*, 24(3):339 – 348, 1978.
- [57] F. Grosshans, G. Van Assche, J. Wenger, R. Brouri, J. Nicolas, and P. Grangier. Quantum key distribution using Gaussian-modulated coherent states. *Nature*, 421:238–241, 2003.
- [58] Samuel L. Braunstein and Peter van Loock. Quantum information with continuous variables. *Rev. Mod. Phys.*, 77(2):513–577, Jun 2005.
- [59] W. P. Bowen, P. K. Lam, and T. C. Ralph. Biased epr entanglement and its application to teleportation. *Journal of Modern Optics*, 50(5):801–813, 2003.

- [60] D. V. Kupriyanov, O. S. Mishina, I. M. Sokolov, B. Julsgaard, and E. S. Polzik. Multimode entanglement of light and atomic ensembles via off-resonant coherent forward scattering. *Phys. Rev. A*, 71(3):032348, 2005.